The Pennsylvania State University

The Graduate School

Department of Chemistry

# CATALYTIC NANOMOTORS AND MICROPUMP SYSTEMS UTILIZING ALTERNATE FUELS

A Dissertation in

Chemistry

by

Flory K. Wong



Submitted in Partial Fulfillment

of the Requirements

for the Degree of

Doctor of Philosophy

December 2016

The dissertation of Flory K. Wong was reviewed and approved* by the following:

Ayusman Sen
Distinguished Professor of Chemistry
Dissertation Advisor
Chair of Committee

Thomas E. Mallouk
Evan Pugh University Professor of Chemistry, Biochemistry, Molecular Biology, and Physics
Head of the Department of Chemistry

Raymond E. Schaak
DuPont Professor of Materials Chemistry

Darrell Velegol
Distinguished Professor of Chemical Engineering

*Signatures are on file in the Graduate School.

# ABSTRACT

Colloidal assemblies of self-powered active particles have become a focus area of research. Ranging from microscopic particle suspensions to nanoscale molecules, these systems transduce chemical energy into mechanical motion across multiple length scales following a variety of mechanisms. Understanding the energy transduction processes and the subsequent nature of particle dynamics offers unprecedented opportunities to explore the physics of small-scale colloidal systems and to harness their behavior in many useful applications.

However, over a decade after the initial discovery of autonomous bimetallic nanorods, we continue to struggle to bring such systems into real-world applications. Part of the setback has been the in-depth research into hydrogen peroxide fuel. While the studies have built up the fundamental knowledge necessary for the advancement of the field, we have yet to do the same for other systems that employ alternate fuels. This dissertation aims to fill that void by developing nano- and micromotor and pump systems that does not rely on traditional hydrogen peroxide fuel, uses novel material by taking inspiration in other areas of research, and complete in-depth studies to provide a clear understanding of such systems.

Chapter 1 provides a general overview of the research into chemically powered nano- and micromotors and pumps, the motivation behind my interest, and concise descriptions of the individual research projects discussed in this dissertation.

Chapter 2 and 3 discusses a highly efficient silver-based nanomotor and micropump system that operates in iodine media. It is a significant step in the development of a new type of system as it is extremely efficient in fuel conversion as well as being a light-modulated system.

Chapter 4 utilizes an established biopolymer to fabricate an acid-sensitive micropump and a proof-of-concept micromotor. This work provides the fundamentals that can be applied to converting other types of polymer into active colloidal systems.

Chapter 5 puts forth a novel biodegradable dual-mechanism micropump made of zinc and iron. The pump is controlled by both electrokinetics and density driven flows. This new system is undaunted by high electrolyte environments and is not limited to one type of chemical fuel, as it is capable of fluid pumping in acid, salt, and buffered solutions.

This dissertation concludes with a brief perspective on the future advancement in nano- and micromachine development.

# Table of Contents

## LIST OF FIGURES

# LIST OF TABLES

## ACKNOWLEDGEMENTS

First and foremost, I would like to thank my advisor and sanity-checker, Ayusman Sen, who has always given me the freedom to pursue my own research interests and supported me with countless advice, and some prodding along the way. Next I would like to sincerely thank my committee members who always asked great questions and returned with great advice: Tom Mallouk, Ray Schaak, and Darrell Velegol, whose scientific curiosity is contagious and provided both valuable advice and support for a fledgling scientist.

I am thankful to all my collaborators and coworkers, Dr. Chandrani Chattergee, Dr. Saibal Bandyopadhyay, Dr. Abhishek Kar, and Dr. Wentao Duan. I would also like to thank the Sen Group members, old and new: A special thanks for Dr. Ran Liu for his quirky quote and for him passing on his expertise onto me, Dr. Frances Pong and Dr. Chandrani Chattergee for the midnight chats and company ("Long live the night owls!"), Dr. Krishna Kanti Dey for his unending support and charming smile, Isamar Ortiz Rivera for her pinkness and enhanced diffusion demonstrations, Lyanne Valdez for her brilliant expressions, Xi Zhao for her excessive cuteness, Scott Biltek for his lively description of everything, and Matt Collins, Alicia Altemose, Ben Tansi, and Remmi Baker for being fun to chat with when I needed a distraction.

In addition, I would to say I owe a gratitude to all the great staff at the MSC Nanofab and Characterization labs, old and new: Bill Drawl, Mike LaBella, Shane Miller, Bangzhi Liu, Xiaojun Weng, Trevor Clark, Ke Wang Jennifer Grey, Julie Anderson, and Jaime Reish. It has been my pleasure to have worked with you all and learn about the instruments from such nice people.

I would never have survived graduate school if not for the continued support and encouragement from my family and close friends: Granny, who always believed I could fly if I wanted to (may she be smiling down on me from wherever she is right now); Dr. Andrew Byro and Richard Jarvis, who treasures me like the kid sister they never had; Joanna Auyeung for her views and advice on life; James Wu, for his midnight chats and encouragement; and Roger Ly, Jenny Yu, Eikar Lai, Thomas Wong, Jack Chiu, Wan Yin Liu, Jie Lin, Helen Zheng, Lily Wong, I thank you all for not giving up on me when I was unable to share many moments with you in the last 5 years.

And, last but not least, my Mom, Dad, and Jing, for all their endless love, enduring patience, and complete support.

As a side note, I would also like to acknowledge the role others had in my professional career. I would like to thank Dr. Bunsen Honeydew and Mr. Beaker for preparing me for graduate school and to motivate me through Mr. Beaker's thoughtful dialogue. I would also like to thank the Minions for helping me uphold laboratory safety and Trees for their sacrifice to make this dissertation possible.

# EPIGRAPH

"Today's science fiction is tomorrow's science fact."

– Isaac Asimov

# Chapter 1 Introduction

## 1.1 Background

"Anything you dream is fiction, and anything you accomplish is science, the whole history of mankind is nothing but science fiction"

– Raymond Douglas Bradbury, author of Fahrenheit 451.

We cannot deny that advancements in science, technology, and the world in general often start off as dreams and desires. Medicine stemmed from the desire for immortality, and chemistry from the dream of turning base metals into gold. Many technological advances stem from an aspiration to improve our environmental conditions and quality of life. Such desires drive discoveries.

For thousands of years, civilization has largely been a matter of mastery of motion. From the wheel which allowed heavy loads to be moved with ease, to pulleys which brought those weights to great heights. Later civilizations would develop gears and springs, for the first time harnessing the power of controlled release of stored motion in the form of clockworks. Today, automobiles can transport goods and people hundreds of miles on chemical fuel. Gears have been developed to create complex machineries capable of a multitude of tasks. Manufacturing prowess can be said to be at the height of productivity through coordinated motion inspired by the disassembly plants in the stockyards of Chicago and the assembly plants of Detroit a hundred years ago. While motion on the macroscale has been well understood and harnessed for applications, motion on the micro- and nanoscale was largely unexploitable due to the limitations of technology.

Feymann's famous speech "There's plenty of room at the bottom" in 1959 directly addressed how there is a vast field of research that is prime for progress. He issued challenges for the scientific community in an effort to spur interest. Unfortunately, his speech garnered little attention to the field. It wasn't until 1986, when Eric Drexler published his famous book, *Engines of Creation* that interest in the creation of small-scale machines began to take root. The possibilities for a range of applications using nano-assemblies and nano-machines enticed many researchers to begin looking into bringing those concepts into reality. Beginning with this sentiment, over the next two decades, a multitude of micro- and nano- systems have been fabricated, *e.g.* patchy particles,[1-5] molecular assemblies,[6-10] quantum dots,[11-15] and nanoparticle synthesis and fabrication.[16-20] Nanotechnology promised to revolutionize the world, and methodically began to fulfill those promises in recent years.

Ever since, the micro- and nano- world have been extensively researched. While we have become proficient at *making* such systems, we were unable to produce and control active colloids. The scientific community initially turned to protein engineering; naturally occurring biomolecular proteins served as promising models for creating artificial nanomachines. They do not require fabrication or modification as motor proteins are naturally adept at motion. Proteins such as kinesin, dynein, and myosin hydrolyze adenosine triphosphate (ATP) and convert the chemical energy into useful mechanical motion.[21-25] Researchers were able to harness the motion of these proteins by directly linking them to synthetic systems for directed motion.[26-30] Hess, et al. were able to use these proteins as molecular shuttles for active transport in synthetic environments.[26] Over the course of the last decade, a multitude of biological systems have been developed. However, these systems were limited to physiological conditions, and efforts in mimicking their

structural features in all-synthetic systems proved extremely difficult due to their inherent complexity.

In 2002, the first evidence of chemical energy being able to power the motion of fully-synthetic structures was demonstrated. Whitesides and his coworkers observed the autonomous motion of millimeter scale platinum-polymer plates in hydrogen peroxide ($H_2O_2$).[31] The plates operated via bubble formation resulting from the decomposition of $H_2O_2$. Two years later in 2004, the first true catalytic autonomous nanomotors were developed by Sen and Mallouk,[32] followed by Ozin and coworkers.[33] They had developed bimetallic nanorods that underwent an electrokinetic mechanism to fuel its motion.[32] These discoveries initiated the research into the development of nanomotors in order to understand motion on the micro- and nanoscale.

Since these initial discoveries, the field of artificial motors capable of directed motion has grown by leaps and bounds in a myriad assortment of varieties.[34-40] These systems can be separated into three general categories typified by their mechanism of motion: directed translation motion motors, rotational motion rotors, and stationary pumps that drive motion in its immediate surrounding, as illustrated in Figure 1-1. The motion of these nano- and micromachines that operate in low Reynolds number fluids are constrained by the Scallop theorem, where motion becomes possible only when particles employ strategies to bring the time-reversal invariance. [41-43] That is, where the reverse of said motion does not simply undo what the motion achieved and end up effectively dead in the water. Motors that move in this environment are dominated by surface forces and interfacial effects with negligible effects from inertia.[44-47] Motion of such systems further require a break in symmetry, either through composition, reaction, and/or shape. Sustained motion requires a constant supply of energy.

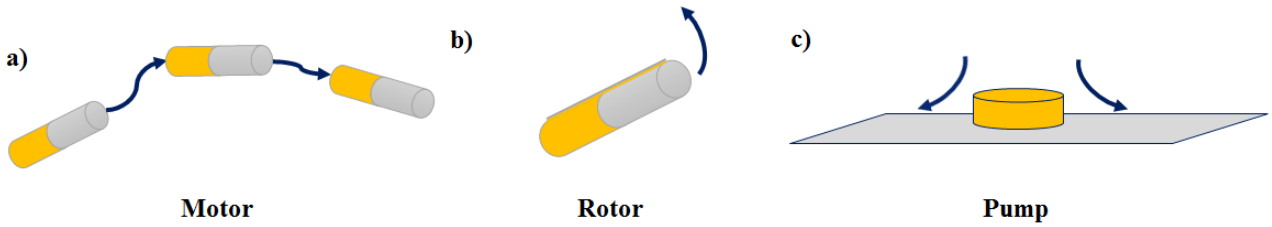


**Figure 1-1.** General scheme for artificial systems that exhibit (a) translation motion, (b) circular motion, and (c) fluid flow arounds stationary pump.

### 1.2 Development of catalytic motor and pump systems

Since the discovery of bimetallic metal nanorods that moved autonomously in $H_2O_2$, these systems have been studied extensively. These bimetallic nanorods usually undergo a self-electrophoretic mechanism.[31-33,48-52] Asymmetric chemical reactions that occur at the two ends of the nanorod generates a gradient of the species (*e.g.* protons, anions) that results in an electric field.[48] The produced field induces motion of the motors themselves due to electrophoresis[48] and exhibits chemotaxis towards fuel similar to living systems[53], illustrated by the Au-Pt nanomotor system in Figure 1-2. A wide variety of electrophoretic motors that utilize hydrogen peroxide as chemical fuel have been fabricated, with applications such as water purification and cargo delivery.

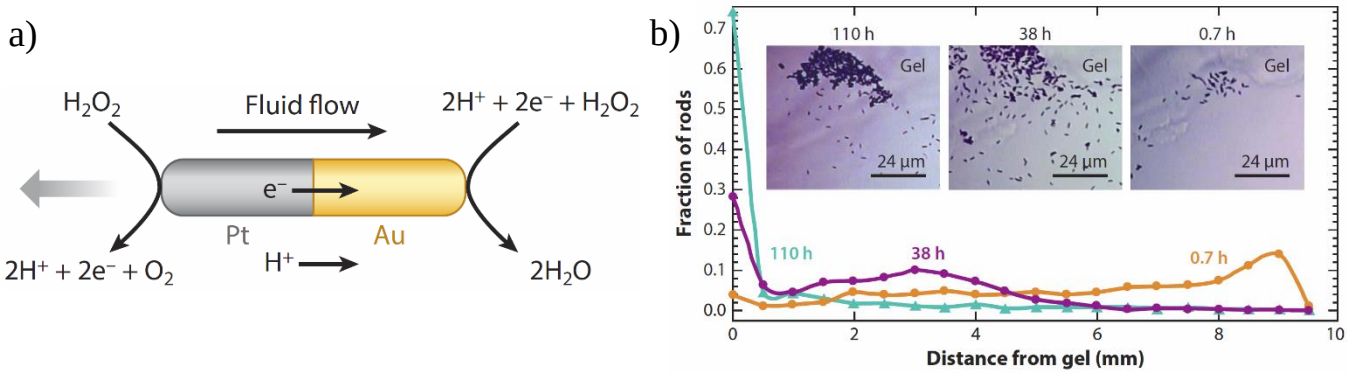


**Figure 1-2.** (a) Self-electrophoretic bimetallic motor using hydrogen peroxide as fuel.[48] (b) Chemotactic movement of Au-Pt nanorods up peroxide fuel gradients.[53]

Other motor systems that operate in hydrogen peroxide have also been fabricated. Decomposition of hydrogen peroxide can lead to bubble formation, leading to the development of what are commonly known as bubble-propelled motor systems. Bubble-propelled motors have been made using a variety of materials and architectures, *e.g*. tubular motors,[54-59] nanorods,[60-67] Janus platinum particles,[68-70] and catalase-containing biomaterial.[71-72]

### 1.3 Motor and pump systems utilizing alternate fuels

While the initial impetus of the field was with peroxide based systems, motors and pumps in other media have been of increased importance in recent years. These new systems utilize materials that enables the use of other chemical fuels, often exploiting the intrinsic characteristics of the material employed.

Chemical-responsive and light-sensitive material have been used to create schooling systems or trigger schooling behavior in conjunction with chemical fuel.[73-77] These systems often operate under diffusiophoresis, where the colloidal particles produce a non-uniform gradient of solute. Such systems have been show to move charged particles in and out of dead-end pores and to heal cracks.[78,79] Bubble-propelled motors that utilize other materials and fuels, such as water or biocompatible fluids, have been show to accomplish tasks such as drug delivery and water remediation.[80-85]

Polymers can also be used to fabricate motors and pumps. Polymer systems can be broken down into two general types: polymerization and depolymerization. For polymerization systems, the conversion of monomers into polymer material through anchoring of catalyst materials can power motors through enhanced diffusion and can display chemotaxis in a monomer concentration gradient.[86-88] The catalyst material themselves can also become motors through the turnover of

reagents to products, leading to enhanced motion of the catalyst when not immobilized to a substrate.[89] These systems can provide a basic design for creating new motors and pumps powered by well-characterized organometallic catalysts and have aided the scientific community to understand motion on the angstrom scale.

Depolymerization motors and pumps operate via the degradation of the polymer from chemical stimuli and triggering the release of decomposition products (monomer and by-products).[90-93] This can act to lower surface tension surrounding a motor, allowing it to move towards areas of higher surface tension. When immobilized onto a surface, thermal fluctuations or density differences can cause fluid flows surrounding the polymer. This type of system allows for use of any well-understood polymers that will respond and depolymerize/degrade in the presence of chemical stimulus.

Hybrid biosystems have also been used to produce biocompatible motors and pumps. Biomaterials such as spermatozoa,[54] DNA-functionalization,[88,94-95] enzyme-functionalization,[96,97] and active free enzyme[98-101] have all be used to make nano- and micromotor systems. Further, immobilization of active enzymes can generate enough mechanical force to cause directional fluid pumping.[102-105] These biosystems exhibit chemotactic behavior, which has been used to direct the motion. Such systems have been used for analyte detection and drug release, sensor system, and separations of enzyme species based solely on activity. [102-106]

### 1.4 Research motivation

From a scientific standpoint, investigating systems involving molecules and small particles is inherently challenging due to the stochastic nature of particle dynamics, the limitations of experimental and modeling techniques in characterizing non-equilibrium systems, and need for

multidisciplinary expertise. The ultimate goal of research in this area is to create a new models for the design of active functional materials and systems by (a) leveraging precise chemical control associated with molecular-level manipulation of materials to create functional building blocks; (b) mobility resulting from biomimetic catalytic energy harvesting from the local environment; (c) rapid and reversible assembly capabilities provided by emergent self-assembly; (d) intelligence and communication capabilities that have been demonstrated in groups of interacting microorganisms; (e) ability to perform specific tasks in response to signals from each other and the environment.

With this in mind, the research conducted in this dissertation into the field of nanomotors and micropumps was an effort to discover new original systems that does not utilize traditional peroxide fuels. Many studies conducted in the field has been deeply rooted in using hydrogen peroxide. Peroxide powered motors and pumps are therefore the most well-understood systems due to the vast literature ranging from fabrication, mechanism, theory and applications on such systems. Peroxide motors and pumps, however, can have limitations in real-world applications. For example, bubble-propelled motors are some of the fastest prototypes developed but the bubble formation itself becomes an impediment for *in-vivo* applications. Electrophoretic motors utilizing peroxide operates as long as fuel is present, but oxygen formation will become a hindrance in any closed system, such as a microfluidic channel. While peroxide-based systems have been invaluable for developing prototype motor function and mechanisms, it is imperative to begin to move away from this system as it imposes a limitation on the advancement of the field.

In the previous section, it can be seen that many novel nanomotor and pump systems that have been developed using alternate fuels. These studies, however, have not been studied as in-depth in comparison to peroxide-based systems. Many of these alternate fuel systems also only

contain one dimension of control, mainly one type of fuel and the material that responds to the fuel that generates motion. In order to truly develop alternate fuel motor and pump systems, such systems should be well-understood and engineered such that multiple conditions or functions can be appended to the system for better control. As such, the research in this dissertation aims to not only develop original systems but also to add dimensions to the motors and pumps.

In Chapter 2, a novel silver-based nanomotor system that uses iodine fuel is described. The system is the most efficient self-electrophoretic motor reported to date and, in addition to its high fuel efficiency, has a light-harvesting aspect that can be used to further tailor motor speeds. Further, the system has displayed collective behavior using the same motor components and fuel.

In Chapter 3, the silver-based nanomotor described in Chapter 2 was adapted into a micropump system that triggers fluid pumping upon iodine exposure. It further exhibited light-modulating effects that manifest in different behaviors of positively charged and negatively charged tracer particles. This provides insight into light-modulated electroosmotic flows resulting from the redox reaction on the surface of the silver-platinum interface.

In Chapter 4, a biocompatible acetalated dextran polymer system that shows great promise as a therapeutic agent was adapted into a micropump and model micromotor system. Fluid flow speeds were explored in both a simple acidic media and buffered pH solution to determine the effect of ions and buffering on the pump speeds. In addition, pump speeds were further explored by varying the amount of acetal coverage along the polymer length to determine its effect, which gives another dimension to pump speed modulation and control.

In Chapter 5, a novel biodegradable bimetallic zinc-iron micropump was developed that allows for the use of a wide range of chemical fuels, ranging from acidic to basic to neutral solutions. High ionic content does not impede fluid flow on the micropump, which is rarely

observed in electrokinetic systems. This system provides an excellent new class of material for biological applications that does not contain issues present in many electrokinetic systems.

## 1.5 References


1. Pawar, A. B.; Kretzschmar, I. Fabrication, assembly, and application of patchy particles. *Macromol. Rapid Commun.* **2010**, *2*, 150-168.
2. Duguet, E.; Hubert, C.; Chomette, C.; Perro, A.; Ravaine, S. Patchy colloidal particles for programmed self-assembly. *Comptes Rendus Chimie* **2016**, *19*, 173-182.
3. Walther, A.; Muller, A. H. E. Janus Particles: Synthesis, self-assembly, physical properties, and applications. *Chem. Rev.* **2013**, *113*, 5194-5261.
4. Du, J.; O'Reilly, R. K. Anisotropic particles with patchy, multicomponent and Janus architectures: preparation and application. *Chem. Soc. Rev.* **2011**, *40*, 2402-2416.
5. Yi, G-R.; Pine, D. J.; Sacanna, S. Recent progress on patchy colloids and their self-assembly. *J. Phys.: Condens. Matter* **2013**, *25*, 193101.
6. Zhang, S. Fabrication of novel biomaterials through molecular self-assembly. *Nature Biotech.* **2003**, *21*, 1171-1178.
7. Barth, J. V.; Constantini, G.; Kern, K. Engineering atomic and molecular nanostructures at surfaces. *Nature* **2005**, *437*, 671-679.
8. Bartl, M. H.; Boettcher, S. W.; Frindell, K. L.; Stucky, G. D. 3-D molecular assembly of function in titania-based composite material systems. *Acct. Chem. Res*. **2005**, *36*, 263-271.
9. Zeng, F.; Zimmerman, S. C. Dendrimers in supramolecular chemistry: from molecular recognition to self-assembly. *Chem. Rev.* **1997**, *97*, 1681-1712.
10. Li, J.; Möhwald, H.; An, Z.; Lu, G. Molecular assembly of biomimetic microcapsules. *Soft Matter* **2005**, *1*,259-264.
11. Gao, X.; Yang, L.; Petros, J. A.; Marshall, F. F.; Simons, J. W.; Nie, S. *In vivo* molecular and cellular imaging with quantum dots. *Curr. Opin. Biotech.* **2005**, *1*, 63-72.
12. Duan, J.; Zhang, H.; Tang, Q.; He, B.; Yu, L. Recent advances in critical materials for quantum dot- sensitized solar cells: a review. *J. Mater. Chem. A.* **2015**, *3*, 17497-17510.
13. Shirasaki, Y.; Supran, G. J.; Bawendi, M. G.; Bulović, V. Emergence of colloidal quantum-dot light-emitting technologies. *Nature Photonics* **2013**, *7*, 13-23.
14. Choi, H.; Nahm, C.; Kim, J.; Kim, C.; Kang, S.; Hwang, T.; Park, B. Review paper: Toward highly efficient quantum-dot and dye-sensitized solar cells. *Curr. Appl. Phys.* **2012**, *13*, S2-S13.
15. Kim, J. Y.; Voznyy, O.; Zhitomirsky, D.; Sargent, E.H. Colloidal quantum dot materials and devices: a quarter-centry of advances. *Adv. Mater.* **2013**, *25*, 4986-5010.
16. Gao, J.; Gu, H.; Xu, B. Multifunctional magnetic nanoparticles: design, synthesis, and biomedical applications. *Acc. Chem. Res.* **2009**, *42*, 1097-1107.

17. Chen, G.; Roy, I.; Yang, C.; Prasad, P. N. Nanochemistry and nanomedicine for nanoparticle-based diagnostics and therapy. *Chem. Rev.* **2016**, *116*, 2826-2885.
18. Johnstone, T. C.; Suntharalingam, K.; Lippard, S. J. The next generation of platinum drugs: targeted Pt(II) agents, nanoparticle delivery, and Pt(IV) prodrugs. *Chem. Rev.* **2016**, 3436-3486.
19. Chinen, A. B.; Guan, C. M.; Ferrer, J. R.; Barnaby, S. N.; Merkel, T. J.; Mirkin, C. A. Nanoparticle probes for the detection of cancer biomarkers, cells, and tissues by fluorescence. *Chem. Rev.* **2015**, *115*, 10530-10574.
20. Kim, B. H.; Hackett, M. J.; Park, J.; Hyeon, T. Synthesis, characterization, and application of ultrasmall nanoparticles. *Chem. Mater.* **2014**, *26*, 59-71.
21. Oster, G.; Wang, H. How Protein Motors Convert Chemical Energy into Mechanical Work, in Molecular Motors (ed M. Schliwa), Wiley-VCH Verlag GmbH & Co. KGaA, Weinheim, FRG
22. Starikov, E. B.; Panas, I.; Norden, B. Chemical-to-mechanical energy coversion in biomacromolecular machines: a plasmon and optimum control theory for directional work. *J. Phys. Chem. B.* **2008**, *112*, 8319–8329.
23. Hess, V. Self-assembly driven by molecular motors. *Soft Matter* **2006**, 2, 669-677.
24. Paxton, W. F.; Sundararajan, S.; Mallouk, T. E.; Sen, A. Chemical locomotion. *Angew. Chem. Int. Ed.* **2006**, *45*, 5420–29.
25. Goel, A.; Vogel, V. Harnessing biological motors to engineer systems for nanoscale transport and assembly. *Nat. Nanotechnol*. **2008**, *3*, 465–475.
26. Hess, H.; Vogel, V. Molecular shuttles based on motor proteins: active transport in synthetic environments. *Rev. Mol. Biotechnol.* **2001**, *82*, 67–85.
27. Limberis, L.; Stewart, R. J. Toward kinesin-powered microdevices. *Nanotechnology* **2000**, *11*, 47–51.
28. Soong, R. K.; Bachand, G. D.; Neves, H. P.; Olkhovets, A. G.; Craighead, H. G.; Montemagno, C. D. Powering an inorganic nanodevice with a biomolecular motor. *Science* **2000**, *290*, 1555–58.
29. Böhm, K. J.; Stracke, R.; Mühlig, P.; Unger, E. Motor protein–driven unidirectional transport of micrometer-sized cargoes across isopolar microtubule arrays. *Nanotechnology* **2001**, *12*, 238–44
30. Browne, W. R.; Feringa, B. L. Making molecular machines work. *Nat. Nanotechnol.* **2006**, *1*, 25–35
31. Ismagilov, R. F.; Schwartz, A.; Bowden, N.; Whitesides, G. M. Autonomous movement and self-assembly. *Angew. Chem. Int. Ed.* **2002,** *41*, 652-54.
32. Paxton, W. F.; Kistler, K. C.; Olmeda, C. C.; Sen, A.; St. Angelo, S. K.; Cao, Y.; Mallouk, T. E.; Lammert, P. E.; Crespi, V. H. Catalytic nanomotors: autonomous movement of striped nanorods. *J. Am. Chem. Soc.* **2004**, *126*, 13424-31.
33. Fournier-Bidoz, S.; Arsenault, A.; Manners, I.; Ozin, G. A. Synthetic self – propelled nanorotors. *Chem. Commun.* **2005**, 441-443.

34. Dey, K. K.; Wong, F.; Altemose, A.; Sen, A. Catalytic motors – quo vadimus? *Curr. Opin. Coll. Interface Sci.* **2016**, *21*, 4-13.
35. Wong, F.; Dey, K. K.; Sen, A. Synthetic micro/nanomotors and pumps: fabrication and applications. *Annu. Rev. Mater. Res.* **2016**, *46*, 407-432.
36. Duan, W.; Wang, W.; Das, S.; Yadav, V.; Mallouk, T. E.; Sen, A. Synthetic nano- and micromachines in analytical chemistry: sensing, migration, capture, delivery, and separation. *Annu. Rev. Anal. Chem.* **2016**, *8*, 311-333.
37. Ebbens, S. J. Active colloids: Progress and challenges towards realizing autonomous applications. *Curr. Opin. Colloid Interf. Sci.* **2016**, *21*¸14-23.
38. Gao, W.; Wang, J. Synthetic micro/nanomotors in drug delivery. *Nanoscale* **2014**, *6*, 10486-10494.
39. Sánchez, S.; Soler, L.; Katuri, J. Chemically powered micro- and nanomtors. *Angew. Chem. Int. Ed.* **2014**, *54*, 1414-1444.
40. Gibbs, J.; Zhao, Y. Catalytic nanomotors: fabrication, mechanism, and applications. *Frontiers of Mater. Sci.* **2011**, *5*, 25-39.
41. Kapral, R. Perspective: Nanomotors without moving parts that propel themselves in solution. *J. Chem. Phys.* **2013**, *138*, 020901
42. Abbott, J. J.; Peyer, K. E.; Lagomarsino, M. C.; Zhang, L.; Dong, L.; Kaliakatsos, I. K.; Nelson, B. J. How Should Microrobots Swim? *Int. J. Robot. Res.* **2009**, *28*, 1434-1447.
43. Purcell, E. M. Life at Low Reynolds-Number. *Am. J. Phys.* **1977**, *45*, 3-11.
44. Song, J.; Ewoldt, R. H.; Hu, W.; Craig Silvis, H.; Macosko, C. W. Flow accelerates adhesion between functional polyethylene and polyurethane. *AlChE J.* **2011**, *57*, 3496-3506.
45. Song, J.; Bringuier, A.; Kobayashi, S.; Baker, A. M.; Macosko, C. W. Adhesion between polyethylenes and different types of polypropylenes. *Polym. J.* **2012**, *44*, 939-945.
46. Song, J.; Baker, A. M.; Macosko, C. W.; Ewoldt, R. H. Reactive coupling between immiscible polymer chains: Acceleration by compressive flow. *AlChE J.* **2013**, *59*, 3391-3402.
47. Song, J.; Thurber, C. M.; Kobayashi, S.; Baker, A. M.; Macosko, C. W.; Silvis, H. C. Blends of polyolefin/PMMA for improved scratch resistance, adhesion and compatibility. *Polymer* **2012**, *53*, 3636-3641.
48. Paxton, W. F.; Baker, P. T.; Kline, T. R.; Wang, Y.; Mallouk, T. E.; Sen, A. Catalytically Induced Electrokinetics for Motors and Micropumps. *J. Am. Chem. Soc.* **2006**, *128*, 14881-8.
49. Kline, T. R.; Iwata, J.; Lammert, P. E.; Mallouk, T. E.; Sen, A.; Velegol, D. Catalytically Driven Colloidal Patterning and Transport. *J. Phys. Chem. B* **2006**, *110*, 24513-21.
50. Wang, Y.; Hernandez, R. M.; Bartlett, D. J.; Bingham, J. M.; Kline, T. R.; Sen, A.; Mallouk, T. E. Bipolar electrochemical mechanism for the propulsion of catalytic nanomotors in hydrogen peroxide solutions. *Langmuir* **2006**, *22*, 10451-10456.
51. Moran, J. L.; Posner, J. D. Electrokinetic locomotion due to reaction-induced charge auto-electrophoresis. *J. Fluid Mech.* **2011**, *680*, 31-66.

52. Yariv, E. Electrokinetic self-propulsion by inhomogeneous surface kinetics. *Proc. R. Soc. A* **2010**, *467*, 1645-1664.
53. Hong, Y.; Blackman, N. M. K.; Kopp, N. D.; Sen, A.; Velegol, D. Chemotaxis of Nonbiological Colloidal Rods. *Phys. Rev. Lett*. **2007**, **99**, 178103.
54. Magdanz, V.; Guix, M.; Schmidt, O. G. Tubular micromotors: from microjets to spermbots. *Robotics and Biomimetics* **2014**, *1*, 11.
55. Gao, W.; Sattayasamitsathit, S.; Orozco, J.; Wang, J. Highly efficient catalytic microengines: template electrosynthesis of polyaniline/platinum microtubes. *J. Am. Chem. Soc.* **2011**, *133* 11862–4.
56. Mei, Y.; Huang, G.; Solovev, A. A.; Urena, E. B.; Monch, I,; Ding, F.; Reindl, T. Fu, R. K. Y.; Chu, P. K. Schmidt, O. G. Versatile approach for integrative and functionalized tubes by strain engineering of nanomembranes on polymers, *Adv. Mater.* **2008**, *20*, 4085–90.
57. Harazim, S. M.; Xi, W.; Schmidt, C. K.; Sanchez, S.; Schmidt, O. G. Fabrication and applications of large arrays of multifunctional rolled-up SiO/SiO2 microtubes. *J. Mater. Chem*. **2012**, *22*, 2878–84
58. Mei, Y. Solovev, A. A.; Sanchez, S.; Schmidt, O. G. Rolled-up nanotech on polymers: from basic perception to self-propelled catalytic microengines. *Chem. Soc. Rev*. **2011**, *40*, 2109–19.
59. Solovev, A. A.; Sanchez, S.; Mei, Y.; Schmidt, O. G. Tunable Catalytic Tubular Micro-Pumps Operating at Low Concentrations of Hydrogen Peroxide. *Phys. Chem. Chem.Phys*. **2011**, *13*, 10131-10135.
60. Wang, H.; Moo, J. G. S.; Pumera, M. From nanomotors to micromotors: the influence of the size of an autonomous bubble-propelled device upon its motion. *ACS Nano* **2016**, *10*, 5041-5050.
61. Vicario, J.; Eelkema, R.; Browne, W. R.; Meetsma, A.; La Crois, R. M.; Feringa, B. L. Catalytic molecular motors: fueling autonomous movement by a surface bound synthetic manganese catalase. *Chem. Commun.* **2005** 3936-38.
62. Sanchez, S.; Solovev, A. A.; Schulze, S.; Schmidt, O. G. Controlled manipulation of multiple cells using catalytic microbots. *Chem. Commun.* **2011**, 47, 698-700.
63. Baraban, L.; Harazim, S. M.; Sanchez, S.; Schmidt, O. G. Chemotactic behavior of catalytic motors in microfluidic channels. *Angew. Chem. Int. Ed.* **2013**, *52*, 5552-56.
64. Manesh, K. M.; Cardona, M.; Yuan, R.; Clark, M.; Kagan, D.; Balasubramanian, S.; Wang, J. Template-assisted fabrication of salt-independent catalytic tubular microengines. *ACS Nano* **2010**, *4*, 1799–804.
65. Gao, W.; Manesh, K. M.; Hua, J.; Sattayasamitsathit, S.; Wang, J. Hybrid nanomotor: a catalytically/magnetically powered adaptive nanowire swimmer. *Small* **2011**, *7*, 2047–51.
66. Zhao, G.; Pumera, M. Magnetotactic artificial self-propelled nanojets. *Langmuir* **2012**, *29*, 7411–15.
67. Zhao, G.; Ambrosi, A.; Pumera, M. Self-propelled nanojets via template electrodeposition. *Nanoscale* **2013**, *5*, 1319–24.

68. Wilson, D. A.; Nolte, R. J. M.; van Hest, J. C. M. Autonomous movement of platinum-loaded stomatocytes. *Nat. Chem.* **2012**, *4*, 268–74.
69. Gibbs, J. G.; Zhao, Y. P. Autonomously motile catalytic nanomotors by bubble propulsion. *Appl. Phys. Lett.* **2009**, *94*, 163104–3.
70. Wheat, P. M.; Marine, N. A.; Moran, J. L.; Posner, J. D. Rapid fabrication of bimetallic spherical motors. *Langmuir* **2010**, *26*, 13052-55.
71. Orozco, J.; Garcia-Gradilla, V.; D'Agostino, M.; Gao, W.; Cortes, A.; Wang, J. Artificial enzyme-powered microfish for water-quality testing. *ACS Nano* **2013**, *7*, 818-824.
72. Gu, Y.; Sattayasamitsathit, S.; Kaufmann, K.; Vazquez-Duhalt, R.; Gao, W.; Wang, C.; Wang, J. Self-propelled chemically-powered plant-tissue biomotors. *Chem. Commun.* **2013**, *49*, 7307-7309.
73. Ibele, M.; Mallouk, T. E.; Sen, A. Schooling behavior of light-powered autonomous micromotors in water. *Angew. Chem. Int. Ed.* **2009**, *48*, 3308–12.
74. Ibele, M. E.; Lammert, P. E.; Crespi, V. H.; Sen, A. Emergent, collective oscillations of self-mobile particles and patterned surfaces under redox conditions. *ACS Nano* **2010**, *4*, 4845–51
75. Hong, Y.; Diaz, M.; Córdova-Figueroa, U. M.; Sen, A. Light-driven titanium-dioxide based reversible microfireworks and micromotor/micropump systems. *Adv. Funct. Mater.* **2010**, *20*, 1568–76.
76. Duan, W.; Liu, R.; Sen, A. Transition between collective behaviors of micromotors in response to different stimuli. *J. Am. Chem. Soc.* **2013**, *135*, 1280–83.
77. Sen, A.; Ibele, M.; Hong, Y.; Velegol, D. Chemo and phototactic nano/microbots. *Faraday Discuss.* **2009**, *143*, 15–27.
78. Kar, A.; Chiang, T.; Rivera, I.O..; Sen, A.; Velegol, D. Enhanced transport into and out of dead-end pores. *ACS Nano* **2015**, *9*, 746–53.
79. Yadav, V.; Freedman, J. D.; Grinstaff, M.; Sen, A. Bone-crack detection, targeting, and repair using ion gradients. *Angew. Chem.* **2013**, *52*, 10997–1001.
80. Mou, F.; Chen, C.; Zhong, Q.; Yin, Y.; Ma, H.; Guan, J. Autonomous motion and temperature-controlled drug delivery of Mg/Pt-poly(*N*-isopropylacrylamide) Janus micromotors driven by simulated body fluid and blood plasma. *ACS Appl. Mater. Interfaces* **2014**, *6*, 9897–903.
81. Gao, W.; Pei, A.; Wang, J. Water-driven micromotors. *ACS Nano* **2012**, *6*, 8432-38.
82. Gao, W.; Feng, X.; Pei, A.; Gu, Y.; Li, J.; Wang, J. Seawater-driven magnesium based Janus micromotors for environmental remediation. *Nanoscale* **2013**, *5*, 4696-700.
83. Soler, L.; Magdanz, V.; Fomin, V. M.; Sanchez, S.; Schmidt, O. G. Self-propelled micromotors for cleaning polluted water. *ACS Nano* **2013**, *7*, 9611-20.
84. Soler, L.; Sanchez, S. Catalytic nanomotors for environmental monitoring and water remediation. *Nanoscale* **2014**, *6*, 7175-7182.
85. Li, J.; Singh, V, Sattayasamitsathit, S.; Orozco, J.; Kaufmann, K.; Dong, R.; Gao, W.; Jurado-Sanchez, B.; Fedorak, Y.; Wang, J. Water-driven micromotors for rapid photocatalytic degradation of biological and chemical warfare agents. *ACS Nano* **2014**, *8*, 11118–25

86. Pavlick, R. A.; Dey, K. K.; Sirjoosingh, A.; Benesi, A.; Sen, A. A catalytically driven organometallic molecular motor. *Nanoscale* **2013**, *5*, 1301–4.
87. Pavlick, R. A.; Sengupta, S.; McFadden, T.; Zhang, H.; Sen, A. A polymerization-powered motor. *Angew. Chem. Int. Ed.* **2011**, *50*, 9374–77.
88. Venkataraman, S.; Dirks, R. M.; Rothemund, P. W. K.; Winfree, E.; Pierce, N. A. An autonomous polymerization motor powered by DNA hybridization. *Nat. Nanotechnol.* **2007**, *2*, 490–94.
89. Dey, K. K.; Pong, F. Y.; Breffke, J.; Pavlick, R.; Hatzakis, E.; Pacheco, C.; Sen, A. Dynamic coupling at the angstrom scale. *Angew. Chem. Int. Ed.* **2016**, *128*, 1125-1129.
90. Zhang, H.; Yeung, K.; Robbins, J. S.; Pavlick, R. A.; Wu, M.; Liu, R.; Sen, A.; Phillips, S. T. Self-powered microscale pumps based on analyte-initiated depolymerization reactions. *Angew. Chem. Int. Ed.* **2012**, *51*, 2400–4.
91. Zhang, H.; Duan, W.; Lu, M.; Zhao, X.; Shklyaev S.; Liu, L.; Huang, T. J. Sen, A. Self-powered glucose-responsive micropumps. *ACS Nano* **2014**, *8*, 8537–42.
92. DiLauro, A. M.; Zhang, H.; Baker, M. S.; Wong, F.; Sen, A,; Phillips, S. T. Accessibility of responsive endcaps in films composed of stimuli-responsive, depolymerizable poly(phthalaldehydes). *Macromolecules* **2014**, *46*, 7257–65.
93. Zhang, H.; Duan, W.; Liu, L.; Sen, A. Depolymerization-powered autonomous motors using biocompatible fuel. *J. Am. Chem. Soc.* **2013**, *135*, 15734–37.
94. Shin, J-S.; Pierce, N. A. A Synthetic DNA walker for molecular transport. *J. Am. Chem. Soc.* **2004**, *126*, 10834–35.
95. Sherman, W. B.; Seeman, N. C. A precisely controlledDNS biped walking device. *Nano Lett.* **2004**, *4*, 1203–7.
96. Pantarotto, D.; Browne, W. R.; Feringa, B. L. Autonomous propulsion of carbon nanotubes powered by a multienzyme ensemble. *Chem. Commun.* **2008**, 1533–35.
97. Pavel. I-A.; Bunea, A-I.; David, S.; Gaspar, S. Nanorods with biocatalytically induced selfelectrophoresis. *Chem. Catal. Chem.* **2014**. *6*, 866–72.
98. Sengupta, S.; Dey, K. K.; Muddana, H. S.; Tabouillot, T.; Ibele, M. E.; Butler, P. J.; Sen, A. Enzyme molecules as nanomotors. *J. Am. Chem. Soc.* **2013**, *135*, 1406–14.
99. Sengupta, S.; Spiering, M. M.; Dey, K. K.; Duan, W.; Patra, D.; Butler, P. J.; Astumian, R. D.; Benkovic, S. J.; Sen, A. DNA polymerase as a molecular motor and pump. *ACS Nano* **2014**, *8*, 2410–18.
100. Muddana, H. S.; Sengupta, S.; Mallouk, T. E.; Sen, A.; Butler, P. J. Substrate catalysis enhances single enzyme diffusion. *J. Am. Chem. Soc.* **2010**, *132*, 2110–11.
101. Butler, P. J.; Dey, K. K.; Sen, A. Impulsive enzymes: a new force in mechanobiology. *Cell. Mol. Bioeng.* **2015**, *8*, 106–18.
102. Sengupta, S.; Patra, D.; Rivera, I. O.; Agrawal, A.; Shklyaev, S.; Dey, K. K.; Córdova-Figueroa, U.; Mallouk, T. E.; Sen, A. Self-powered enzyme micropumps. *Nat. Chem.* **2014**, *6*, 415–22.

103. Shklyaev, O. E.; Shum, H.; Sen, A.; Balazs, A. C. Harnessing Surface-bound Enzymatic Reactions to Organize Microcapsules in Solution. *Science Advances* **2016**, *2*, e1501835.
104. Ortiz-Rivera, I.; Shum, H.; Agrawal, A.; Sen, A, Balazs, A. C. Convective Flow Reversal in Self-powered Enzyme Micropumps. *Proc. Nat. Acad. Sci. USA* **2016**, *113*, 2585.
105. Dey, K. K.; Zhao, X.; Tansi, B. M.; Méndez-Ortiz, W. J.; Córdova-Figueroa, U. M.; Golestanian, R.; Sen, A. Micromotors Powered by Enzyme Catalysis. *Nano Letters* **2015**, *15*, 8311.
106. Dey, K. K.; Das, S.; Poyton, M. F.; Sengupta, S.; Butler, P. J.; Cremer, P. S.; Sen, A. Chemotactic separation of enzymes. *ACS Nano* **2014**, *8*, 11941–49.

# Chapter 2 Highly efficient light-harvesting nanomotor using halogen media

## 2.1 Introduction

While we have become proficient at fabricating and manipulating materials on the micro and nanoscale, the ability to control the motion of the materials themselves is still an underdeveloped field. In an effort to emulate and understand motion on the nanoscale, various types of synthetic nanomotors have been fabricated and characterized over the last decade.[1-5] Amongst the different types of nanomotors, self-electrophoretic motors are of particular interest due to the electric field generated by the motors themselves that lead to directed motion. The first self-electrophoretic motor synthesized was a bimetallic nanorod composed of gold and platinum segments (Au-Pt), synthesized by Mallouk and Sen in 2004.[6-8] The bimetallic nanorod exhibit directed motion, moving at 5-20 μm/s. The asymmetric decomposition of hydrogen peroxide ($H_2O_2$) occurring at opposing end of the motor leads to the self-electrophoresis.[8-11]

Using $H_2O_2$ as the fuel source, a wide variety of metallic motors have been synthesized and shown to move by a similar mechanism.[12-16] However, $H_2O_2$ is far from the perfect fuel source. Aside from the asymmetric electrochemical decomposition as a result of the short-circuit between platinum and gold, there is a second decomposition reaction that occurs solely on platinum.[6] This leads to loss of fuel through routes that do not lead to propulsion. Peroxide decomposition also releases oxygen, leading to bubble formation. Liu and Sen developed an efficient, bubble-free self-electrophoretic bimetallic motor consisting of copper and platinum (Cu-Pt). The nanomotor acts as a nanobattery in dilute aqueous bromine ($Br_2$) or iodine ($I_2$) solutions. This bimetallic motor exhibits directed motion with speeds of about 10-20 μm/s.[17]

We have continued to seek more efficient motor designs. There have been examples in the literature regarding light-driven or light-assisted motors; e.g. Janus $TiO_2$ microparticles,[18-20] silver-salt microparticles,[21-23] DNA walker molecules.[24] These, however, use light as its primary or secondary fuel, meaning discontinued use of light will cause the motor function to cease. A particularly intriguing possibility involves using light to reverse the redox reaction that causes electrophoretic propulsion. This will lead to the regeneration of the fuel; in essence, the energy for propulsion will be derived ultimately from light with the bipolar redox reaction merely acting as the conduit for the conversion of light energy to mechanical motion (Figure 2-1). In this chapter, a highly efficient, light-modulated, self-electrophoretic bimetallic Ag-Pt motor based on the reversible reaction of silver with iodine ($I_2$) is reported. The reaction involves the following steps: (a) bipolar redox reaction leading to the conversion of Ag to AgI resulting in propulsion and (b) photochemical decomposition of AgI back to elemental silver (Ag) and $I_2$.[25,26]

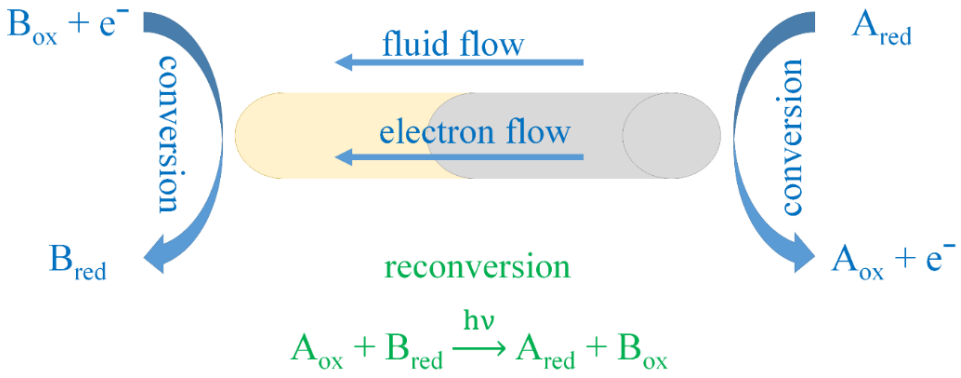


**Figure 2-1**. Generalized scheme for the regeneration of fuel, allowing for continued motion of light-assisted self-electrophoretic motor.

## 2.2 Experimental details

### 2.2.1 Fabrication

Whatman Anodisc anodized aluminum oxide membranes with 0.02 μm pores (Whatman Anodisc 6809-5022) were sputtered with a 200 nm layer of sacrificial metal (usually copper) using Kurt Lesker CMS-18/RF sputtering system. Using this conductive layer as the working electrode, a segment of metal can be synthesized galvanostatically on a Bio-logic SP-150 potentiostat. All potentials were measured relative to an Ag/AgCl reference electrode and a platinum wire serves as the counter electrode.

In the copper sputtered AAO templates, a segment of sacrificial copper was first deposited (-1.2 V/cm$^2$) for 2 minutes from a solution of copper sulfate pentahydrate (100 g/L), ammonium sulfate (20 g/L), and diethylenetriamine (76.4g/L). Following deposition and rinsing, a 1 μm segment of inert metal, platinum (deposited at -0.3 mA/cm$^2$ for 40 minutes), was electrodeposited from a commercial solution (Technic Platinum TP RTU solution, 5 g/L, Part #240451GL). Following the deposition of platinum, a final segment of silver (1 or 2 μm) was synthesized, using a 0.1M solution of potassium silver cyanide at -0.9V/cm$^2$ for 200 mC or, alternatively, a solution of silver chloride, sodium thiosulfate, and potassium disulfite at -0.5 mA/cm$^2$.[33] This method produces nanorods with dimensions of 400 μm in width and 2-3 μm in length. Aside from platinum, other materials (such as gold and poly(3,4-ethylenedioxythiophene) were made in conjunction of silver as well. Gold was electrodeposited using Orotemp 24 RTU Rack commercial deposition solution containing 0.264 Troy oz per liter (deposited at -0.9 V/cm$^2$ for 300mC). Poly(3,4-ethylenedioxythiophene (PEDOT) was deposited after silver deposition using a 0.1 M solution of 3,4-ethylenedioxythiophene (EDOT, 97% purchased from Aldrich) in 0.1 M lithium

perchlorate in acetonitrile (deposited at -0.9 V/cm$^2$). For removal of the template and dispersion of the nanorods, the sputtered copper was selectively etched using a commercial copper etchant (Transene Copper Etch BTP). To remove a sacrificial silver backing, a solution of 3 M nitric acid was used. The alumina template was subsequently removed by a 3 M sodium hydroxide (NaOH) solution. Alternatively, the template can be etched using 5-10% hydrogen fluoride (HF). The rods were then centrifuged and washed by deionized water at least 8 times. Sample was finally dispersed in 1 mL of deionized water.

### 2.2.2 Experimental setup

Final nanorod sample was diluted to 25% and sonicated briefly to ensure uniformity. 10 µL of this solution was placed inside a circular well (9 mm diameter, 1 mm deep, Grace Bio Labs FastWells SKU 664112) that was adhered to a microscope glass slide and open to air. The purpose of the well was to prevent solution migration after addition of solution and to ensure uniform spread and thickness. 10 µL of a stock iodine solution was added as fuel for the nanorods. Iodine exposure concentrations in this dissertation are reported as final solution concentration of iodine present in the sample (Table 2-1). The nanorod sample were then imaged with a Zeiss Axiovert 200 MAT optical microscope and the individual nanorod movement were tracked and analyzed using Tracker video analysis software (by Cabrillo).

**Table 2-1**. Iodine stock solution concentrations and actual iodine concentration in experimental sample after addition.

| $I_2$ | Stock [$I_2$] (mM) | After Addition (mM) |
|---|---|---|
| 2.5% | 0.02818 | 0.01409 |
| 5% | 0.05635 | 0.028175 |
| 7.50 | 0.08453 | 0.042265 |
| 10% | 0.1127 | 0.05635 |
| 15% | 0.1691 | 0.08455 |
| 20% | 0.2254 | 0.1127 |

### 2.2.3 Characterization

*Electron Microscopy* – Scanning electron microscopy (SEM) images were obtained using the Nova NanoSEM630 field emission scanning electron microscope at 5 kV (Landing voltage of 5 keV) with a working distance below 5 mm using the TLD detector. Energy-dispersive X-ray spectroscopy (EDS) data was obtained using 10 kV accelerating voltage. Transmission electron microscopy (TEM) and scanning electron microscopy (STEM) images were collected by FEI Titan TEM with dual correctors with EELS and EDS capabilities at 200 kV.

*Open Potential Measurements* – Measurements were taken on a BioLogic SP-150 Potentiostat using 99.999% Platinum and Silver foils purchased from Alfa Aesar. The silver foil was connected to the working electrode while the platinum foil was connected to the counter electrode, with the reference electrode short-circuited to the counter. 1 $cm^2$ areas on each foil was exposed to iodine solutions about 1 cm apart. The potential measurements were measured and the value was recorded at 5 min after exposure when the measurement has leveled out.

## 2.3 Autonomous motion of Ag-based Nanomotors

### 2.3.1 Directed linear motion of nanorods

In aqueous iodine solutions, the motion of the Ag-Pt nanorods is visibly non-Brownian. We can characterize the motion of the nanorods by tracking the motors' position over time after iodine exposure. Figure 2-2 shows the trace of a single Ag-Pt nanomotor at different time stamps in 28 µM iodine.

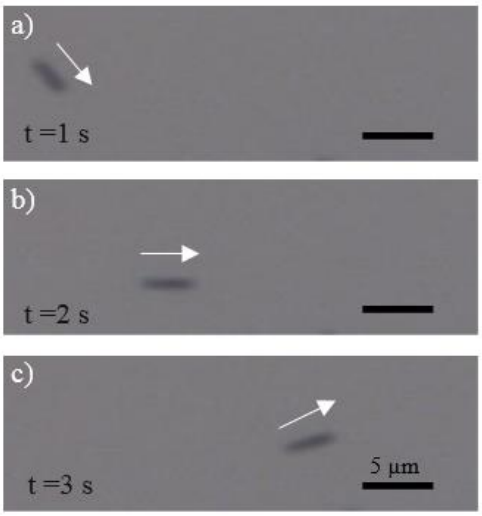


**Figure 2-2**. Cropped frames of a single moving Ag-Pt nanomotor at different time stamps in 28 µM $I_2$ solution. The nanomotor is moving at 6.34 µm/s.

It was found that varying the iodine concentration significantly impacted the nanomotor speeds, with the nanomotors moving 2-3 µm/s at low iodine concentrations of 14.1 µM $I_2$ while moving 20 µm/s at 113 µM $I_2$. Figure 2-3 shows nanomotor speeds at different iodine concentrations with their corresponding current density, measured as described in the experimental

section. Both motor speed and current density of the system have a strong linear correlation to iodine concentration.

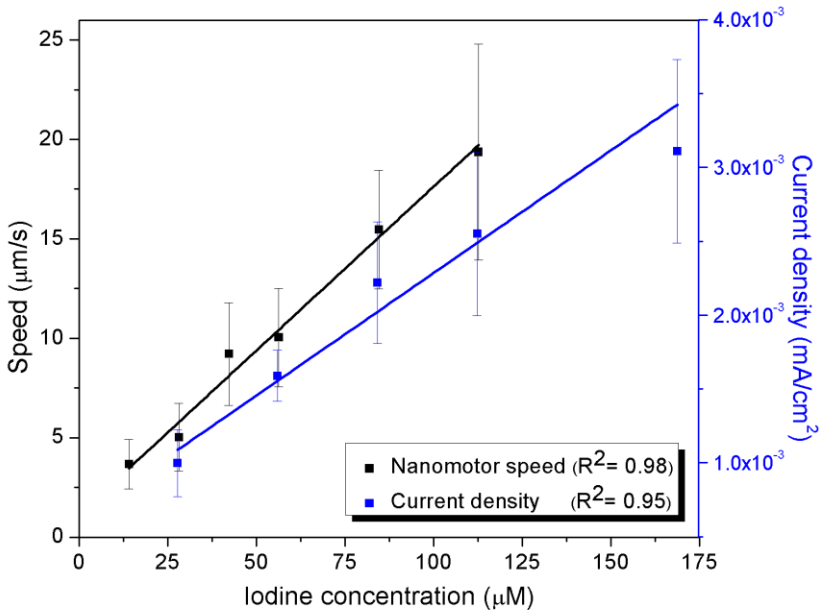


**Figure 2-3**. Ag-Pt nanomotor speeds at different iodine concentrations during initial exposures (speeds recorded over 5 seconds and averaged) and the corresponding current density.

### 2.3.2 Motor Characterization

In order for silver-based nanomotors to move in iodine fuel, an asymmetry must be present in the nanorod formation. Therefore, bi-segmented nanorod architecture was used. To visualize the difference between normal nanorods and the converted AgI rods, electron microscopy (SEM, STEM) and energy dispersive spectroscopy (EDS) were used to characterize the surface of the rods.

Initial trials focused on gold-silver (Ag-Au) nanorods as the intrinsic coloring of the segments makes characterization under the microscope ideal. These motors move at an extremely rapid initial spurt and then stops abruptly. This may be due to iodine etching the gold in addition

to reacting with the silver to power the motor, leading to extremely rapid consumption of iodine fuel. When examined under SEM (Figure 2-4), it can be seen that the entire length of the nanorods have uneven surface detailing, indicating reaction of both the gold and silver segment.

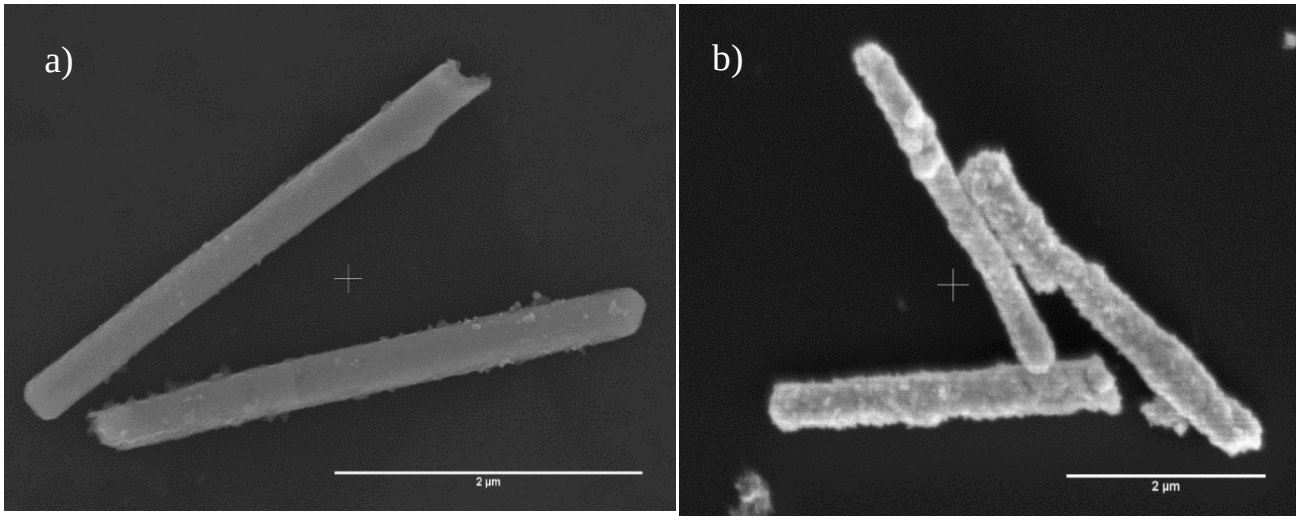


**Figure 2-4**. Pre-exposure (a) and post-exposure (b) SEM images of Ag-Au nanomotors. Pre-exposure, it one can easily see both gold and silver segments is uniform and smooth. Post-exposure, it is difficult to determine the segments as both sides have rough surface detailing, alluding to the reaction of both metals in iodine. Scale bars are 2 µm.

Due to the problems presented by the Ag-Au system, gold was replaced by platinum. Ag-Pt nanorods were found to be excellent motors owing to the non-reactive nature of platinum. Platinum, however, is not without its drawbacks. It was found that during electrodeposition silver did not adhere well to the deposited platinum segment. This can result in breakage of nanorods when sonicated for extended periods of time. Figure 2-5 is an SEM image of electrodeposited Ag-Pt nanorods, showing a rough transition between the two metals in comparison to Figure 2-4A, which has a smooth transition between gold and silver. Therefore, during fabrication and subsequent sonications, care was taken to ensure adequate silver deposition solution and brief periods of sonication to prevent dissociation of the platinum and silver segments.

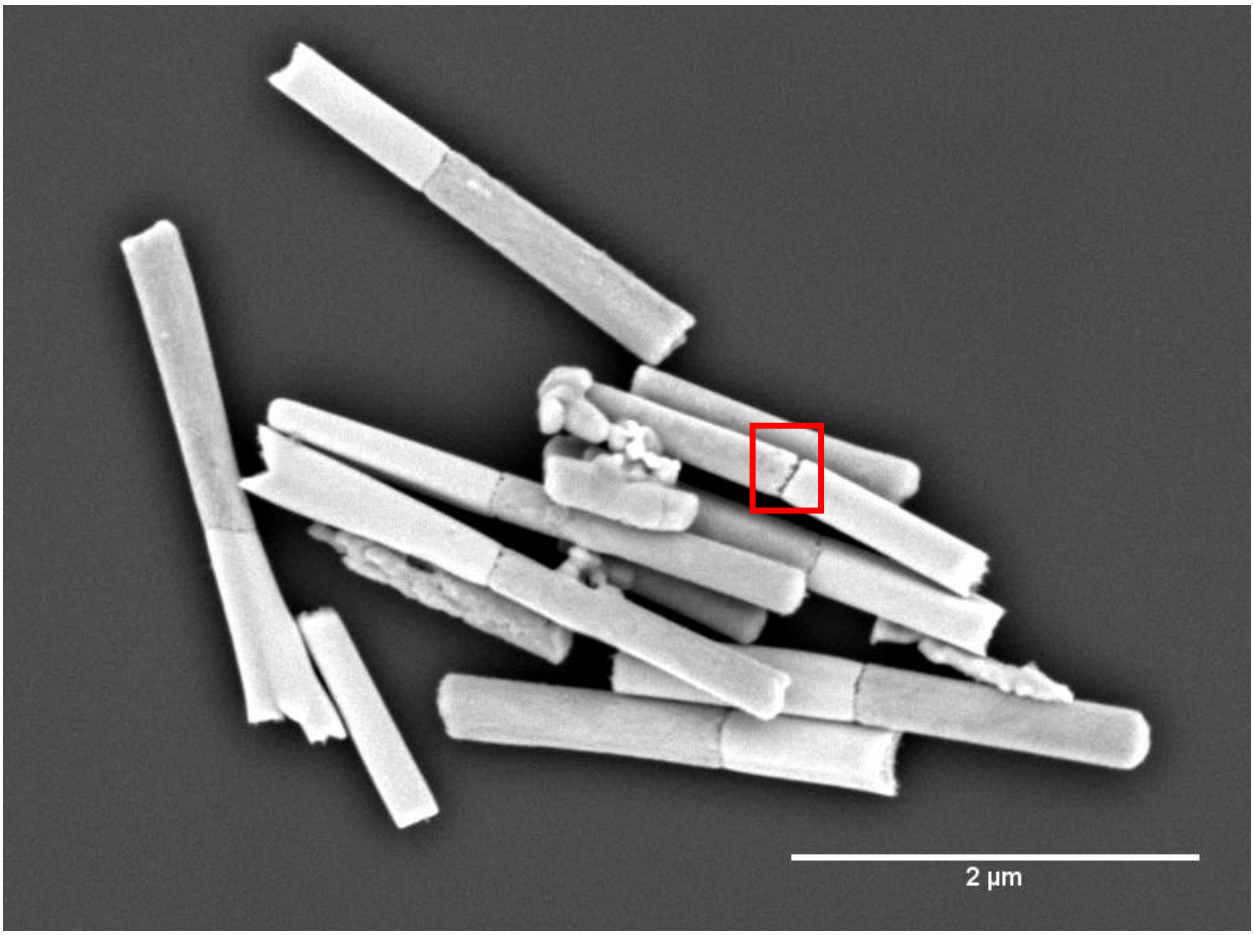


**Figure 2-5**. Ag-Pt nanorods after electrodeposition and subsequent release. A cleft between the two segments can be seen in the SEM image, a result of mild adhesion incompatibility of the two metals (red highlight).

Figure 2-6 compares pure Ag-Pt rods (a) to Ag-Pt rods treated with iodine (b). The platinum segment is attached to a smooth silver segment with a distinct interface in pure Ag-Pt nanorods. After exposure to 0.05 mM iodine (Figure 2-6B), the platinum surface remains relatively unchanged while the silver surface becomes uneven and develops ridges. This is due to the increase in volume of the rod after conversion. Based on the molecular weight and mass density of AgI and Ag, we can calculate the volume ratios of AgI/Ag to be $V_{AgI/Ag} = 4.02$.

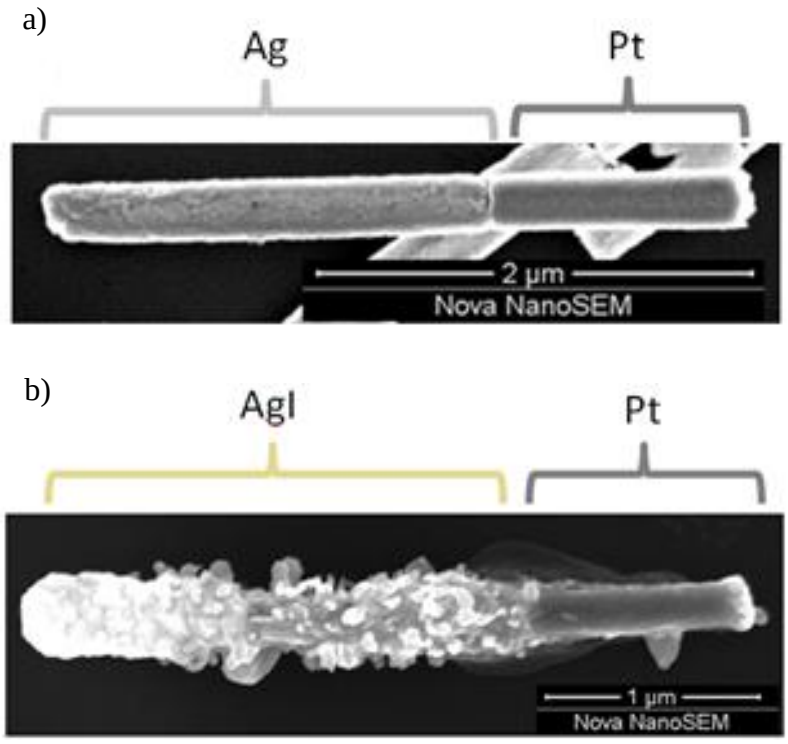


**Figure 2-6**. SEM Images of (a) pure Ag-Pt nanorods and (b) Ag-Pt nanorods after exposure to iodine, turning it into AgI-Pt nanorods. Images were taken using a Nova NanoSEM630.

To further characterize the conversion, STEM/EDS was used to elucidate whether Ag to AgI conversion was complete as well as the extent of the conversion. Figure 2-7 shows an EDS map scan of a reacted nanomotor taken at 200 kV using a FEI Titan TEM, clearly distinguishing between the silver iodide and the platinum domains.

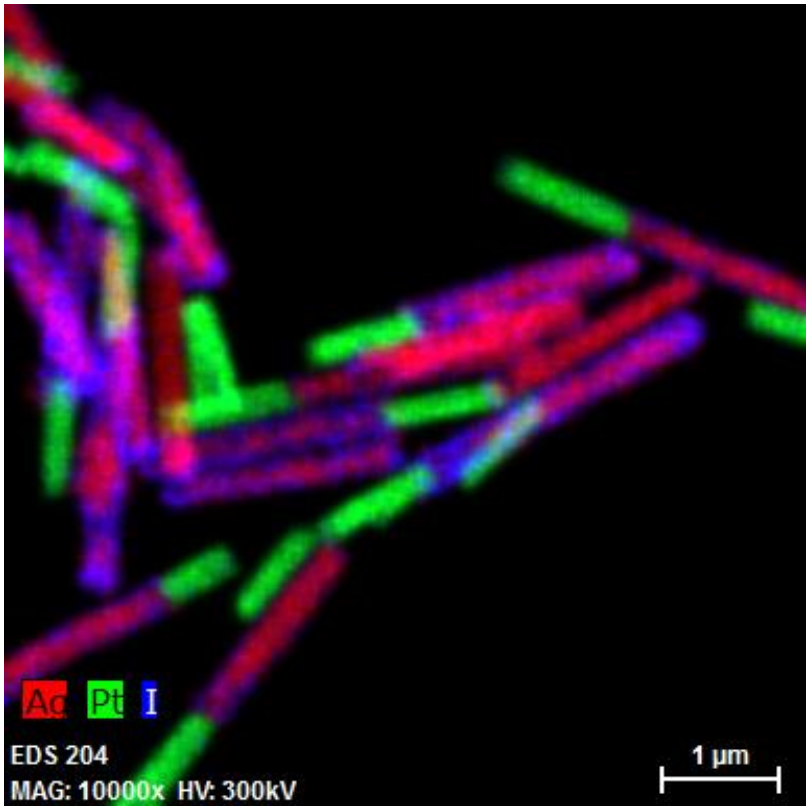


**Figure 2-7**. EDS map data of a converted AgI-Pt nanorod after exposure to 28 µM $I_2$. The data was obtained at 200 kV using a FEI Titan TEM.

Detailed ratios for Ag:I EDS data were taken from EDS spectra obtained through EDS mapping in STEM mode. Line scans across the converted silver segment shows there is slightly higher iodide content near the edge of the rod, hinting at the silver iodide conversion forming a shell around an unreacted silver core (Figure 2-8). Figure 2-9 shows a typical EDS spectrum obtained from a full-body scan of a reacted nanomotor. Using this, the calculated % elemental

composition of the rod across the length of the silver segment shows a Ag:I ratio of about 6:1 in 28.2 mM $I_2$. Since the shell is porous, the diffusion of silver ions through the shell will be somewhat slowed but not stopped. Hence, the formation of AgI shell is unlikely to reduce the nanomotor efficiency significantly.

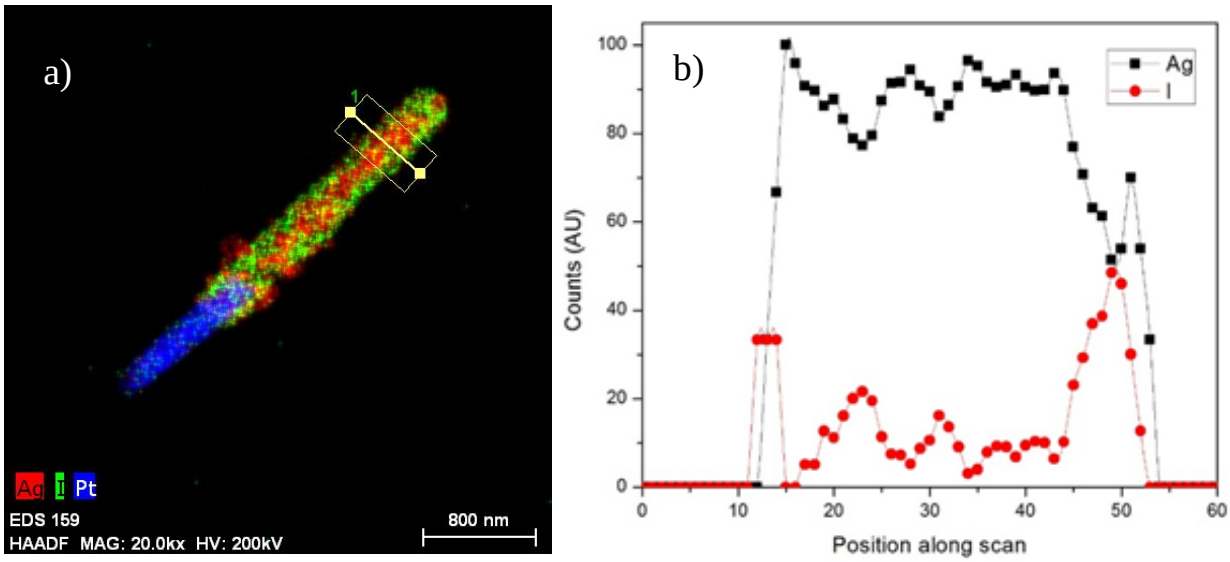


**Figure 2-8**. Elemental mapping scan data of AgI-Pt nanorod using Titan EDS. (a) EDS compiled image of elements, showing the path of the scan across the silver segment. (b) Graph generated from the counts detected for the elements silver and iodine along the bisecting scan. The scan shows higher iodine content at the edge of the motors.

The movement of Ag-Pt nanorods upon the introduction of iodine, as well as SEM and EDS data, demonstrates that the Ag to AgI conversion process proceed as expected. As the conversion should be a surface reaction, the silver iodide formed is amorphous. Figure 2-10 demonstrates this through a series of HRTEM images of an AgI region on the rod being exposed to the electron beam, turning from a relatively amorphous material into a crystalline lattice over time.

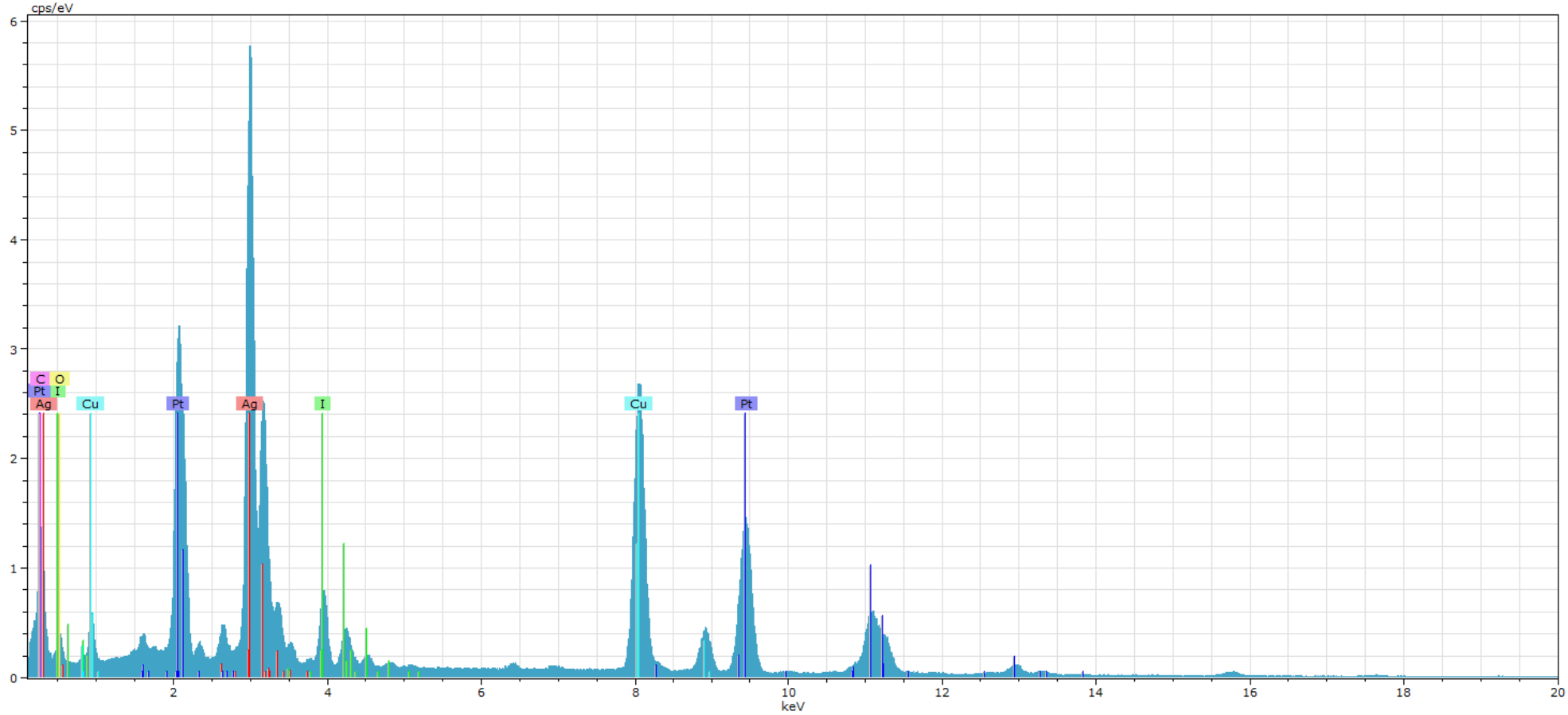


**Figure 2-9**. Typical spectrum obtained from elemental mapping data of AgI-Pt nanorod using Titan EDS. EDS data was taken at 80 kV on a Titan TEM.

**Figure 2-10**. HRTEM (with FFT) images of edge of AgI converted nanomotors taken in sequence (a-d) at 200 kV at the same location and focus over 5 sec, showing initial material being relatively amorphous and subsequent formation of crystalline material over time.

| **HRTEM Image** | **FFT** |
|---|---|
| 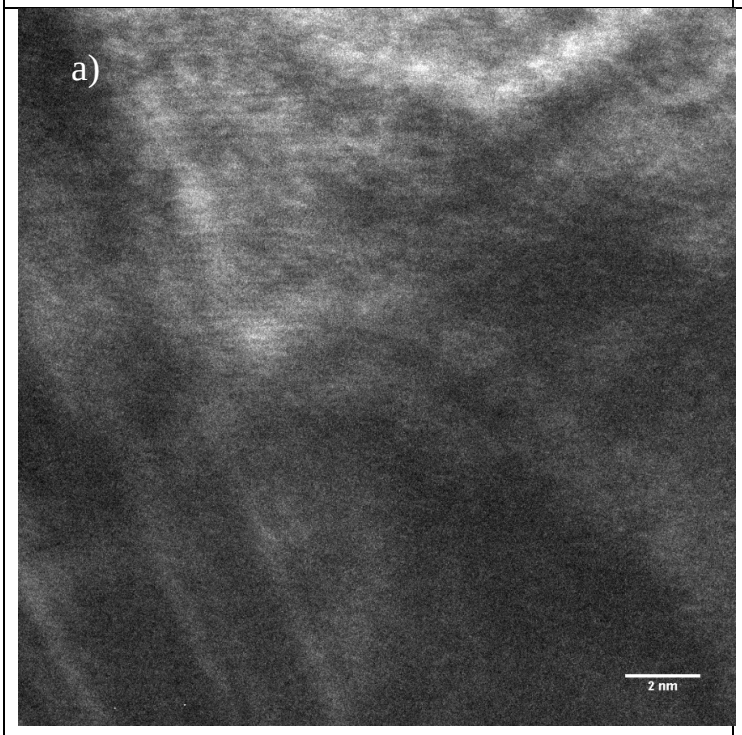  | 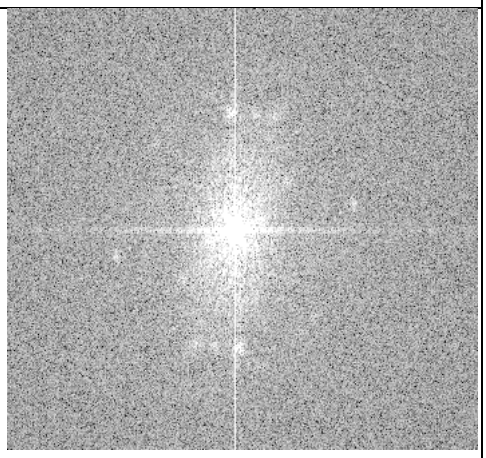 |
| 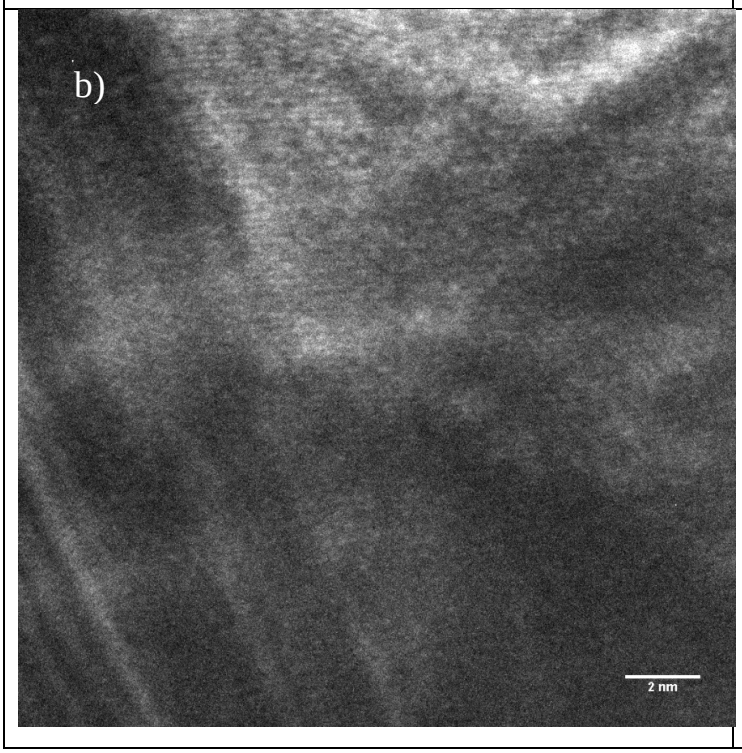  | 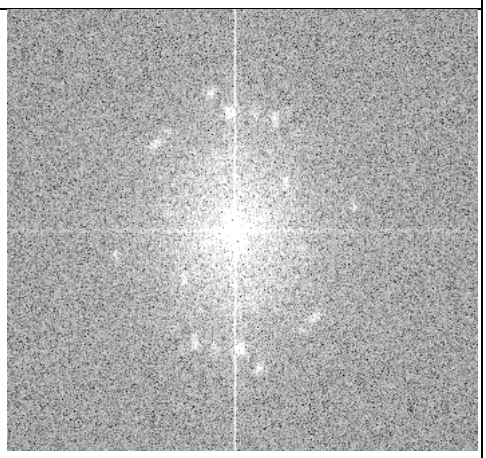 |

**Figure 2-10 continued**. HRTEM (with FFT) images of edge of AgI converted nanomotors taken in sequence (a-d) at 200 kV at the same location and focus over 5 sec.

| **HRTEM Image** | **FFT** |
| --- | --- |
| 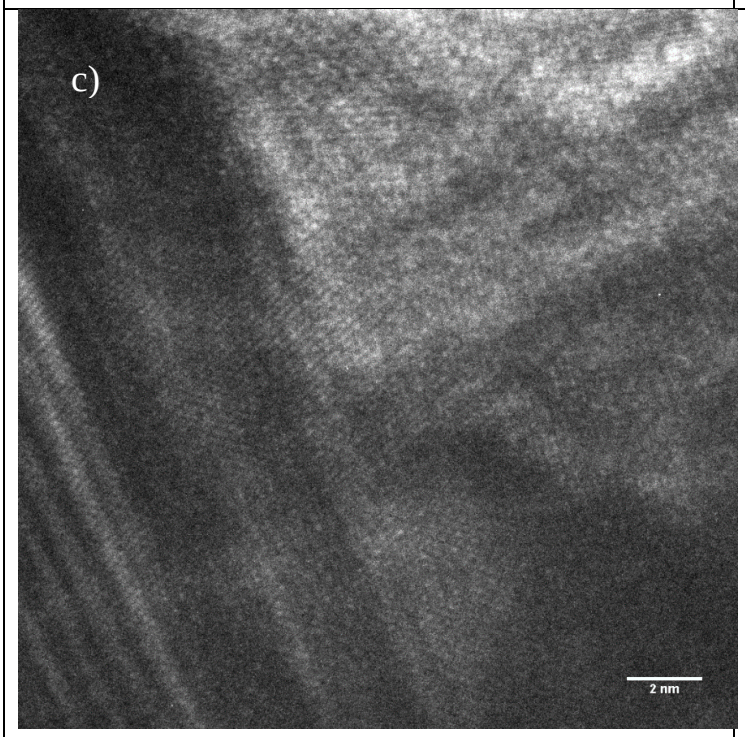  | 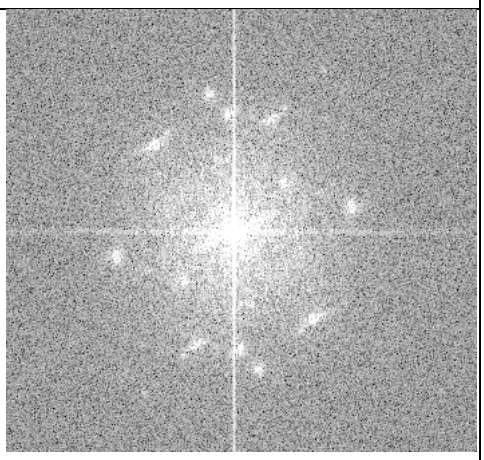 |
| 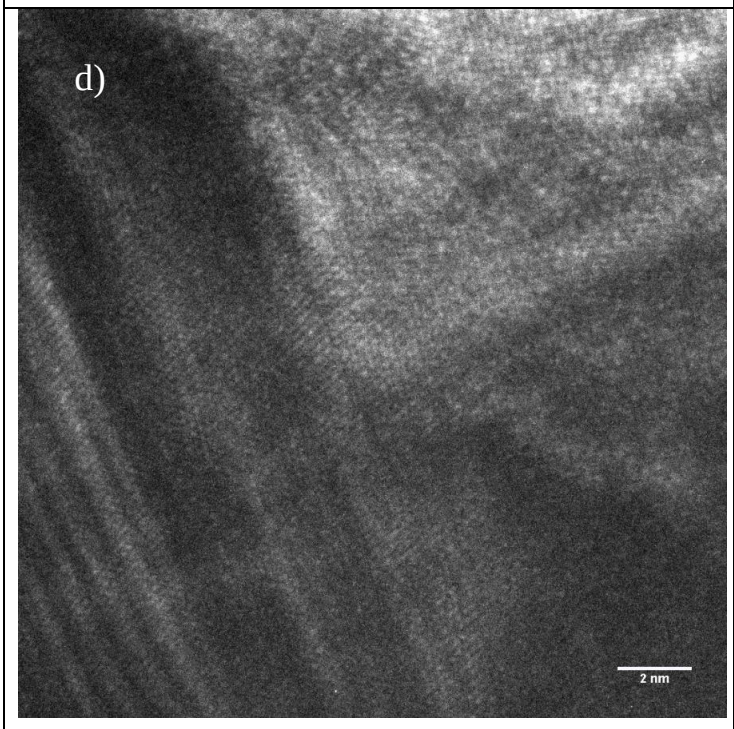  | 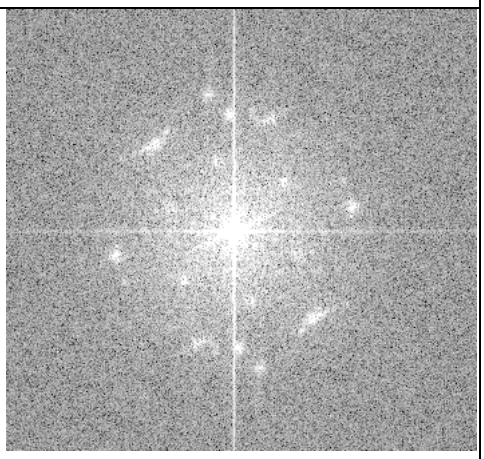 |

### 2.3.3 Mechanism

Figure 2-11 shows the Ag/AgI conversion process and how it powers the motion of the rods. Conversion of the Ag segment of a bimetallic nanorod to AgI occurs from exposure to an aqueous iodine ($I_2$) solution. Oxidation occurs at the silver segment, where electrons lost travel along the length of the rod to the platinum and reduces iodine into iodide ($I^-$) ions. $I^-$ ions subsequently flow along the length of the rod and combines with the oxidized silver ($Ag^+$) to form AgI. Positive ions in the double layer on the surface of the negatively-charged nanorod causes electroosmotic fluid flow along the rod in the direction of the electric field (Ag to Pt), thereby causing the nanomotor to move silver side first.

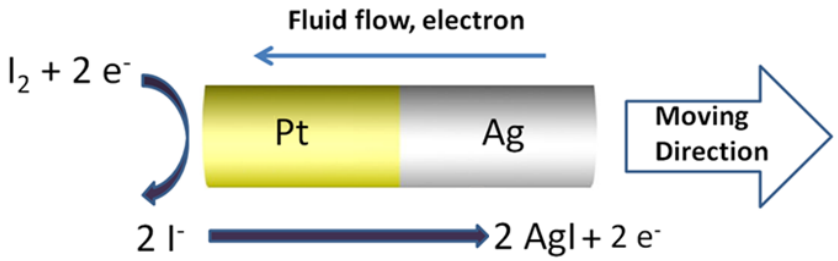


**Figure 2-11**. Detailed diagram of the conversion cycle and how the motion of the silver-based nanorod occurs.

To confirm the directional movement of the nanorods and whether the silver segment is indeed the leading end, a reflectance mode recording of Ag-Au nanorods in iodine were analyzed. Ag-Au nanorods were used to better visualize the two different segments due to the inherent color difference in the metals that is observable in the optical microscope. Figure 2-12 is a time-tracked image of said Ag-Au nanomotors, which clearly move along their long axis with the silver end leading. This supports the electrophoretic mechanism of Ag-based nanomotors.

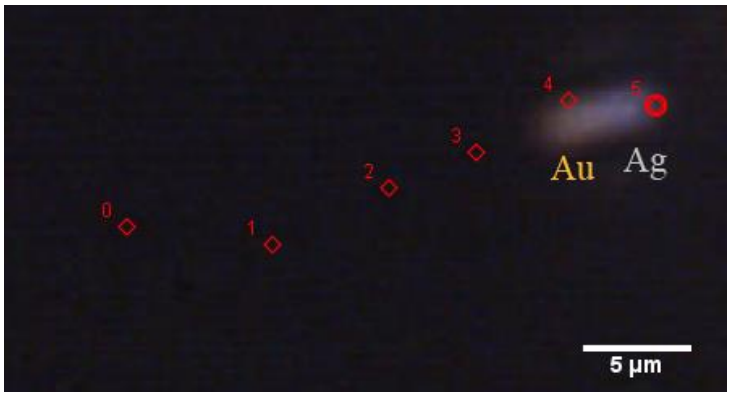


**Figure 2-12**. Time-tracked image of Au-Ag nanorod moving in iodine (42.3 µM), recorded in reflectance mode.

Another major evidence for a self-electrophoretic mechanism is the absence of motion with a non-conductive polymer tail in place of conductive platinum or gold. Nanorods composed of a poly(3,4-ethylenedioxythiophene) segment in contact with silver does not show motion when exposed to iodine fuel.

To further confirm the reaction mechanism, electrochemical potentials and the open circuit current was measured using bulk silver and platinum electrodes. The redox reactions that occur with Ag and Pt in an $I_2$ solution are as follow: Silver is oxidized to silver ion (eq. 1). In an iodine solution, there are two possible reduction reactions (eq. 2 and 3):

$$Ag + I^- \rightarrow AgI + e^- \qquad E^0 = 0.152\ V \quad (1)$$

$$HIO + H^+ + 2e^- \rightarrow I^- + H_2O \qquad E^0 = 0.987\ V \quad (2)$$

$$I_2 + 2e^- \rightarrow 2I^- \qquad E^0 = 0.535\ V \quad (3)$$

Open-circuit potential between Ag and Pt in a saturated $I_2$ solution were measured to be 0.66 V, suggesting that $I_2$ rather than HIO was being reduced, which further supports the supposed mechanism.

### 2.3.4 Nanomotor Efficiency

In comparison to analogous systems, Ag-Pt motors in $I_2$ move at comparable speeds at orders of magnitude lower fuel consumption. Table 2-2 shows a comparison of nanomotors and their fuel concentrations when running at about 7 μm/s in ambient lighting conditions. Ag-Pt motors use ten times less fuel to achieve the same speeds in comparison to Cu-Pt motors, which provide a direct comparison due to their similar mechanisms. The Ag-Pt nanomotor moves at about 7 μm/s using 28 μM $I_2$, whereas the closest analogous, the Cu-Pt/halide system developed by Liu and Sen,[17] will have an estimated speed of <1 μm/s under the same conditions. In comparison to peroxide systems, Ag-Pt nanomotors use much less fuel due to the absence of side reactions, such platinum-catalyzed spontaneous decomposition of peroxide.

**Table 2-2**. List of nanomotor systems and their fuel concentration required for motion on the order of about 7 μm/s.[17,27]

| Nanomotor System | Fuel | [Fuel] (mM) | Motor speeds (μm/s) |
|---|---|---|---|
| Au-Pt | $H_2O_2$ | 180 | 7-10 |
| Cu-Pt | $Br_2$ /$I_2$ | 0.3 | 7 |
| Ag-Pt | $I_2$ | 0.028 | 7 |

To truly understand the efficiency of the Ag-Pt/$I_2$ motor system, the power conversion efficiency of the nanomotor was calculated based on the equation 4:

$$\eta_{ambient} = \frac{mechanical\ power\ output}{total\ chemical\ power\ input} = \frac{P_{mech}}{P_{chem}} \qquad (4)$$

where $P_{mech}$ and $P_{chem}$ are further defined as

$$P_{mech} = F_{drag} v = f v^2 \qquad (5)$$

$$P_{chem} = n_{I_2}\Delta G \quad (6)$$

Here, $F_{drag}$ is the drag force calculated for a cylindrical motor, where $f$ is defined as

$$f = \frac{2\pi\mu L}{ln\left(\frac{2L}{R}\right)-0.72} \quad (7)$$

The terms for equation 4-7 are defined as $v$ being motor speed, $n_{I_2}$being the rate of fuel consumption, $\Delta G$ is the Gibbs free energy of the Ag to AgI conversion (from equation 1), μ being the dynamic viscosity of water, r being the radius of the cylindrical motor, and L being the length of the cylindrical motor. All units and calculations are provided in Supporting Information.

Using the equations listed above, the calculated efficiency of Ag-Pt nanomotors was on the order of $10^{-5}$. In comparison, Au-Pt/$H_2O_2$ motor efficiency is on the order of $10^{-9}$.[27] An efficiency on the order of $10^{-5}$ makes the Ag-Pt/$I_2$ system comparable to external field driven motors (such as acoustic motors) and more efficient than any other published self-electrophoretic motor.[28,29]

In order to simplify calculations, $n_{I_2}$was calculated based on the instantaneous consumption of all iodine added to the motor system due to Ag to AgI conversion; assuming the process takes place over 10 seconds, which is the typical tracking period, the efficiency calculated becomes $5.4 \times 10^{-4}$. (Full calculation and values used in estimations in Appendix)

Three factors likely contribute to the high efficiency of the Ag-Pt/$I_2$ motors. First, silver reacts rapidly with iodine. Second, there are no side reactions that lead to unproductive fuel consumption. For example, in the Au-Pt/$H_2O_2$ motors, only a small fraction of $H_2O_2$ is utilized for propulsion while the rest is wasted due to its rapid catalytic decomposition at the Pt-end alone. Finally, the converted species, AgI, is a light sensitive material and this property can be used to further enhance motor speeds without the need for additional iodine.

## 2.4 Light-harvesting effect of silver-based nanomotors

### 2.4.1 Regeneration of silver via light exposure

While we have established that Ag-Pt/$I_2$ nanomotor is much more fuel efficient than other electrophoretic motors, the motor depends on a reaction that oxidizes the silver segment to power its motion. When the silver segment is fully converted to AgI or when $I_2$ is exhausted, motion will cease. However, due to silver iodide's high sensitivity to actinic light, we examined the effect of light to either prolong motor motion and/or to enhance motor speeds. Figure 2-13 illustrates how a regenerative cycle for Ag/AgI can be made.

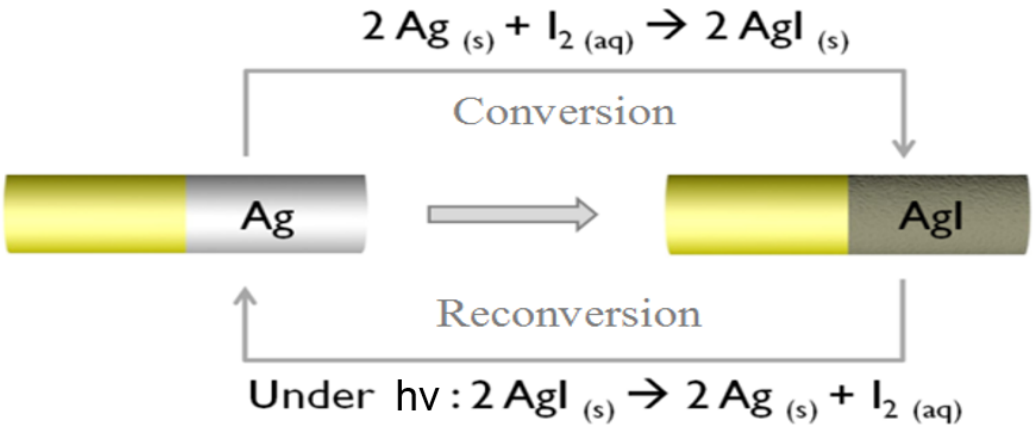


**Figure 2-13**. Ag/AgI conversion and reconversion cycle that can be used to increase nanomotor speed and/or lifetime. An increase in ambient light or UV light exposure leads to significant increase in motor speed.

### 2.4.2 Phenomena

Using this as a basis, one can theoretically develop a silver-based nanomotor with continuous motion in presence of iodine and light. This is, unfortunately, difficult to realize due to the Ag to AgI oxidation rate being much higher than the reconversion (AgI to Ag) rate. Also, at high iodine concentrations, the almost fully converted AgI segment disintegrates when exposed to UV light. We can, however, use UV or-ambient lighting to enhance motor speeds and make longer-lasting motors. Figure 2-14 shows two different speed profiles of Ag-Pt nanomotors at different light exposures. Nanomotor speeds at low fuel concentration do not seem to be affected by increase in ambient light. However, at higher iodine concentrations, an increase in ambient lighting leads to a large increase in motor speeds. At 113 µM $I_2$, a doubling of the motor speed was observed, increasing to 40 ± 6.24 µm/s from 20 ± 5.44 µm/s. Figure 2-15 gives the intensities of light at different wavelengths for 20 mW and 80 mW exposure.

To further understand the reason why light has an effect on the speed of nanomotors, an experiment at low iodine concentration in near-absence of actinic light was performed. The experiment was conducted using a red long-pass filter (Figure 2-16) at 20 mW light exposure, which removes most of the wavelengths to which AgI is photosensitive.

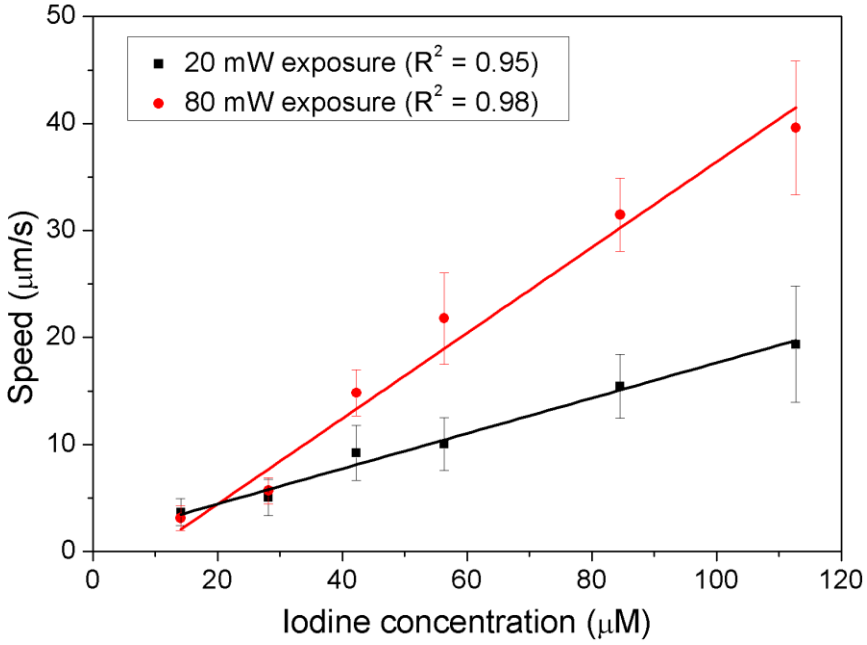


**Figure 2-14**. Speed of Ag-Pt nanomotors at different iodine concentrations at two different light exposures.

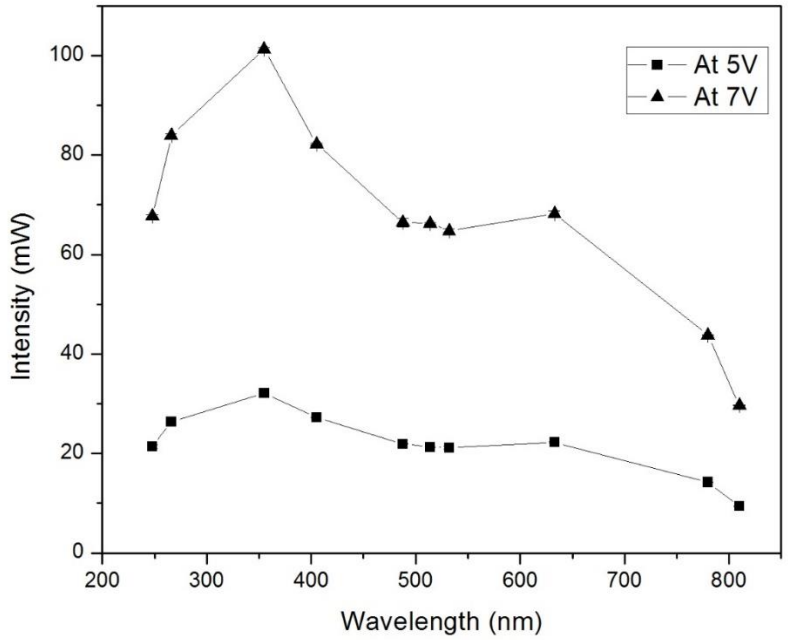


**Figure 2-15**. Lamp intensity readings at 5V (reported as 20 mW intensity) and 7V (reported as 80 mW intensity) microscope settings, recorded using Keithley Model 6487 Picoammeter/Voltage Source.

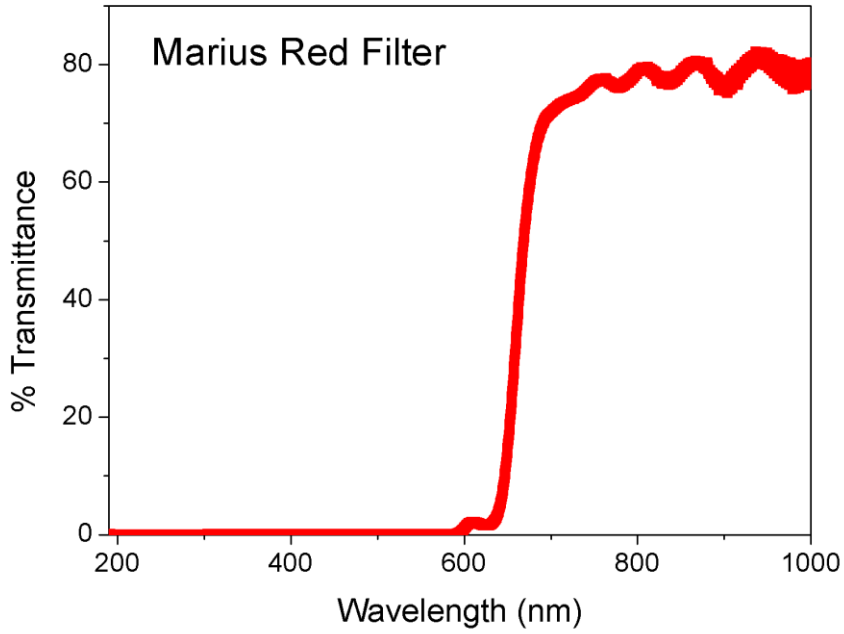


**Figure 2-16.** Transmittance spectrum of commercial red longpass filter (purchased from LEE filters, Marius Red), taken on a Thermo Fisher Evolution 220 UV-Visible Spectrophotometer.

The nanomotors moving in red light have slower speeds (at 5.68 ± 0.9 μm/s) in comparison to motors moving at room-lighting conditions (9.21 ± 2.5 μm/s) in identical iodine exposures (at 42 μM). After motion ceases, the removal of the red filter and an increase in ambient light intensity revitalizes motor movement *without additional iodine exposure*, giving motor speeds of 8.9 ± 2.5 μm/s. This speed is comparable to motors that were moving in ambient lighting conditions after initial exposure to iodine. This suggests that light reinitiates motion due to the decomposition of AgI back into elemental silver and $I_2$.

While light exposure can increase Ag-Pt motor speed and motor longevity, it is only useful when limited to the lower iodine concentrations reported in this paper. An increase in light intensity at higher iodine concentration can lead to very rapid AgI decomposition, causing the nanomotors to visibly curl and deform (Figure 2-17). This deformation is due to uneven formation of elemental

silver that does not uniformly redeposit on the motor surface. In addition, high iodide concentrations increase the solubility of silver iodide through formation of $I_3^-$ ion, thereby aiding in the dissolution of the AgI segment.

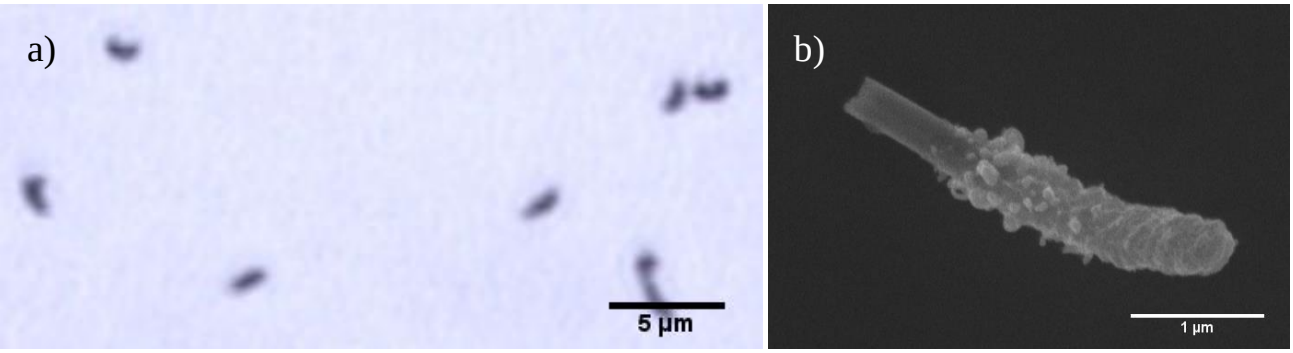


**Figure 2-17**. Optical microscope image (a) showing the curling of Ag-Pt nanomotors when exposed to high UV intensity in presence of 112 µM iodine during iodine exposure and reaction in solution. SEM image (b) shows detailed image of curled Ag-Pt nanomotors post-iodine exposure.

## 2.5 Collective behavior in Silver-based nanomotors

### 2.5.1 Introduction

In nature, collective behavior is prevalent in flocks of birds or schools of fish. The dynamics that influence and leads to collective behavior is often extremely complex and unlike those present in enhanced diffusion systems.[33,34] Using artificial systems, many researchers have been able to mimic this behavior using colloidal particles.[35-37] Such systems can produce self-generated gradients and trigger interactions between the individual particles, often via diffusiophoresis. For both ionic and non-ionic diffusiophoresis,[37,38] colloidal systems must produce non-uniform gradient of solutes and the solute-particle interaction should generate sufficient hydrodynamic stress within the interfacial layer of the particles. The interplay of the forces involved is illustrated by many colloidal systems, such as silver chloride, silver phosphate, and titania microparticles.[22,39-42] These materials are easily fabricated, with the most commonly used method being bottom-up nanoparticle syntheses and precipitation reactions to form uniform particles. [43-45]

Colloidal materials that respond to chemical stimuli,[46,47] photochemical stimuli, [42,48] or both[41] can be used effectively as active systems capable of directional motility and triggered schooling/excluding behavior.[49] Such behaviors often appear with increased colloid concentrations.[40,46-51] These active colloids respond to stimuli and trigger reactions that can produce solutes such as molecules and ions. Doing so, nearby colloids detect the released solutes. The individual colloids can then interact and induce some form of collective behavior as a result. Different types of collective behavior have been demonstrated in literature, ranging from fireworks effect to swarming/schooling, to dynamic clustering effects.

One of the model diffusiophoretic systems is micrometer-sized silver chloride particles that respond to UV illumination, resulting in reduction of silver chloride to metallic silver and subsequent release of $H^+$ and $Cl^-$ ions. Such secretion of ions from the translating micro/nanomotors initiate long-range, collective interactions among the particles via self-diffusiophoresis. This behavior is reminiscent of quorum sensing organisms that swarm in response to a minimum threshold concentration of a signaling chemical. The addition of hydrogen peroxide as an oxidant results in reformation of AgCl and reversal of the above behavior, ultimately resulting in collective oscillations.[39] Further studies uncovered different diffusive behaviors based on their proximity to other particles.[22,41,49]

Titania microparticles have been demonstrated to be another efficient system displaying emergent behaviors of micromotors in response to UV illumination. The photoactivity of $TiO_2$ comes from the electron-hole separation which, in water or methanol, induce complex radical chain reactions that results in diffusiophoretic motion. Hong and collaborators developed $TiO_2$ micromotors and pumps and investigated collective oscillatory behavior of motors with inactive $SiO_2$ particles under periodic UV illumination.[42]

In addition to silver chloride and titanium dioxide, both of which converts energy from photocatalytic reactions into mechanical energy, silver phosphate ($Ag_3PO_4$) microparticles exhibit collective behavior that is not fully dependent on UV light.[41] With $Ag_3PO_4$ particles, the addition and removal of $NH_3$ creates a shift in chemical equilibrium that leads to exclusion and schooling behaviors respectively. The addition of ammonia produces hydroxide ions ($OH^-$), phosphate ions ($HPO_4^{2-}$), and diammino-silver(I) ions ($Ag(NH_3)_2^+$). The diffusivity of $OH^-$ is higher than the other ions in solution, leading to a dominating outward electroosmotic flow that results in exclusion

behavior. Upon depletion of ammonia, the reaction is reversed, resulting in schooling behavior. UV light was only found to be effective in preventing the transition from exclusion to schooling.[41]

While numerous types of synthetic micro- and nanomotors have been reported, there are few examples that show collective behavior. In this section, Ag-Pt nanomotors have been adapted to exhibit such behaviors. The Ag-Pt motors respond to both chemical and photochemical stimuli and, depending on UV exposure, can toggle between schooling and excluding behavior.

### 2.5.2 Fabrication and Experimental details

Ag-Pt nanomotors that exhibit collective behavior was fabricated in an identical fashion as the procedure described in Section 2.2.1. Following deposition, the sacrificial copper was etched with two different commercial etchant solutions: Transene Copper BTP Etch (containing copper chloride, ammonium hydroxide, and hydrogen peroxide) or Transene Copper Etch 49-1 (containing citric acid, ammonium hydroxide, and hydrogen peroxide). Following copper etching, the template was removed via immersion in 3 M NaOH for a period of 30 minutes. The rods were then centrifuged and washed by deionized water at least 8 times. Sample was finally dispersed in 1 mL of deionized water. Experimental conditions are identical to that described in Section 2.2.2.

### 2.5.3 Characterization of Schools

It was an accidental discovery that lead to the formation of schooling silver-based motors. During copper etching, exposure of the silver-segments of the nanorods to the etchant for extended period of times produced nanomotors that schooled after addition of iodine instead of nanomotors only capable of directed translational motion.

Figure 2-18 and 2-19 illustrates how Ag-Pt nanorods form schools after iodine addition. Schools formed immediately after iodine addition tend to be 10-20 μm in diameter (Figure 2-18, left image). In order to determine whether these were indeed schooling behavior and not a result of aggregation, the sample was allowed to sit for an extended period of time after addition of iodine. If the samples aggregate, which they may due to the high particle density in the solution, the aggregates will not relax over time. However, this was not the case as the schools are shown to relax 1 minute after motion stops (Figure 2-18, right image). Figure 2-19 is a compilation of a magnified sample of the same area taken over time, showing how the motors move and slowly come together to form a swarm.

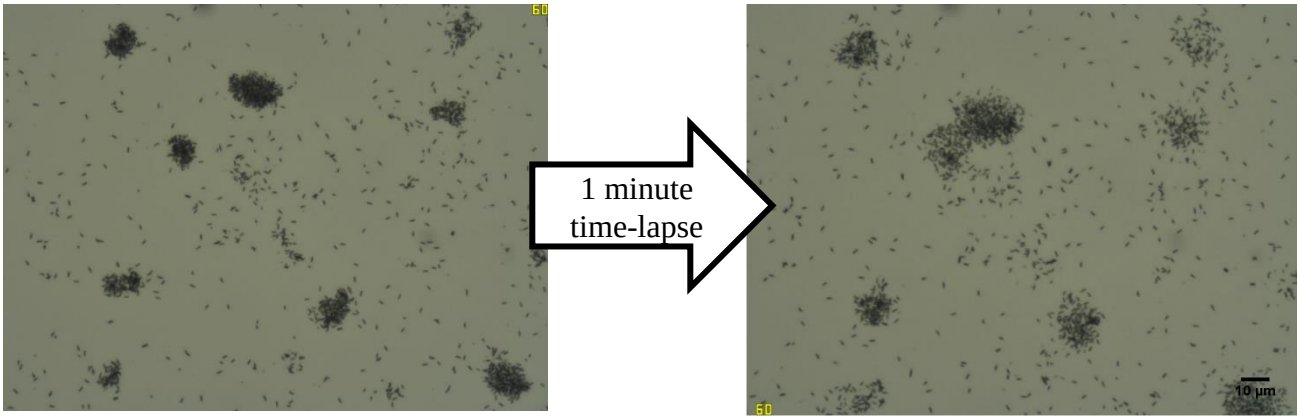


**Figure 2-18.** Tight school formation in Ag-Pt nanorod samples after addition of iodine (left) relaxes over time (right), confirming the presence of collective behavior and not a result of particle aggregation.

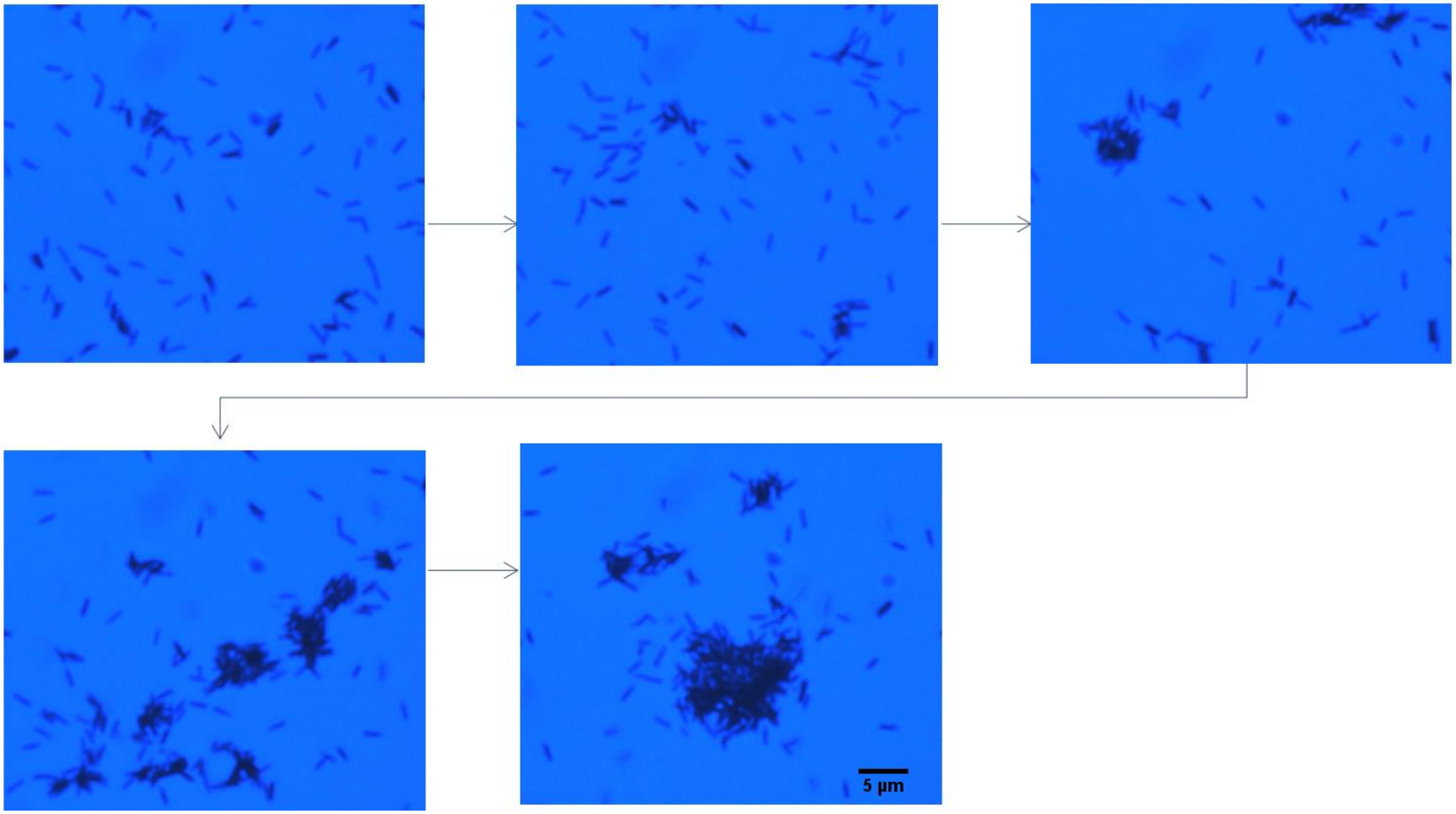


**Figure 2-19.** Formation of schools after iodine addition (7.5%) to Ag-Pt nanorods. Sequential images taken from the same area of a recorded video as time progressed. Over time, smaller individual schools were seen to merge to form larger schools after another addition of iodine fuel after motion has seemingly ceased. The blue tint is the result of the usage of a UV filter inserted before the recording optics.

After schooling/relaxing of motors occur, subsequent additions of iodine reinitiates the schooling phenomena and can even cause individual schools to come together and form larger schools spanning hundreds of microns (Figure 2-20).

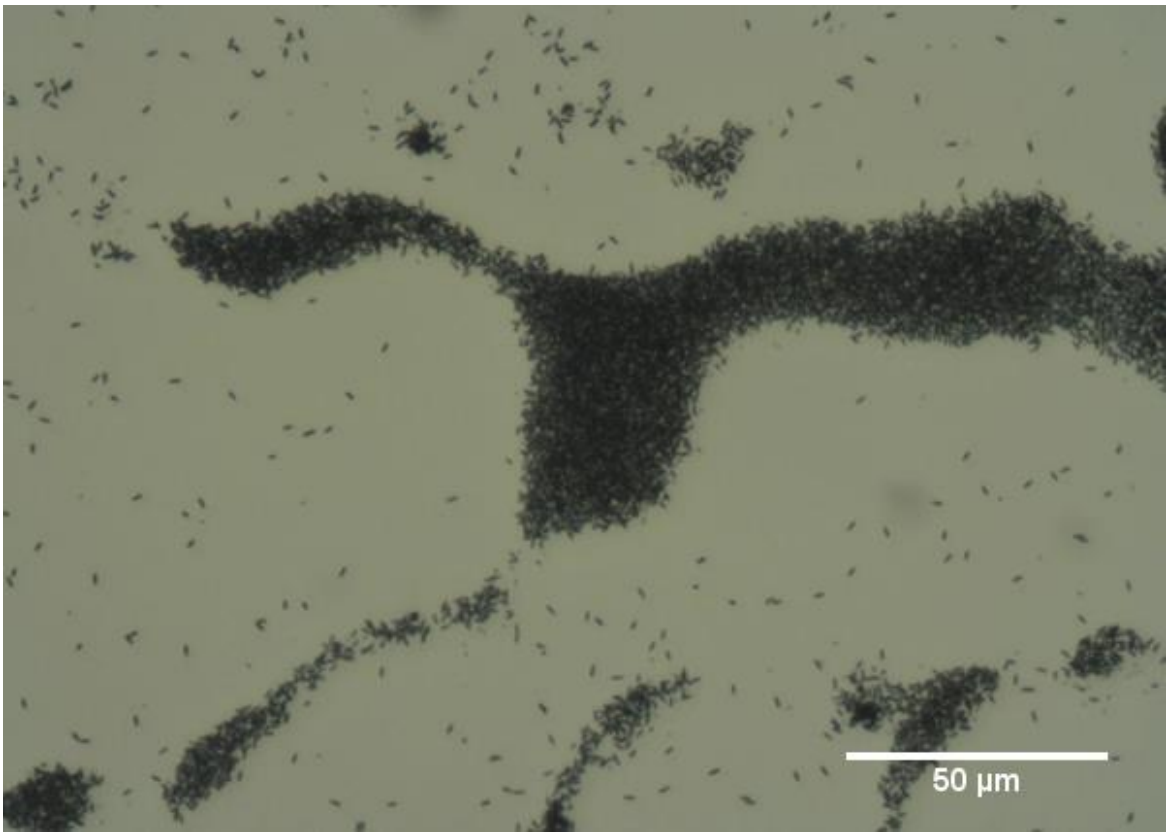


**Figure 2-20.** Formation of large schools through collective behavior of smaller schools after additional iodine exposure.

### 2.5.4 Light-modulated effects on collective behavior

Due to the light sensitivity nature of Ag-Pt nanomotors, it was suspected that Ag-Pt nanorods that exhibit collective behavior can be modulated using light. After formation of schools, introduction of UV light causes a rapid exclusionary effect where the individual motors move away from each other. Subsequent removal of UV light, *without adding additional iodine*, produces a schooling effect that causes the reforming of the original schools. By continually toggling the UV on and off, a "firework-like" effect can be observed with the schooled particles (Figure 2-21).

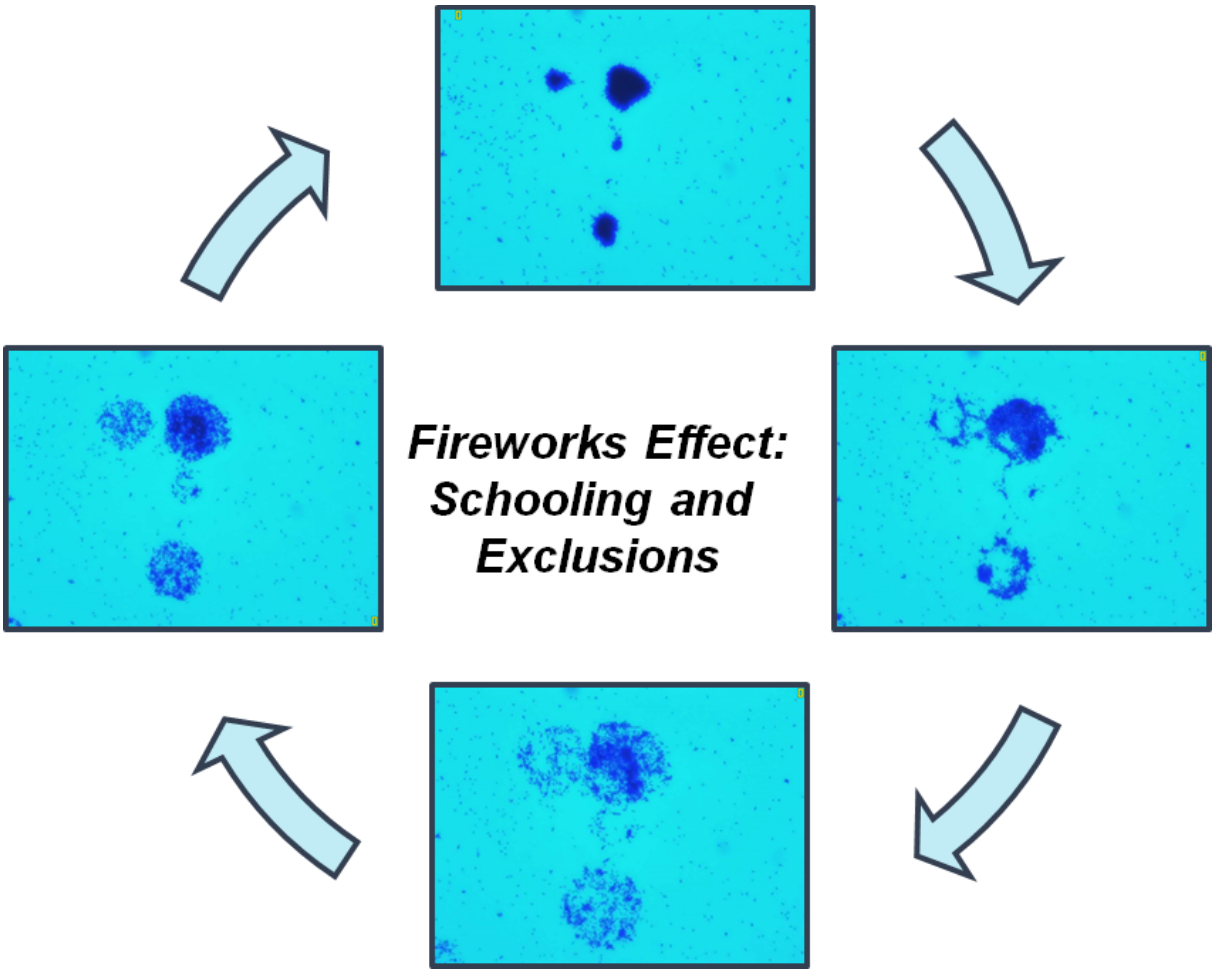


**Figure 2-21.** Fireworks effect resulting from iodine exposure, triggered by UV on/off toggle.

### 2.5.5 Mechanism

This collective behavior was found to only occur when nanorods samples are at full concentration without pre-dilution. In comparison, linear Ag-Pt motors reported in previous sections was pre-diluted to 25% concentration before iodine was added. Therefore, the schooling phenomena may be a due to a high particle density of nanorods. Nanorod samples that experience schooling does not do so when examined in dilute conditions. These dilute nanorod samples, while behaving linearly like the motors described in earlier sections (Chapter 2.1-2-4), do not move at the high speeds observed in the previous sections. This hints at an intrinsic difference in the silver structure of the Ag-Pt nanorods, which was examined via SEM.

It was found that the surface of the silver looked markedly different between nanomotors that move linearly and those that exhibit collective behavior. Figure 2-22 shows a comparison between the two types of motors. Motors that exhibit school have a very rough surface, likely due to uneven oxidation of the silver from exposure to reactive oxidizers (*i.e.* ammonium hydroxide/hydrogen peroxide mix). The motors will, therefore, not respond well via self-electrophoresis due to the impeded electron flow and Ag-to-AgI conversion.

a)

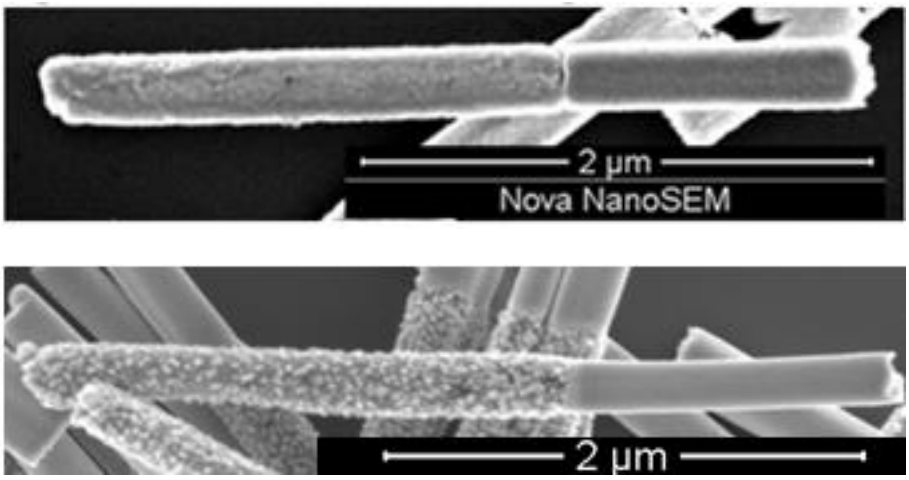


b)

**Figure 2-22.** SEM comparison of Ag-Pt nanomotors that move via directed linear motion (a) and nanomotors that exhibit schooling/excluding behavior (b).

While the exact mechanism has not been elucidated, the schooling effect of Ag-Pt nanomotors may be due to a diffusiophoretic mechanism. With a high density of Ag-Pt nanorods, iodine is consumed rapidly and can lead to localized concentration gradients. With UV exposure, a reverse reaction occurs that may lead to exclusionary behavior.

## 2.6 Conclusion

A highly efficient Ag-Pt nanomotor system that uses micro-molar amounts of fuel have successfully been synthesized. The nanomotors show good linear correlation of motor speed with fuel concentration, current density, and light sensitivity. The propulsion mechanism involves self-electrophoresis with the oxidation of silver and the simultaneous reduction of $I_2$ at the platinum tail, ultimately forming AgI. In the presence of light, AgI decomposes back to Ag and $I_2$. It was found to increases motor speed and reinitiates motion when fuel is spent. In essence, the system serves as light harvesting self-electrophoretic motor. This versatile system can also be turned into a micropump, which will be discussed in detail in Chapter 3.

Moving forward, there are several materials issues that need to be addressed. One such example is the rapid degradation of silver iodide in high light/UV conditions, resulting in curling of the nanomotors. A possible remedy would be a light-permeable membrane or coating that maintains the integrity of the silver segment. In addition, while the schooling phenomena is highly reproducible, the exact mechanism and conditions that induces the motors to behave exhibit collective behavior is not well understood.

Despite the problems outlined above and other issues, the present system serves as an excellent first step towards a light-harvesting active system in its ability to use light to regenerate spent reagents. It does not require high intensity of ultraviolet light required by other light-powered systems and uses the lowest concentration of fuel in comparison to other self-electrophoretic systems. Active motors and pumps that derive their propulsive energy directly from ambient light and uses little or no chemical fuel, and do not require batteries, electronics, or an external power source to function, are likely to find applications in remote regions where they can operate without human intervention.

## 2.7 References


1. Wang, W.; Duan, W.; Ahmed, S.; Mallouk, T.E.; Sen, A. Small Power: Autonomous Nano- and Micro-Motors Propelled by Self-Generated Gradients. *Nano Today*. **2013**, *8*, 531-554.
2. Wang, H.; Pumera, M. Fabrication of Micro/Nanoscale Motors. *Chem. Rev.* **2015**, *155*, 8704-8735.
3. Sanchez, S.; Soler, L.; Katuri, J. Chemically Powered Micro- and Nanomotor. *Angew. Chem. Int. Ed.* **2015**, *54*, 1414-1444.
4. Dey, K.K.; Wong, F.; Altemose, A.; Sen, A. Catalytic Motors – Quo Vadimus? *Curr. Opin. Colloid Interface Sci.* **2016**, *21*, 4-13.
5. Wong, F.; Dey, K.K.; Sen, A. Synthetic Micro/Nanomotors and Pumps: Fabrication and Applications. *Annu. Rev. Mater. Res*. **2016**, 46**,** 407-432.
6. Paxton, W. F.; Kistler, K. C.; Olmeda, C. C.; Sen, A.; St. Angelo, S. K. Cao, Y.; Mallouk, T. E.; Lammert, P. E.; Crespi, V. H. Catalytic Nanomotors: Autonomous Movement of Striped Nanorods. *J. Am. Chem. Soc.*, **2004**, *126*, 13424-13431.
7. Paxton, W. F.; Sen, A.; Mallouk, T. E. Motility of Catalytic Nanoparticles through Self-Generated Force. *Chem. Eur. J.*, **2005**, *11*, 6462-6370.
8. Paxton, W. F.; Baker, P. T.; Kline, T. R.; Wang, Y.; Mallouk, T. E.; Sen, A. Catalytically Induced Electrokinetics for Nanomotors and Nanopumps. *J. Am. Chem. Soc.*, **2006**, *128*, 14881-14888.
9. Kline, T.R.; Paxton, W. F.: Wang, Y.; Velegol, D.; Mallouk, T. E.; Sen, A. Catalytic Micropumps: Microscopic Convective Fluid Flow and Pattern Formation. *J. Am. Chem. Soc.*, **2005**, *127*, 17150-17151.
10. Wang, Y.; Hernandez, R. M.; Bartlett, D. J.; Bingham, J. M.; Kline, T. R.; Sen, A.; Mallouk, T. E. Bipolar Electrochemical Mechanism for the Propulsion of Catalytic Nanomotors in Hydrogen Peroxide Solutions. *Langmuir*, **2006**, *22*, 10451-10456.
11. Moran, J. L.; Wheat, P. M.; Posner, J. D. Locomotion of Electrocatalytic Nanomotors due to Reaction Induced Charge Autoelectrophoresis. *Phys. Rev. E*, **2010**, *81*, 065302(R).
12. Demirok, U. K.; Laocharoensuk, R.; Manesh, K. M.; Wang, J., Ultrafast Catalytic Alloy Nanomotors. *Angew. Chem. Int. Ed.* **2008,** *47*, 9349-9351.
13. Sattayasamitsathit, S.; Gao, W.; Calvo-Marzal, P.; Manesh, K. M.; Wang, J., Simplified Cost-Effective Preparation of High-Performance Ag-Pt Nanowire Motors. *ChemPhysChem* **2010,** *11*, 2802-2805.
14. Laocharoensuk, R.; Burdick, J.; Wang, J., Carbon-Nanotube-Induced Acceleration of Catalytic Nanomotors. *ACS Nano* **2008,** *2*, 1069-1075.
15. Soler, L.; Magdanz, V.; Fomin, V.M.; Sanchez, S.; Schmidt, O.G. Self-propelled micromotors for Cleaning Polluted Water. *ACS Nano*. **2013**, *7*, 9611-9620.
16. Lee, T.C.; Alarcón-Correa, M.; Miksch, C.; Hahn, K.; Gibbs, J.G.; Fischer, P. Self-propelling Nanomotors in the Presence of Strong Brownian Forces. *Nano Lett.* **2014**, *14*, 2407-12.

17. Liu, R.; Sen, A. Autonomous Nanomotor Based on Copper–Platinum Segmented Nanobattery. *J. Am. Chem. Soc.*, **2011**, *133*, 20064-20067.
18. Hong, Y.; Diaz, M.; Córdova-Figueroa, U.M.; Sen, A. Light-Driven Titanium-Dioxide-Based Reversible Microfireworks and Micromotor/Micropump Systems. *Adv. Funct. Mater.* **2010**, *20*, 1568-76.
19. Dong, R.; Zhang, Q.; Gao, W.; Pei, A.; Ren, B. Highly Efficient Light-Driven $TiO_2$-Au Janus Micromotors. *ACS Nano*, **2016**, *10*, 839-844.
20. Li, Y.; Mou, F.; Chen, C.; You, M.; Yin, Y.; Xu, L.; Guan, J. Light-Controlled Bubble Propulsion of Amorphous $TiO_2$/Au Janus Micromotors. *RSC Adv.*, **2016**, *6*, 10697-10703.
21. Ibele, M.; Mallouk, T.E.; Sen, A. Schooling Behavior of Light-Powered Autonomous Micromotors in Water. *Angew. Chem. Int. Ed.* **2009**, *48*, 3308-3312.
22. Ibele, M.E.; Lammert, P.E.; Crespi, V.H.; Sen, A. Emergent, Collective Oscillations of Self-Mobile Particles and Patterned Surfaces Under Redox Conditions. *ACS Nano*. **2010**, *4*, 4845-4851.
23. Duan, W.; Ibele, M.; Liu, R.; Sen, A. Motion Analysis of Light-Powered Autonomous Silver Chloride Nanomotors. *Eur. Phys. J. E.* **2012**, *35*, 77-84.
24. You, M.; Chen, Y.; Zhang, X.; Liu, H.; Wang, R.; Wang, K.; Williams, R. R.; Tan, W. An Autonomous and Controllable Light-Driven DNA Walking Device. *Angew. Chem. Int. Ed*., **2012**, *51*, 2457-2460.
25. Fred, R. R. *Iodide Metals and Metal Iodides*; Wiley: USA, 1961; pp 199-2.
26. Kirk-Othmer Encyclopedia of Chemical Technology. 5th ed. New York, NY. John Wiley and Sons, 1991-Present., p. V22 (1997) 182.
27. Sriveeraraghavan, S.; Krishnan, R.; Natarajan, S. Silver Electrodeposition from Thiosulfate Solutions. *Met. Finish.*, **1989**, *87*, 115-117.
28. Wang, W.; Chiang, T.; Velegol, D.; Mallouk, T.E. Understanding the Efficiency of Autonomous Nano- and Microscale Motors. *J. Am. Chem. Soc.*, **2013**, *135*, 10557-10565.
29. Wang, W.; Castro, L.A.; Hoyos, M,; Mallouk, T.E. Autonomous Motion of Metallic Microrods Propelled by Ultrasound. *ACS Nano*, **2012**, *6*, 6122–6132.
30. Wang, W.; Li, S.; Mair, L.; Ahmed, S.; Huang, T.J.; Mallouk, T.E. Acoustic Propulsion of Nanorod Motors Inside Living Cells. *Angew. Chem. Int. Ed.* **2014**, *53*, 3201-3204.
31. Kline, T. R.; Iwata, J.; Lammert, P. E.; Mallouk, T. E.; Sen, A.; Velegol, D. Catalytically Driven Colloidal Patterning and Transport. *J. Phys. Chem. B.* **2006**, *110*, 24513-24521.
32. Jun, I.; Hess, H. A Biomimetic, Self-pumping Membrane. *Adv. Mater.*, **2010**, *22*, 4823-4825.
33. Anderson, J. L. Colloid transport by interfacial forces. *Annu. Rev Fluid. Mech*. **1986**, *21*, 61-99.
34. Anderson, J. L.; Prieve, D. C. Diffusiophoresis – migration of colloidal particles in gradients of solute concentration. *Sep. Purif. Methods* **1984**, *13*, 67-103.
35. Wang, W.; Duan, W.; Ahmed, S.; Sen, A.; Mallouk, T. E. From one to many: Dynamic assembly and collective behavior of self-propelled colloidal motors. *Acc. Chem. Res.* **2015**, 48, 1938-1946.

36. Solovev, A. A.; Sanchez, S.; Schmidt, O. G. Collective behavior of self-propelled catalytic micromotors. *Nanoscale* **2013**, *5*, 1284-1293.
37. Wang, W.; Duan, W.; Ahmed, S.; Mallouk, T. E.; Sen, A. Small power: Autonomous nano- and micromotors propelled by self-generated gradients. *Nano Today* **2013**, *8*, 531-554.
38. Elgeti, J.; Winkler, R. G.; Gompper, G. Physics of microswimmers – Single particle motion and collective behavior: a review. *Rep. Prog. Phys*. **78**, 056601.
39. Ibele, M.; Mallouk, T. E.; Sen, A. Schooling behavior of light-powered autonomous micromotors in water. *Angew. Chem. Int. Ed.* **2009**, *48*, 3308–12.
40. Wang, W.; Duan, W.; Sen, A.; Mallouk, T. E. Catalytically powered dynamic assembly of rod-shaped nanomotors and passive tracer particles. *Proc. Nat. Acad. Sci.* **2013**, *110*, 17744-17749.
41. Duan, W.; Liu, R.; Sen, A. Transition between collective behaviors of micromotors in response to different stimuli. *J. Am. Chem. Soc.* **2013**, *135*, 1280–83.
42. Hong, Y.; Diaz, M.; Còrdova-Figueroa, U. M.; Sen, A. Light-driven titanium-dioxide-based reversible microfireworks and micromotor/micropump systems. *Adv. Funct. Mater.* **2010**, *20*, 1568–76.
43. Ebbens, S. J. Active colloids: Progress and challenges towards realizing autonomous applications. *Curr. Opin. Colloid Interf. Sci.* **2016**, *21*¸14-23.
44. Dey, K. K.; Wong, F.; Altemose, A.; Sen, A. Catalytic motors – quo vadimus? *Curr. Opin. Coll. Interface Sci.* **2016**, *21*, 4-13.
45. Gibbs, J.; Zhao, Y. Catalytic nanomotors: fabrication, mechanism, and applications. *Frontiers of Mater. Sci.* **2011**, *5*, 25-39.
46. Kagan, D.; Balasubramanian, S.; Wang, J. Chemically Triggered Swarming of Gold Microparticles. *Angew. Chem. Int. Ed.* **2011**, *50*, 503-506.
47. Theurkauff, I.; Cottin-Bizonne, C.; Palacci, J.; Ybert, C.; Bocquet, L. Dynamic Clustering in Active Colloidal Suspensions with Chemical Signaling. *Phys. Rev. Lett.* **2012**, *108*, 268303.
48. Palacci, J.; Sacanna, S.; Steinberg, A. P.; Pine, D. J.; Chaikin, P. M. Living Crystals of Light-Activated Colloidal Surfers. *Science* **2013**, *339*, 936-940.
49. Sen, A.; Ibele, M.; Hong, Y.; Velegol, D. Chemo and phototactic nano/microbots. *Faraday Discuss.* **2009**, *143*, 15–27.
50. Thakur, S.; Kapral, R. Collective dynamics of self-propelled sphere-dimer motors. *Phys. Rev. E* **2012**, *85*, 026121.
51. Soto, R.; Golestanian, R. Self-Assembly of Catalytically Active Colloidal Molecules: Tailoring Activity Through Surface Chemistry. *Phys. Rev. Lett.* **2014**, *112*, 068301.
52. Duan,W,.;Ibele, M.; Liu, R.; Sen, A. Motion analysis of light-powered autonomous silver chloride nanomotors. *Eur. Phys. J. E* **2012**, *35*, 77–84.

# Chapter 3 Light-modulated silver-based micropump using micromolar halogen media

## 3.1 Introduction

Micropumps are of interest to the scientific community due to how it can transfer mechanical energy to its surroundings. One potential application for micropumps is in the field of chemical and biological analysis. Miniaturization of fluidic devices have been in development for over two decades due to the benefits it can offer.[1] Through miniaturization, quantities of samples and reagents can be reduced and, often, the length of time required for detection can be shortened. The smaller size also reduces cost and enables higher portability.[2] These systems, however, often depend on the passive diffusion of material due to the inability to produce fluid movement. For those that involve fluid flows, external fields or pressure is often required (*e.g.* electric fields,[3-5] magnetic fields,[6-9] rotary gears,[10-12] reciprocal displacement[13-16]).

With the discovery and subsequent development of nanomotor systems, it was found that such systems can be adapted into micropumps. These micropumps have the advantage of being self-contained, without the need for a sustained external field or pressure. When the motors are anchored to a surface, it results in the surrounding fluid to flow around the stationary motor which is now acting as a pump. These micropumps produce directional fluid flow, often through chemical means. Such synthetic micropumps respond to external stimuli and, at the surface of the micropump, reactions can lead to the generation of concentration gradients and thus generate fluid flow. The first micropumps[17-20] made from this approach was based on the nanomotors that operated through electrochemical means. By fabricating the two metals in electrical contact on a flat surface, an asymmetric redox reaction occurs at the two metal surfaces and results in a gradient that blankets the two metals. This gradient of ions produces an electric field, which will cause

charge particles in its surround to respond phoretically. The electric double layer at the charged surface of the micropump behaves osmotically. The combination of phoresis and osmosis results in fluid flow in the pump's surface. Subsequent studies produced micropumps systems that utilize other forms of propulsion, such as self-diffusiophoresis,[21-23] density gradients,[24-25] amongst others.[26,27]

Over the course of the last decade, many such systems were developed to delve into applications and to understand the phenomena at small length scales. For example, recent endeavors on alternate micropumps have revolved around polymer-based and enzyme-based systems due to their ability to sense and pump in response to specific analytes. Polymer-based micropumps can produce fluid flows from the depolymerization of an insoluble film when in contact with specific reagents. The resulting products become soluble and, depending on the compound released, will trigger pumping due to diffusiophoresis or density gradients.[25] Enzyme-based systems involves the immobilization of enzymes onto a surface. The selectivity and reactivity of enzymes allows us to induce fluid flows via density gradients due to substrate turnover. This has been accomplished with a variety of enzymes and have further been linked with drug delivery systems and sensor applications.

These micropumps can offer analyte selectivity, directional fluid flow, potential delivery applications, and other advantages that traditional micropumps may fall short from. There is, however, still room for development and improvement. The detection limits for micropumps is similar to that of motor systems, on the order of millimolar concentration. In this chapter, a micropump based on the short-circuiting of silver and platinum metals that operates in the micromolar regime is discussed. The pump was made by evaporating platinum, followed by a patch of silver on top. This provides a continuous interface between the two metals during the

reaction and a distinctive edge that allows for ease in observation. The silver-based micropump uses the motor system described in Chapter 2 as a basis, and therefore, has a light-modulated aspect that can further enhance the movement of fluid and charged particles. This low fuel consumption and light-harvesting effect allows for an excellent study into the fundamentals and principles for light-sensitive micropump systems.

## 3.2 Experimental details

### 3.2.1 Fabrication

A 10 nm adhesion layer of titanium was evaporated via E-beam onto microscope glass slides using a Semicore E-beam Evaporation System. Immediately following evaporation of titanium, a 100 nm of platinum was evaporated to ensure adherence to the titanium without contamination. The sample was allowed to cool in the chamber for 30 minutes before it was removed and a mask with 7 mm circular holes were placed on the platinum sample surface. 200 nm of silver was then evaporated onto the platinum, creating a patch of silver on a film of platinum. This is the interface used for analysis of silver-based micropumps. The samples were cooled in the processing chamber prior to removal. Immediately after removal, the slides were placed in slide holders and stored in a vacuum dessicator until use.

### 3.2.2 Experimental setup

A hybridization chamber (20 mm diameter, 1 mm deep, Grace Bio Labs SKU621111) was attached to the micropump surface to provide a chamber for fluid and tracer particles in order to visualize fluid flow during pumping. Figure 3-1 illustrates typical Ag-Pt micropump experimental setup.

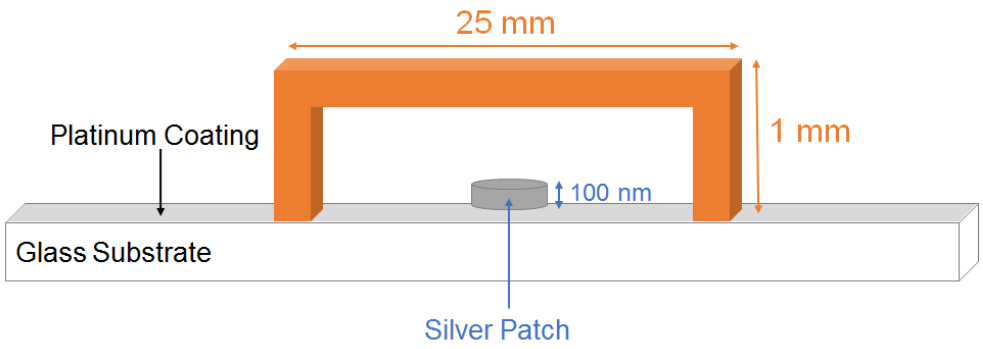


**Figure 3-1.** Silver-platinum micropump schematic, showing position and dimensions of platinum, and silver patches, and the fluid-filled chamber dimensions used in micropump experiments.

In a typical micropump experiment, the hybridization chamber was filled with an iodine solution that contains suspended positively charged tracer particles (amidine polystyrene latex or aPSL) or negatively-charged (sulfate polystyrene latex or sPSL) particles. Iodine concentrations similar to those used in the motor experiments was used for the micropumps to allow for comparison (refer to Table 2-1). For ambient light measurements, the lamp was raised to the high intensity setting. For low lighting measurements, a red cut-off filter (Lee Filters, Marius Red, Figure 2-16) that removes all wavelengths above 650 nm was placed between the top of the micropump chamber and the light from the microscope. The resulting fluid flow was characterized by recording the movement of tracer particles with an Olympus BX60M optical microscope (and in some cases, with a Zeiss Axiovert 200M microscope) with a Point Grey Flea3 camera. The individual particle movement were tracked and analyzed using Tracker video analysis software (by Cabrillo).

## 3.3 Fluid and particle motion in silver-based halogen micropump

### 3.3.1 Analysis of particle/fluid motion

Upon addition of iodine fuel, fluid pumping was immediately initiated. The pumping speeds of positively-charged aPSL and negatively-charged sPSL particles are shown in Figure 3-2. Both show fast pumping speeds at micromolar concentrations of iodine. The average motor speeds of aPSLs are almost halved that of sPSLs at every concentration due to the electroosmotic flow that is responsible for the fluid flow. This difference in speeds is due to the light effect on the electroosmotic flow, which is discussed in a later section.

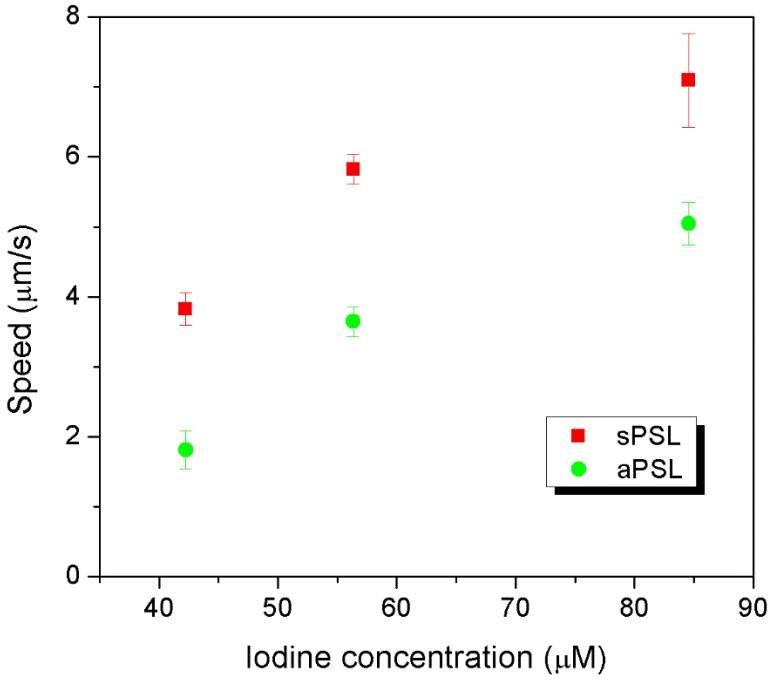


**Figure 3-2.** Pumping speeds for aPSL and sPSL particles in silver-based micropumps at different iodine concentrations.

In comparison to other similar types of micropumps, silver-based micropumps show comparable pumping speeds at lower fuel concentrations. This is mainly a result of the sensitivity of silver to iodine fuel. The resulting conversion of silver to silver iodide occurs rapidly and thus

creates high pumping speeds. This high reactivity also leads to relatively fast consumption of the silver patch at high iodine concentrations. As a result, pump speeds in high iodine concentrations are not as consistent as the speeds reported in figure 3-2.

In addition to the speed differences between aPSL and sPSL tracer particles, they were observed to move in opposite directions. The aPSL particles were pumped outwards from silver towards platinum at the Ag/Pt interface while sPSL particles were pumped inwards, as shown in Figure 3-3 and 3-4 respectively.

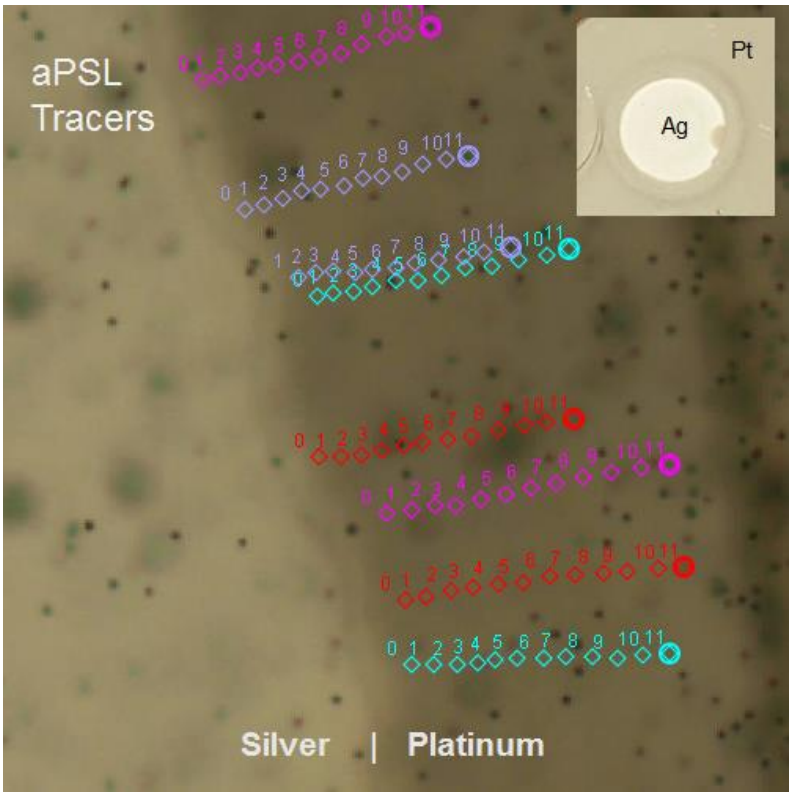


**Figure 3-3.** Tracking of aPSL particles in 85 µmol $I_2$ every second for 11 seconds. aPSL particles are pumped outwards from the Ag/Pt interface**.**

The aPSL particles shown in figure 3-3 were pumped outwards. The inset in the figure is a macroscale image of the pump, exhibiting an accumulation ring as a result of the pumping of the tracers off the silver patch (faint grey line surrounding the Ag patch). This was observed in all micropump samples, but was most apparent at higher concentrations.

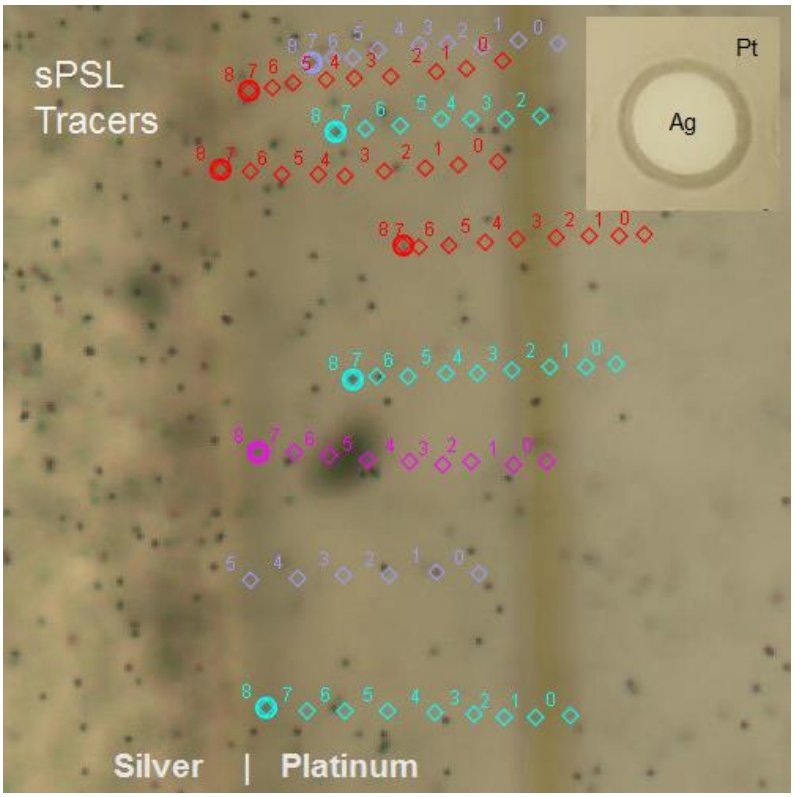


**Figure 3-4.** Tracking of sPSL particles in 85 µmol $I_2$ every second for 8 seconds. sPSL particles are pumped inwards towards the Ag/Pt interface.

The sPSL particles shown in figure 3-4 were pumped inwards. The inset in the figure is a macroscale image of the pump, exhibiting an exclusion zone is the result of the pumping of the surrounding tracers towards the silver and accumulating on top of the silver patch (empty dark ring

surrounding Ag patch). This was observed in all micropump samples, but was also most apparent at higher concentrations.

### 3.3.2 Mechanism

The Ag-Pt micropump operates based on particle electrophoresis and electroosmosis. Figure 3-5 illustrates fluid pumping mechanism for the silver-iodine micropump.

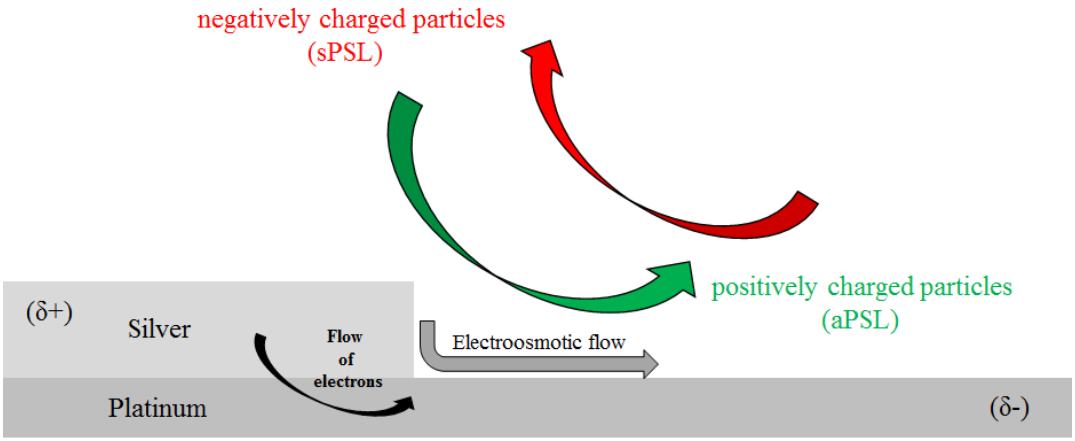


**Figure 3-5.** Mechanism for charged particle motion at silver-platinum interface in iodine solution. During the conversion of Ag to AgI, electrons are formed at the silver segment and consumed at the platinum. The flow of electrons causes the silver patch to develop a δ+ charge and the platinum patch to develop a δ- charge, causing the aPSL particles to migrate towards platinum while sPSL particles to migrate towards silver at the Ag/Pt interface.[9,31]

Evidence of this mechanism can be seen in the pumping directions of the particles. In the upright position, aPSL is pumped outwards while sPSL is pumped inwards. The pumping directions for the charge-specific particles do not change when the pump system was inverted, demonstrating that the pumping mechanism is a result of the electron flow occurring from silver

to platinum during the Ag to AgI reaction (illustrated in Figure 2-11) and not a result of other factors such as thermal or density-driven flows.[24,28]

In addition to particle electrophoresis, there is electroosmotic fluid flow along the pump surface due to the redox reaction. Because of the presence of an oxide layer, metal surfaces have a negative zeta potential.[8] Consequently the double layer is positively charged resulting in fluid flow along the metal surface towards the negative end (Pt segment).[31,32] This electroosmotic flow either aids (for positive aPSL) or retards (for negative sPSL) particle motion, resulting in the pumping speed differences shown in Figure 3-2.

### 3.3.3 Light-modulated effect of micropumps

As with the Ag-Pt nanomotors, Ag-Pt micropumps are also sensitive to ambient light. In Figure 3-2, the speeds of aPSL particles and sPSL particles in ambient light is reported. In the absence of light, however, the speeds of the particles change drastically. Figure 3-6 shows compiled graphs of aPSL and sPSL pump speeds as a function of iodine concentration and light exposure. sPSL particles show higher pump speeds when exposed to light (blue) in comparison to pump speeds where wavelengths above 650 nm were filtered out (red). aPSL particles, however, show the inverse trend. Use of a red filter (red) yields faster pump speeds in comparison to exposure to light (blue).

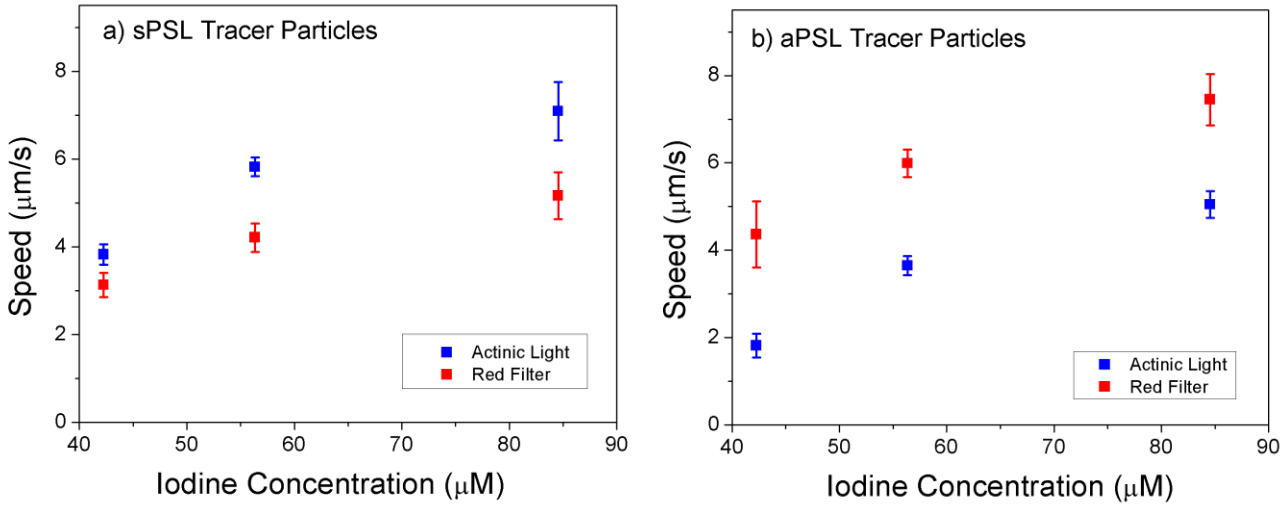


**Figure 3-6.** Pump speeds at different iodine concentrations for (a) sPSL particles and (b) aPSL particles in low light (red) and high light (blue) conditions.

As mentioned in the previous section, the electrophoretic effect and electroosmotic flow generated by the Ag-to-AgI conversion is what causes the positively charged aPSL to be pumped outwards while negatively charged sPSL is pumped inwards. The difference in exposure to light is the main factor for the different trends observed. In the presence of light, the redox reaction is partially reversed, slowing down the electroosmotic flow. In the absence of light, there is no reversal of AgI-to-Ag so the electroosmotic flow is not retarded by the reverse reaction. Accordingly, the pump speed of sPSL particles in high exposure of light is faster in comparison to pump speeds when a red filter was in use (Figure 3-6A). sPSL particles flow in the counter direction to the electroosmotic flow. When in presence of light, the electroosmotic flow is impeded and sPSL particles will move faster because there is a slower flow going in opposition. On the other hand, the pump speed of aPSL particles shows the opposite trend. Thus, the speeds of aPSL particles is increased in the absence of light (Figure 3-6B). In the absence of light, there is no

reverse reaction and the electroosmotic flow is unaffected. aPSL particles move along the direction of the electroosmotic flow and therefore moves faster.

### 3.4 Conclusion

Ag-Pt micropumps have excellent reproducibility and sensitivity to iodine fuel. It uses micromolar amounts of chemical fuel in comparison to the millimolar amounts usually employed in other similar micropump systems. The particle electrophoresis of positively and negatively charged particles can be used to aid in their separation. Ag-Pt micropumps have an added benefit of the ability to be light-modulated. By changing the light intensity, the electroosmotic flow can be sped up or slowed down. This offers an added dimension of control to pumping speeds in addition to fuel concentration.

Moving forward, there are materials issues that need to be addressed. One such example is the rapid degradation of silver iodide in high light and high iodine concentrations, resulting in the formation of Ag debris in the micropumps. In high iodine concentrations, the solubility of silver iodide increase. Therefore, when exposed to light, the process occurs rapidly and the reformed silver and pieces of silver iodide go into the solution. Pumping speeds at lower iodine concentrations, however, is very consistent and do not exhibit this issue.

The present system, in conjunction with the system describe in Chapter 1, serves as an excellent first step towards a light-harvesting active system in its ability to use light to regenerate spent reagents. Silver-based systems is shown to have extreme versatility in the type of setup that it can operate in. This study demonstrates new design principles for micro/nanomotors and pump systems that has light-sensitivity and harvesting properties, with possible uses in applications that can be made as a closed system without user input.

## 3.5 References


1. Laser, D. J.; Santiago, J. G. A review of micropumps. *J. Micromech. Microeng.* **2004**, *14*, R35-R64.
2. Wong, C. C.; Flemming, J. H.; Adkins, D. R. Evaluation of mini/micro-pumps for micro-chem-lab. *Proc. 2002 ASME Int. Mechanical Engineering Congress and Exposition*. **2002**; New Orleans, LA.
3. Bart, S. F.; Tavrow, L. S.; Mehregany, M.; Lang, J. H. Microfabricated electrohydrodynamic pumps. *Sensors Actuators A* **1990**, *21*, 193-197.
4. Fuhr, G.; Schnelle, T.; Wagner, B.Traveling wave-driven microfabricated electrohydrodynamic pumps for liquids. *J. Micromech. Microeng*. **1994**, *4*, 217–26.
5. Jeong, S.; Seyed-Yagoobi, J. Experimental study of electrohydrodynamic pumping through conduction phenomenon. *J. Electrost*. **2002**, *56*, 123–33.
6. Hatch, A.; Kamholz, A. E.; Holman, G.; Yager, P.; Bohringer, K. F. A ferrofluidic magnetic micropump. *J. Microelectromech. Syst*. **2001**, *10*, 215–21.
7. Lemoff, A. V.; Lee, A. P. An AC magnetohydrodynamic micropump. *Sensors Actuators B* **2000**, *63*, 178–85.
8. Huang, L.; Wang, W.; Murphy, M. C.; Lian, K.; Ling, Z. G. LIGA fabrication and test of a DC type magnetohydrodynamic (MHD) micropump. *Microsyst. Technol*. **2000**, *6*, 235–40.
9. Leventis, N.; Gao, X. R. Magnetohydrodynamic electrochemistry in the field of Nd-Fe-B magnets. Theory; experiment; and application in self-powered flow delivery systems. *Anal. Chem.* **2001**, 73, 3981–92.
10. Döppler, J.; Clemens, W.; Ehrfeld, W.; Jung, S.; Kämper, K-P.; Lehr, H. Micro gear pumps for dosing of viscous fluids. *J. Micromech. Microeng.* **1997,** *7*, 230–232.
11. Kilani, M. I.; Galambos, P. C.; Halk, Y. S.; Chem, C-J. A surface micromachined spiral-channel viscous pump. *Proc. 2001 ASME International Mechanical Engineering Congress and Exposition.* **2002**: *New Orleans, LA.*
12. Terray, A.; Oakey, J.; Maar, D. W. M. Microfluidic control using colloidal devices *Science* **2002**, *296*, 1841–1844.
13. van Lintel, H.T.G.; van de Pol, F.C.M.; Bouwstra, S. A piezoelectric micropump based on micromachining of silicon. *Sensors Actuators*, **1988**, *15*, 153-167.
14. Shoji, S.; Nakagawa, S.; Esashi, M. Micropump and sample-injector for integrated chemical analyzing systems. *Sensors Actuators A*, **1990**, *21*, 189-92.
15. Berg, J. M.; Anderson, R.; Anaya, M.; Lahlouh, B.; Holtz, M.; Dallas, T. A two-stage discrete peristaltic micropump. *Sensors Actuators A*, **2002**, *104*, 6-10.
16. Zengerle, R.; Ulrich, J.; Kluge, S.; Richter, M.; Richter, A. A bidirectional silicon micropump. *Sensors Actuators A* **1995**, *50*, 81–6.
17. Kline, T. R.; Iwata, J.; Lammert, P. E.; Mallouk, T. E.; Sen, A.; Velegol, D. Catalytically Driven Colloidal Patterning and Transport. *J. Phys. Chem. B* **2006**, *110*, 24513-21.
18. Ibele, M. E.; Wang, Y.; Kline, T. R.; Mallouk, T. E.; Sen, A. Hydrazine Fuels for Bimetallic Catalytic Microfluidic Pumping. *J. Am. Chem. Soc.* **2007**, *129*, 7762-7763.
19. Kline, T. R.; Paxton, W. F.; Wang, Y.; Velegol, D.; Mallouk, T. E.; Sen, A. Catalytic micropumps: microscopic convective fluid flow and pattern formation. *J. Am. Chem. Soc.* **2005**, *127*, 17150-1.

20. Jun, I.-K.; Hess, H. A Biomimetic, Self-Pumping Membrane. *Adv. Mater.* **2010**, *22*, 4823-4825.
21. McDermott, J. J.; Kar, A.; Daher, M.; Klara, S.; Wang, G.; Sen, A.; Velegol, D. Self-generated diffusioosmotic flows from calcium carbonate micropumps. *Langmuir* **2012**, *28*, 15491–97.
22. Yadav, V.; Zhang, H.; Pavlick, R.; Sen, A. Triggered "on/off " micropumps and colloidal photodiode. *J. Am. Chem. Soc*. **2012**, *134*, 15688–91.
23. Reinmuller, A.; Oguz, E. C.; Messina, R.; Lowen, H.; Schope, H. J.; Palberg, T. Colloidal crystallization in the quasi-two-dimensional induced by electrolyte gradients. *J. Chem. Phys*. **2012**, *136*, 164505–10.
24. Sengupta, S.; Patra, D.; Rivera, I. O.; Agrawal, A.; Dey, K. K.; Cordova-Figueroa, U.; Mallouk, T. E.; Sen, A. Self-powered enzyme micropumps. *Nat. Chem*. **2014**, *6*, 415–22.
25. Zhang, H.; Yeung, K.; Robbins, J. S.; Pavlick, R. A.; Wu, M.; Liu, R.; Sen, A.; Phillips, S. T. Self-powered microscale pumps based on analyte-initiated depolymerization reactions. *Angew. Chem. Int. Ed*. **2012**, *51*, 2400–4.
26. Patra, D.; Zhang, H.; Sengupta, S.; Sen, A. Dual stimuli-responsive, rechargeable micropumps via "host-guest" interactions. *ACS Nano* **2013**, *7*, 7674–79.
27. Solovev, A. A.; Sanchez, S.; Mei. Y.; Schmidt, O. G. Tunable catalytic tubular micro-pumps operating at low concentrations of hydrogen peroxide. *Phys. Chem. Chem. Phys*. **2011**, *13*, 10131–35.
28. Zeng, S.; Chen, C-H.; Mikkelsen Jr,; J. C.; Santiago, J. G. Fabrication and characterization of electroosmotic micropumps. *Sensors and Actuators B* **2001**, *79*, 107-114.

# Chapter 4 Biocompatible acetalated dextran polymer micromotor and pumps

## 4.1 Introduction

Stimuli responsive polymeric materials[1-3] have gathered a lot of interest in engineering and biomedical applications. Research interests have significantly grown in the design of 'smart' polymer platforms which can undergo spontaneous physical (conformation, inter-, intra-strand association) or chemical (fragmentation or degradation) changes in nano-dimensions when external stimuli is present.[4-6] These polymer based therapeutics can release cargo, *e.g.* drug molecules,[7,8] DNA,[9,10] and protein,[11-13] in response to specific physiological stimuli such as pH, and ionic strength.[14-16]

Acid degradable polymers,[17] especially those which respond to mildly acidic media are particularly attractive carriers as they can selectively release the therapeutic material in acidic micro environment of tumors or intracellular endosomes and lysosomes.[18] By design, the acid labile polymers are of two different types: a) acid cleavable functional groups are present in the polymer backbone, leading to depolymerization when the end cap is removed in acidic media; b) acid labile pendant groups release cargo where the polymeric backbone remains intact. In case of the former, biocompatibility of the polymer fragments poses a severe limitation, whereas, in the latter case OH-functionalized biocompatible polysaccarides can be used as the base-polymer. Bachelder and coworkers[19] demonstrated that the acetalation of the OH- groups present in dextran is an efficient technique to obtain pH responsive, biodegradable polymer platforms with tunable rate of degradation. The degradation products thus obtained from this polymer (AcDEX) are water soluble dextran, acetone, and methanol. This polymer is extremely versatile and can be made into

different architectures, such as microspheres or microfibers.[20] AcDEX microspheres were found to have low toxicity in comparison to FDA-approved poly(lactic-co-glycolic acid) (PLGA) microspheres.[19] AcDEX, as a result, has been widely studied as therapeutic agents, such as for usage as vaccines, vaccine-based treatments, and sustained release systems.[8, 19-22] More recently, Kauffman and collaborators[23] have also demonstrated that, by using a different acetal protection group, the acetalated dextran they synthesized produces ethanol instead of methanol, which further enhances the polymers' biocompatibility. Figure 4-1 illustrates the polymer reaction scheme.

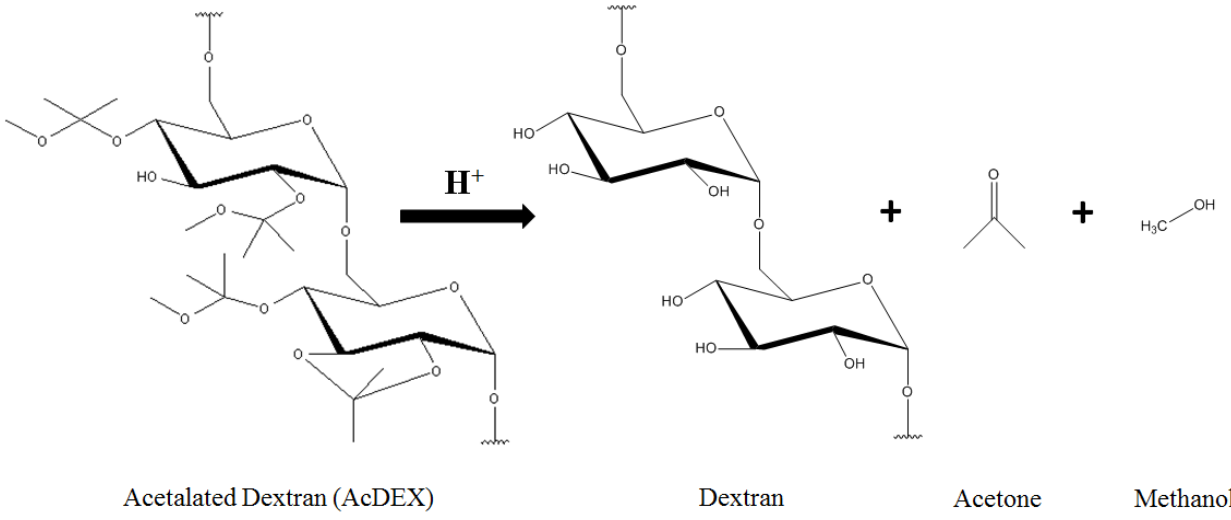


**Figure 4-1**. Reaction scheme for degradation of AcDEX polymer into dextran, acetone, and methanol by-products under acidic conditions.

Stimuli responsive bio-compatible materials, such as AcDEX, is an area of research that is gaining importance due to its potential applications. While much of the work is focused on developing and characterizing such materials, another field of research have adapted these materials to serve another purpose. The development and adaptation of materials for the design of functional micro-dimensional pumps have often focused on using polymers like AcDEX to trigger fluid motion in response to internal stimuli. These pump systems have been designed to respond

to a range of specific analytes, with great potential for use in biological and analytical systems. While many different biopolymers have been explored for this application, AcDEX holds a distinct advantage over the other polymers. The previously reported stimuli responsive polymer micropumps are based on a depolymerization approach.[24,25] Thus the extent of pumping depends on the accessibility of the polymer end caps to the external stimuli.[26] In the current approach the acid labile acetal groups are dangling from the dextran backbone, and unlike the predecessors, these micropumps can undergo facile degradation to initiate pumping of fluid. In this chapter, the first example of self-powered acetalated dextran micropumps which sense acidic pH and initiate the pumping of both fluid and insoluble particles is discussed. The mechanism of pumping and tunability of both rate and direction of pumping is further established. In addition, a proof-of-concept micromotor was developed, illustrating how versatile this material is for self-powered active material fabrication.

## 4.2 Experimental details

### 4.2.1 Synthesis of AcDEX polymer

Anhydrous dextran (3g) of 9-11 KD molecular weight range was dissolved into anhydrous DMSO (30 mL) by stirring at 60 $^{o}$C for 2 hours. After cooling down the reaction mixture to room temperature, pyridinium p-toluene sulfonate (46 mg) was added followed by the addition of 2-methoxy propene (8g, 111 mmol) drop by drop. Resulting reaction mixture was allowed to stir at room temperature and 12 mL of reaction aliquots were withdrawn at 10 minutes, 1 hour, and 6 hour time points, using gas tight syringe. The desired solid product was precipitated by immediately adding the reaction aliquot in water. Finally, solid product was collected by vacuum

filtration and freeze dried to further remove any residual moisture. Solid product was stored in a dessicator at -20°C. The methodology was adapted from the procedure reported in Kaufmann, et al.[23]

### 4.2.2 Fabrication of polymer micropump

Glass slides were cleaned with piranha solution for 1 hour, thoroughly rinsed with distilled water, and dried via nitrogen. The cleaned slides were then silanized through immersion in Sigmacote (purchased from Sigma Aldrich) for 1 hour. The slides were then rinsed with acetone and dried with nitrogen. This provides a hydrophobic surface to allow the AcDEX polymer to adhere. To create a polymer film, 10 mg of AceDex was dissolved in 150 µL of anhydrous tetrahydrofuran. A 2 µL drop was drop-casted onto the silylated surface and allowed to air dry for 15 minutes. The spotted slides were then transferred into slide holders and placed under vacuum overnight to remove residual solvent. Microscopy characterization (light microscope and SEM) were used to determine smoothness of surface of the micropump.

### 4.2.3 Fabrication of micromotor

A monolayer of <1mm diameter amberlite particles (Aldrich IRA-400 chloride form, 20-25 mesh) was adhered to tape. This was to prevent movement of particles during the polymer-coating process. 50 mg of AcDEX was dissolved in 1 mL of methanol. The resulting solution was airbrushed 6 inches away from the amberlite particles using a Master Airbrush G233-SET Multi-Purpose Precision Dual-Action Gravity Feed Airbrush Professional Set. Particles were lifted off by mechanically onto a clean collection vessel. This was adapted from the protocol established in

Zhang, et al.[25] Stylus profilometry (KLA Tencore p16+ Stylus profilometer) was used to determine amount of polymer coating on the particles.

### 4.2.4 Experimental setup

A hybridization chamber (20 mm diameter, 1 mm deep, Grace Bio Labs SKU621111) was attached to the AcDEX micropump patches surface to provide a chamber for fluid and tracer particles in order to visualize fluid flow during pumping. Care was taken to ensure the polymer did not lift off the silylated glass surface due to electrostatics or accidental contact. Figure 4-2 illustrates the setup for a typical AcDEX micropumps, where the polymer patch was drop-casted onto a silanized surface.

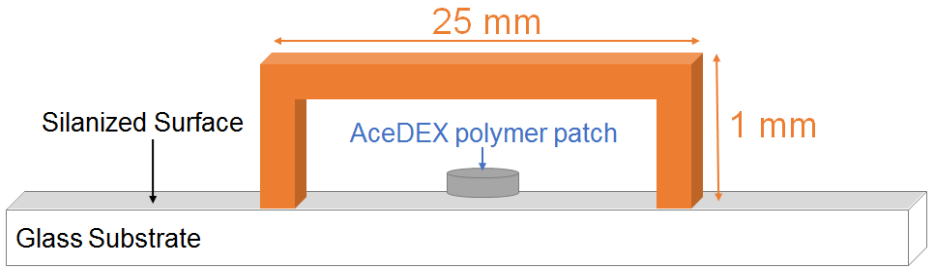


**Figure 4-2**. AcDEX polymeric micropump setup, showing dimensions of the chamber. The polymer patch is made by drop-casting onto a silanized surface and is typically 2 mm in diameter.

In a typical AcDEX micropump experiment, the chamber was filled with acidic solution containing tracer particles (aPSL and sPSL). During injection into the chamber, the solution was injected slowly to prevent disturbances to the polymer patch. Upon contact between the solution and the polymer, a timer was initiated to signal time t = 0 mins after addition and to keep track of exposure time. The concentrations of acid and the individual solutions used are described in the

results section. Fluid flow is characterized by the recording of tracer particle motion with an Olympus BX60M optical microscope (and in some cases, with a Zeiss Axiovert 200M Inverted microscope) with a Point Grey Flea3 camera. The individual particle movement were tracked and analyzed using Tracker video analysis software (by Cabrillo).

## 4.3 Analysis of AcDEX micropump

### 4.3.1 Fluid pumping behavior

While AcDEX polymers have been explored for its biomedical use, such as for time-dependent drug delivery purposes, it is often conducted under passive conditions. With the aim of converting passive AcDEX polymers into a potential active transport system, motion triggered by the degradation of AcDEX polymer was studied using a pump architecture. With this in mind, the micropump illustrated in Figure 4-2 was used to determine how different conditions can affect fluid flow and speeds.

In order to find out how different conditions influence to fluid flow and speeds, $AcDEX_{1hr}$ (removed from reaction at 1 hr time point) was exposed to a range of concentrations of a simple mono-protic acid (HCl) and a poly-protic acid (phosphoric acid) in a biologically compatible phosphate buffered solution. Figure 4-3 shows tracer particles being pumped away from the $AcDEX_{1hr}$ polymer, which is prevalent in all micropump experiments reported herein. Using the Tracker software, speed profiles over time were obtained for the degradation of $AcDEX_{1hr}$ polymers in the different acidic media (Figure 4-4). $AcDEX_{1hr}$ pumps show different speed profiles over time depending on the acid concentration.

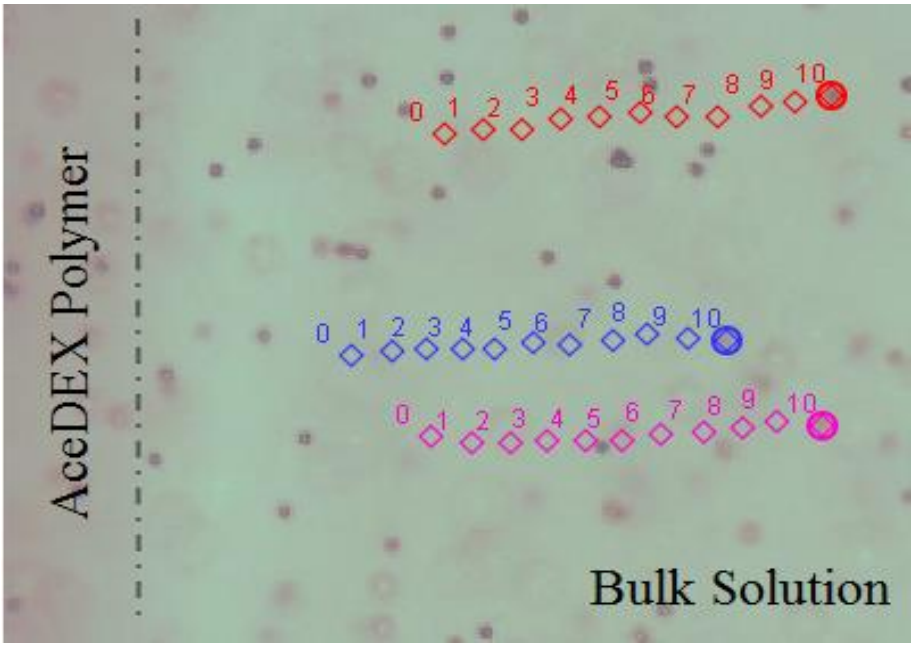


**Figure 4-3**. Time-lapsed tracking of tracer particles (polystyrene latex beads) in 10 mM HCl, showing fluid flow moving away from polymer edge. Particles are tracked every second for an average duration of 14 seconds.

At higher acid concentrations of 20 mM and 15 mM HCl, pump speeds rise rapidly after initial additions of acid from 4-6 µm/s to just below 10 µm/s that typically occur at the 7 and 10 minute mark respectively. After hitting a peak pumping speed, pumping slows down continuously until speeds plateau at around 1 µm/s. At lower acid concentrations of 10 mM and 5 mM HCl, the maximum pumping speeds are lower in comparison to speeds at higher concentrations. Since less degradation product is formed at the same time, the profiles are not as sharp as in higher acid concentrations. The max pumping speeds of 10 mM is almost double that of 5 mM while maximum speeds at 20 mM and 15 mM are relatively similar, hinting at an exponential relationship of maximum pumping speeds to acid concentration.

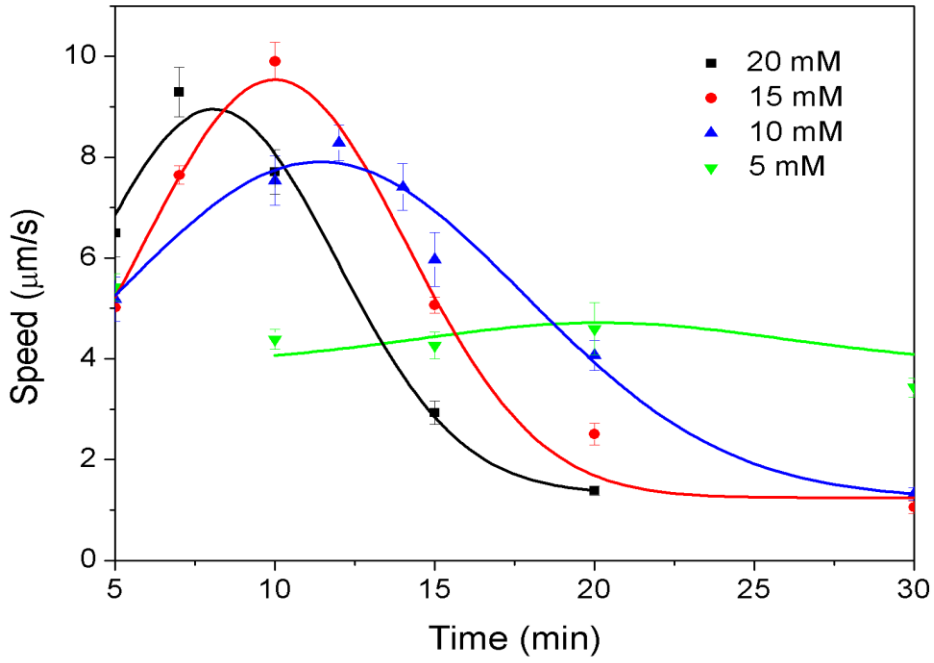


**Figure 4-4**. Speed profiles of $AcDEX_{1hr}$ micropumps when exposed to different concentrations of HCL over time. The data was fitted with $R^2$ values over 0.95 as a guide for the eye.

Aside from pumping speeds, it is interesting to note that the time at which the maximum pumping occur shifts over time as you decrease the acid concentration. This is due to the rapid consumption of $AcDEX_{1hr}$ polymer in higher acid concentration, creating faster pumping speeds at an earlier time frame. In addition, the degradation leads to the formation of ethanol and acetone which increases the solubility of the polymer. In comparison, the increase to maximum pumping and subsequent decrease in lower acid concentration is much more gradual and occur at longer time scales. It is, however, interesting that all of the pumps, regardless of acid concentration, seems to ultimately reach the same resting pump speed of about 1 μm/s for an observed period of 40-50 minutes. This results from speeds that can be maintained by a smaller $AcDEX_{1hr}$ patch as well as lower local concentrations of acetone and ethanol products at the polymer-surface interface.

To explore whether the pumping speeds of $AcDEX_{1hr}$ micropumps do indeed have an exponential relationship, Figure 4-5 plots the maxima speeds of $AcDEX_{1hr}$ micropumps for four different HCl concentrations. This graph has a good fit with an exponential curve fitting algorithm and shows that pumps reach a speed maximum that begins to level off at about 15 mM HCl. Therefore, max pump speeds and profiles can be tailored using the information obtained from Figure 4-5 by using not only acid concentrations, but time as an added dimension.

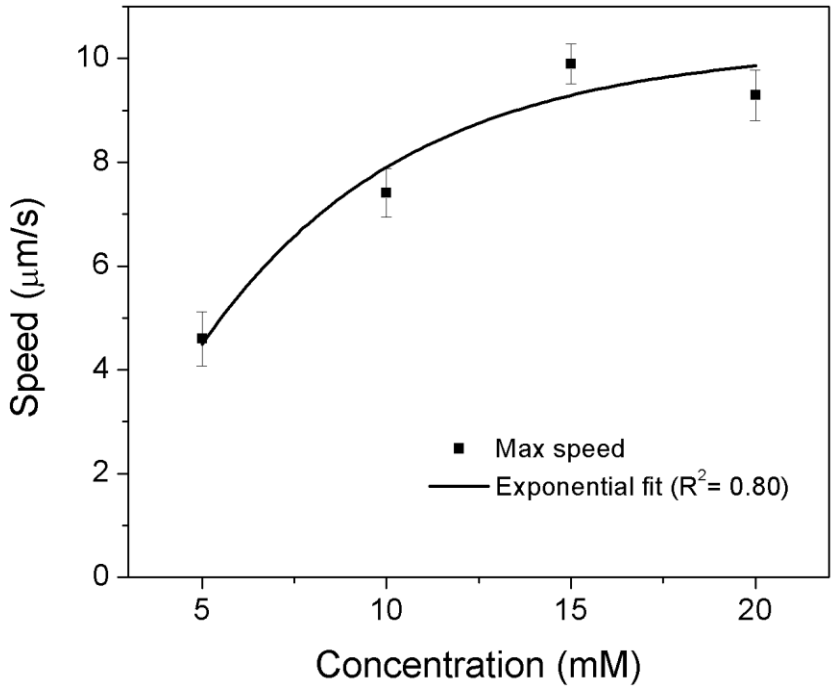


**Figure 4-5**. Maximum speeds of $AcDEX_{1hr}$ micropumps at different HCl concentrations. Curve fitted to exponential curve using OriginPro8.

Due to the intended usage of $AcDEX_{1hr}$ micropumps in biological systems, pump profiles in different buffered pH systems were also explored. Buffered pH solutions consisting of 10 mM phosphate buffered solution (10 mM sodium phosphate, 15 mM sodium chloride) was adjusted

with phosphoric acid dropwise until the desired pH was obtained. Figure 4-6 shows the profiles of $AcDEX_{1hr}$ pumping at different pH. The profiles for pH 1.5-2.5 are very similar to those of high acid concentrations in Figure 4-4. At lower acidic conditions for pH 3-4, however, the pump speeds leveled off almost immediately and maintain an almost-constant pumping speed.

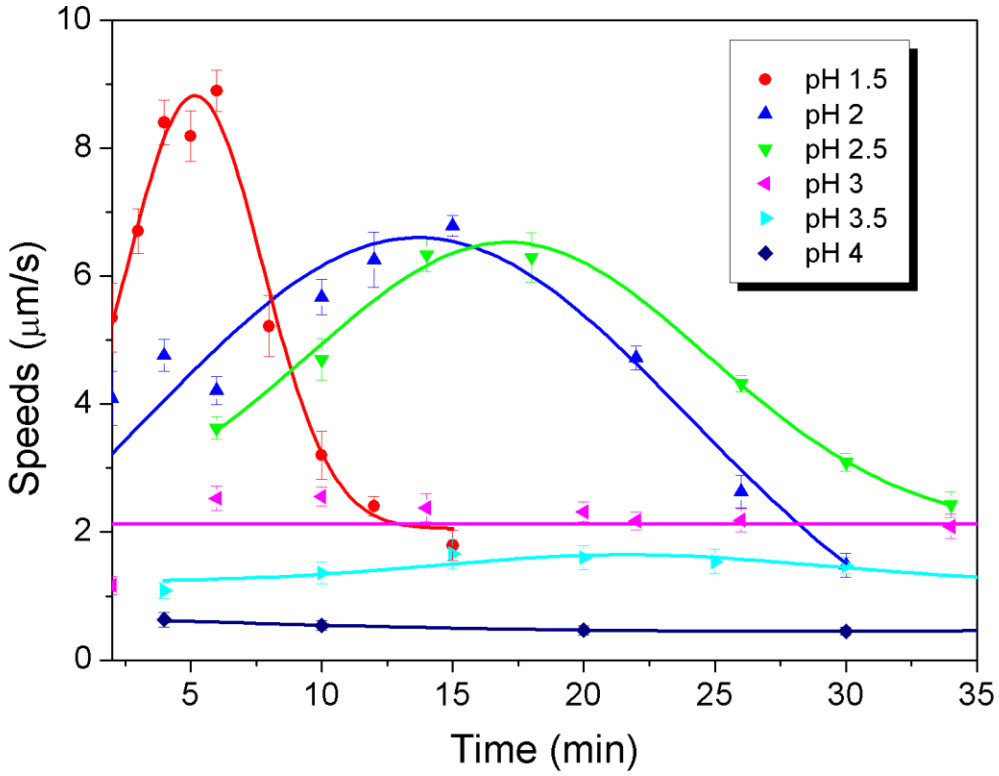


**Figure 4-6**. AcDEX pump profiles over time after exposure to phosphate buffered solutions.

The analysis of micropump motion in HCl and pH modulated phosphate buffered solutions illustrates two key factors: AcDEX micropumps can operate in ionic environments, such as in buffered systems and the simplified profiles obtained in HCl conditions can be used to correlate and understand the release of material in more complicated systems.

### 4.3.2 Characterization

Due to the drop-casting method of fabrication, this necessitates the analysis of surface detailing of AcDEX micropumps. Figure 4-7 shows the perspective of the microscope camera and an SEM image of a typical AcDEX patch.

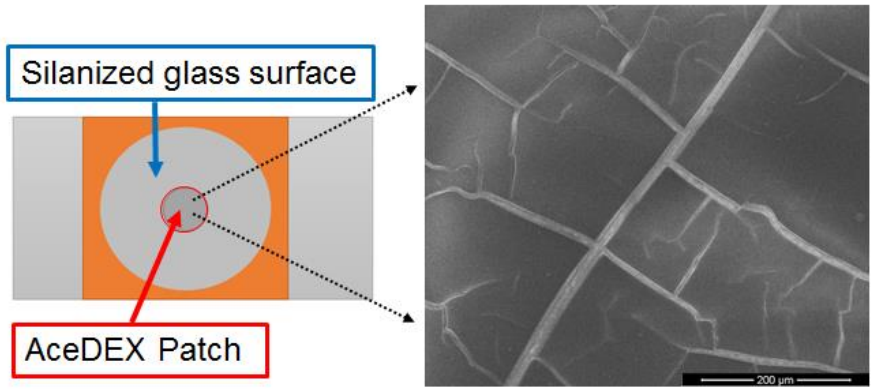


**Figure 4-7**. AcDEX micropump architecture, where the polymer was spotted onto silanized glass surface to form a thin film. Zoomed-in image shows an SEM scan of the typical pump surface, showing thin cracks microns in size formed from the drop-cast drying method. Scale bar on SEM image is 200 nm.

The patches consistently contain cracks on the surface that measures tens of microns as a result of the casting method. Due to the presence of cracks and the drop-casting process, the surface area of the polymer patch change, which in turn affects the pump speeds. Therefore, all results reported in the study used polymer patches about 2 mm in size with similar surface detailing to minimize random errors.

### 4.3.3 Mechanism

AcDEX is an acid-degradable polymer synthesized by adding protecting acetal groups on the dextran backbone. Due to the protecting groups, AcDEX is a relatively hydrophobic polymer that will not readily dissolve in water. Upon exposure to acidic media, the protecting acetal groups are converted to ethanol and acetone. The species that are formed is highly soluble in an aqueous environment. The degradation and dissolution of products likely leads to a local density gradient and will generate a density-driven flow away from the pump surface. Previously, Figure 4-1 and 4-4 was able to illustrate the reaction scheme and show the pumping directions the micropump relative to the pump orientation respectively. In order to verify the pumping mechanism, the pump was exposed to acidic fuel in an upright and an inverted setting.

Fluid flows were observed to be moving away from pump-surface interface when the pump is upright while fluid flows towards the interface in an inverted system. Figure 4-8 illustrates the resulting flows observed, in upright and inverted architecture. This is indicative of a density-driven flow, as the products of the degradation reaction (ethanol, acetone, and dextran) is denser than the starting reactants. For the reactants, only acid is taken into account as the AcDEX polymer itself is stationary.

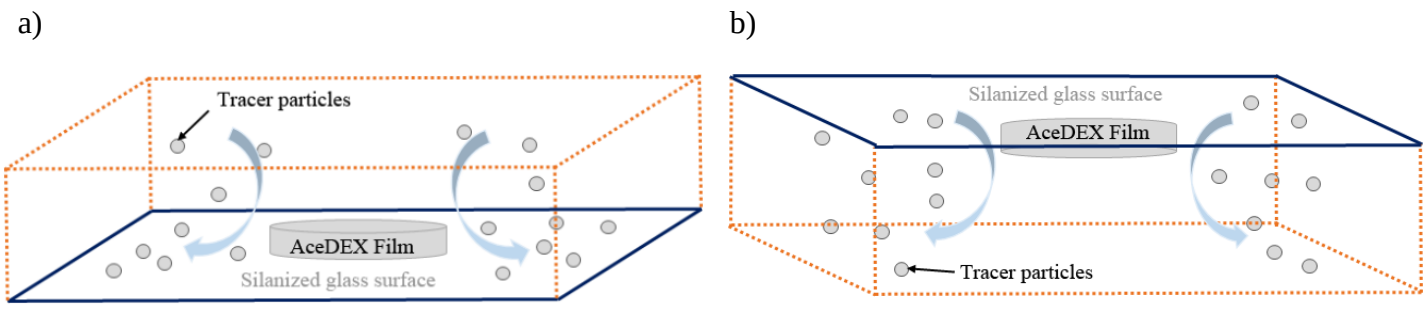


**Figure 4-8**. Pumping directions observed for (a) upright AcDEX micropump and (b) inverted AcDEX micropump, showing inversion of fluid flow supporting a density-driven flow mechanism.

In an upright pump (Figure 4-8a), fluid flows away from the AcDEX pump outwards. In the presence of a density-driven flow, an upright pump will cause the denser products to accumulate and flow away from the pump surface. In an inverted pump (Figure 4-8b), fluid flows in the opposite direction, inwards toward the AcDEX pump. In an inverted pump, however, the dense products will sink in the chamber away from the AcDEX patch, causing fluid to move inwards to fill the void. This is in line with experimental observations.

The previous section already detailed how fluid flow speeds can be correlated to acidic concentrations. Pump speeds and direction have been attributed to the degradation of the polymer. Therefore, the greater the amount of acetalated endgroups along the polymer backbone, the slower the pump initiation and speeds should be as the presence of acetal groups retard AcDEX degradation and dissolution into aqueous solution. This has been shown to be the case in previously reported in-depth NMR and degradation studies.[13,23] Figure 4-9 shows how acetal content changes over reaction time, providing an estimate on the increase in acetal content with respect to reaction time.[13] Figure 4-10 shows a comparison of speed profiles at the same acid concentration (10 mM HCl) for AcDEX polymers that were reacted for different lengths of time (10 minutes, 1 hour, and 6 hour).

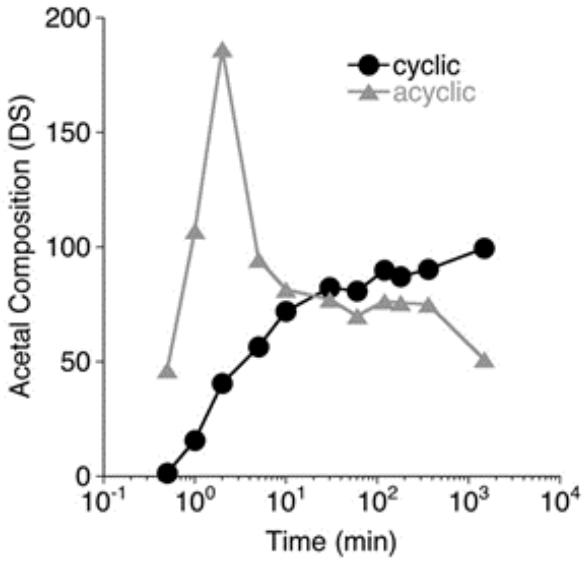


**Figure 4-9.** Degree of acetal substitution on dextran over time, showing increase of coverage as reaction time increases. Initial burst of coverage is primarily due to acyclic acetals, which are then slowly replaced by cyclic acetals. Reproduced with permission from Reference 13. Copyright 2009, National Academy of Sciences, USA.

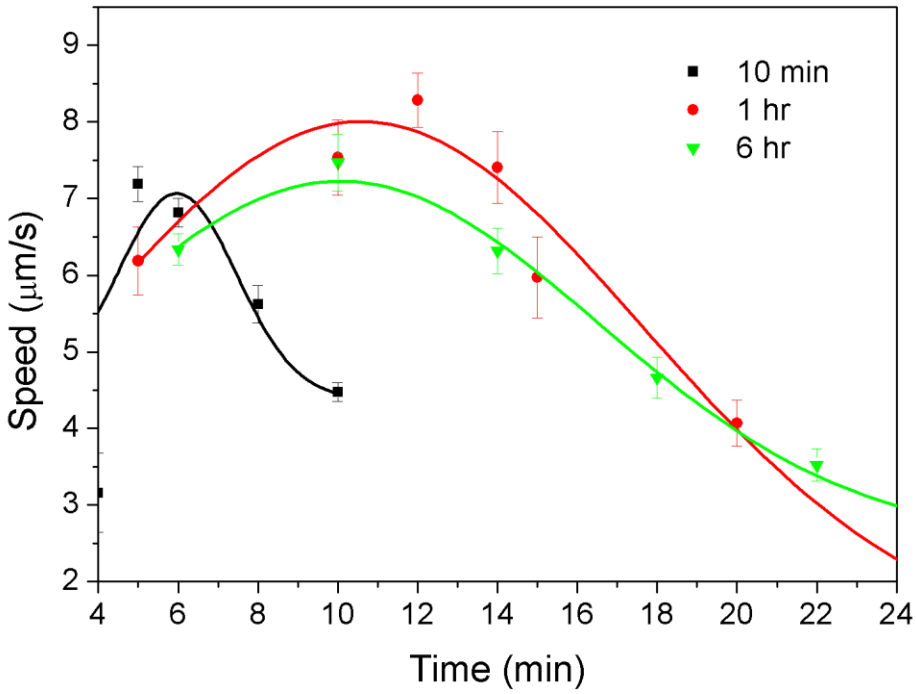


**Figure 4-10**. Speed profiles of AcDEX pump fabricated with polymers removed from reaction vessel at different times. All pumps were exposed to 10 mM HCl solution.

The longer the polymer was allowed to react during initial synthesis, the more acetalated end groups are present along the backbone.[13] The polymer removed after 10 minutes of reaction ($AcDEX_{10min}$) shows a rapid degradation profile that occurs over roughly 10 minutes. It is an extremely volatile system and large variations were observed in both timescale and max pumping speeds for $AcDEX_{10min}$. The polymer removed after 6 hours ($AcDEX_{6hr}$) shows a similar degradation profile to polymer removed after 1 hour ($AcDEX_{1hr}$). Both reach pumping maxima around the same time point. $AcDEX_{6hr}$, however, show slightly lower pumping speeds across the full degradation timescale in comparison to $AcDEX_{1hr}$. This is caused by the faster degradation/dissolution of $AcDEX_{1hr}$ since it has less acetal content. At around the 20 min time point, there is a crossover where pump speeds of $AcDEX_{6hr}$ overtakes $AcDEX_{1hr}$. This is caused by the slowing down of pumping in $AcDEX_{1hr}$ micropump resulting from initial signs of polymer exhaustion in the reaction. Therefore, the amount of acetal protecting endgroups coverage is another factor that can be utilized to tailor AcDEX pump speeds and material release profile.

## 4.4 Analysis of AcDEX micromotors

### 4.4.1 Motion analysis

In order for AcDEX to be used as an active response drug delivery agent, a Janus motor containing AcDEX polymer was fabricated. $AcDEX_{1hr}$ polymer was airbrushed onto Amberlite to create Janus particles roughly 0.7-0.85 mm in size. When placed in contact with dilute acid at the air-solution interface, the motors can move tens to hundreds of body-lengths per second depending on the acid concentration. In 1 M HCl, the particles move at 29.3 ± 9.5 mm/s. In 5 M HCl, the

particles move at 485.3 ± 105.7 mm/s. Figure 4-11 shows an AcDEX motor moving in acidic solution

The motors show promise as directed delivery agents due to their fast speeds with relatively low amounts of active material in comparison to the size of the entire Amberlite particle. The speeds, however, do have a relatively large standard deviations in motor speeds as a result of the airbrush method. While airbrushing puts a solid layer of polymer onto all the Amberlite particles, there will be variations of thickness as the airbrushed solution dries. While the system has this inherent randomness, the order of magnitude in the speeds between exposures to lower vs. higher acid concentrations are still extremely consistent.

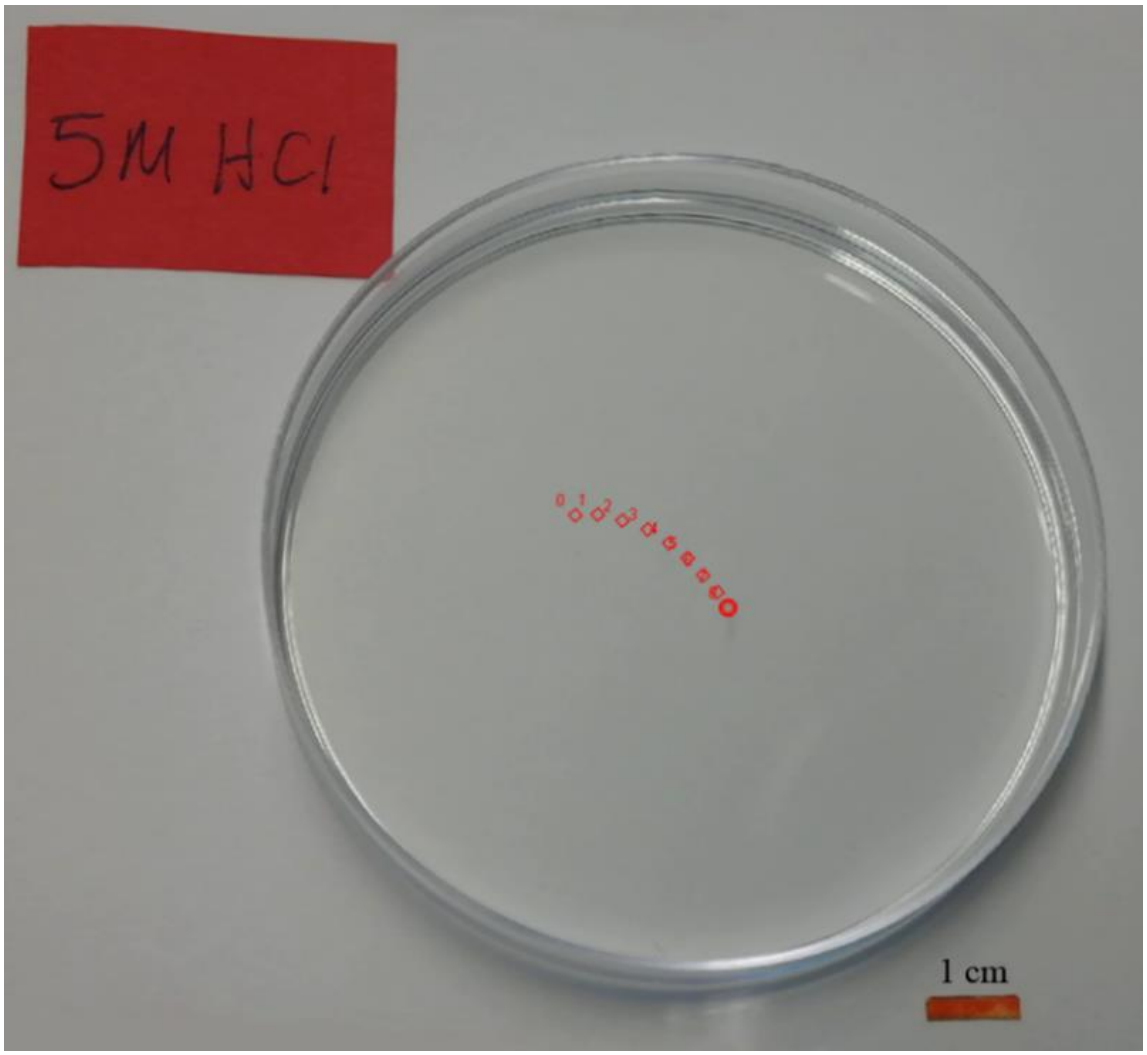


**Figure 4-11.** Movement of AcDEX-coated Janus particles in 5 M HCl over time. Each marked movement of the motor occurred over 0.05 seconds.

### 4.4.2 Mechanism

Similar to AcDEX micropumps, the polymer Janus motors operate via acid degradation. Figure 4-12 illustrates the details of AcDEX motor movement. The degradation produces products that dissolve into the acidic solution at the air-solution interface, which lowers the surface tension on the polymer end. This produces a surface tension gradient across the motor, which creates a force that moves the particle towards the area of higher surface tension.

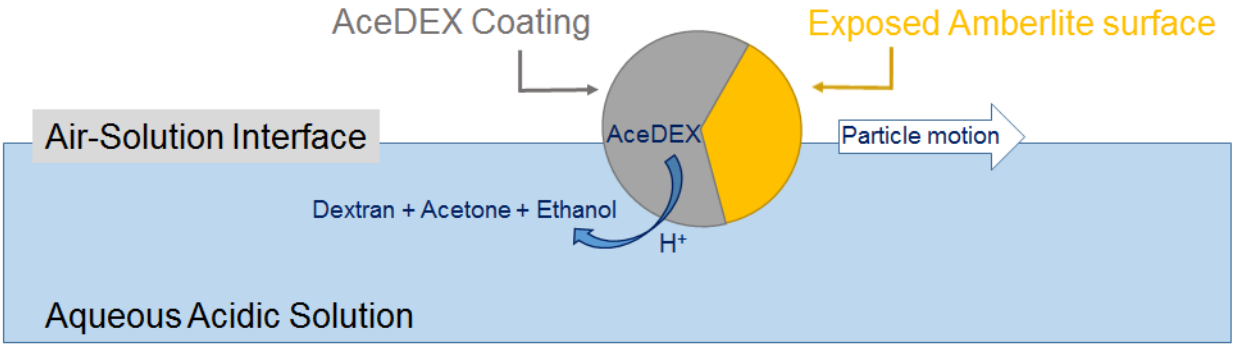


**Figure 4-12**. Mechanism for motion of AcDEX Janus particles in acidic solution.

### 4.4.3 Characterization

It has been established that AcDEX is a versatile material that can easily be made or applied in different forms.[20] This was the main reason why AcDEX Janus motors were easily fabricated using a solution airbrush method. In order to determine the relative amount of polymer that has been airbrushed onto Amberlite to make Janus particles, profilometry experiments were conducted. Figure 4-13 shows a profilometry profile of the airbrushed polymer on a glass surface done at the same time as motor fabrication, showing that the AcDEX film is not very uniform. Therefore, there can be variations in the amount of AcDEX polymer on each particle.

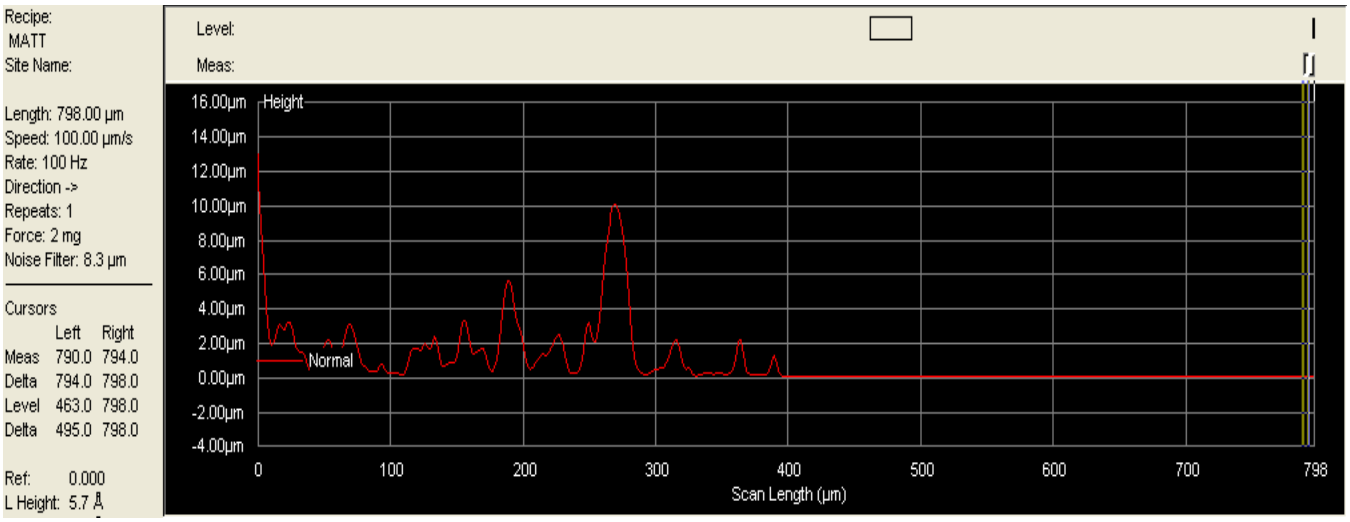


**Figure 4-13.** Stylus profilometry experiment for AcDEX polymer patch thickness for airbrushed motor fabrication, taken using a KLA Tencore p16+ stylus profilometer. The flat area past 400 µm serves as the leveling blank, which is an area of glass that was not exposed to the airbrushed polymer.

The slight differing amounts of airbrushed polymer on the Janus motors will impact speeds and duration of motor movement. The other cause for large deviations is random error due to the angle of the particles when introduced to the solution. The motor particles are dropped individually into the acidic solution. As such, the amount of exposure the AcDEX patch has to the solution is randomized.

## 4.5 Conclusion

While acetalated dextran polymer has been attracting attention as a drug delivery and therapeutic agent, most of the studies only revolve around the timed release of materials. The work conducted in this dissertation provides in-depth analysis of fluid flow and particle motion that arises directly from the degradation of the AcDEX polymer. It was found that the micropump fabricated using AcDEX can easily reach 7-10 µm/s fluid speeds, allowing for rapid release and

delivery of potential payload within short timespans. Tailoring of multi-faceted conditions can also allow for slow, steady release of material. These speeds are not only comparable to other chemical responsive polymer-based micropumps, it uses an order of magnitude less fuel or multiple orders of magnitude less polymer. [24,25] In addition, AcDEX polymer has an advantage over others when used to produce motion. The previously reported stimuli responsive polymer micropumps are based on a depolymerization approach.[24,25] Thus the extent of pumping depends on the accessibility of the polymer end caps to the external stimuli.[26] In the current approach the acid labile acetal groups are present throughout the dextran backbone, and unlike the predecessors, these micropumps can undergo facile degradation to initiate pumping of fluid.

AcDEX was also coated onto a particle to create a Janus motor capable of hundreds of body lengths in acidic media. This serves as a proof-of-concept that directional nano- and micromotors can be fabricated with AcDEX polymer for chemotactically-directed delivery systems. This study provides the fundamentals necessary to further the understanding of stimuli response polymer-based delivery systems as AcDEX is an emerging biomaterial that shows promise in biological applications.

## 4.6 References


1. Cohen Stuart, M. A.; Huck, W. T. S.; Genzer, J.; Müller, M.; Ober, C.; Stamm, M.; Sukhorukov, G. B.; Szleifer, I.; Tsukruk, V. V.; Urban, M.; Winnik, F.; Zauscher, S.; Luzinov, I.; Minko, S. Emerging applications of stimuli-responsive polymer materials. *Nat. Mater.* **2010**, *9*, 101-113.
2. Roy, D.; Cambre, J. N.; Sumerlin, B. S. Future perspectives and recent advances in stimuli-repsonsive materials. *Prog. Polym. Sci.* **2010**, *35*, 278-301.
3. Cabane, E.; Zhang, X.; Langowska, K.; Palivan, C. G.; Meier, W. Stimuli-responsive polymers and their applications in nanomedicine. *Biointerphases* **2012**, *7*, 9.
4. Benetti, E. M.; Zapotoczny, S.; Vancso, G. J. Tunable thermoresponsive polymeric platforms on gold by "photoiniferter"–based surface grafting. *Adv. Mater.* **2007**, *19*, 268-271.
5. Verma, R.; Adhikary, R. R.; Banerjee, R. Smart material platforms for miniturizatized devices: implications in disease models and diagnostics. *Lab Chip* **2016**, *16*, 1978-1992.
6. Schäfer, C. G.; Winter, T.; Heidt, S.; Dietz, C.; Ding, T.; Baumbergc, J. J.; Gallei, M. Smart polymer inverse–opal photonic crystal films by melt-shear organization for hybrid core–shell architectures. *J. Mater. Chem. C* **2015**, *3*, 2204-2214.
7. Liechty, W. B.; Kryscio, D. R.; Slaughter, B.V.; Peppas, N. A. Polymers for drug delivery systems. *Annu. Rev. Chem. Biomol. Eng.* **2010**, *1*, 149-173.
8. Kauffman, K. J.; Kanthamneni, N.; Meenach, S. A.; Pierson, B. C.; Bachelder, E. M.; Ainslie, K. M. Optimization of rapamycin-loaded acetalated dextran microparticles for immunosuppression. *Int. J. Pharm.* **2012**, *422*, 356-363.
9. Pannier, A. K.; Shea, L. D. Controlled release systems for DNA delivery. *Molecular Therapy* **2004**, *10*, 19-29.
10. Yu, Y.; Si, Y.; Bechler, S. L.; Liu, B.; Lynn, D. M. Polymer multilayers that promote the rapid release and contact transfer of DNA. *Biomolecules* **2015**, *16*, 2998-3007.
11. Fang, F.; Szleifer, I. Controlled release of proteins from polymer-modified surfaces. *Proc. Nat. Acad. Sci.* **2006**, *103*, 5769-5774.
12. Koyamatsu, Y.; Hirano, T.; Kakizawa, Y.; Okano, F.; Takarada, T.; Maeda, M. pH–responsive release of proteins from biocompatible and biodegradable reverse polymer micelles. *J. Control. Release* **2014**, *173*, 89-95.
13. Broaders, K. E.; Cohen, J. A.; Beaudette, T. T.; Bachelder, E. M.; Fréchet, J. M. J. Acetalated dextran is a chemically and biologically tunable material for particulate immunotherapy. *Proc. Nat. Acad. Sci.* **2009**, *106*, 5497-5502.
14. Adhikary, R. R.; More, P.; Banerjee, R. Smart nanoparticles as targeting platforms for HIV infections. *Nanoscale* **2015**, *7*, 7520-7534.
15. Zhang, Y.; Chan, H. F.; Leong, K. W. Advanced materials and processing for drug delivery: the past and the future. *Adv. Drug Deliv. Rev.* **2013**, *65*, 104-120.
16. Zhang, X.; Yang, P.; Dai, Y.; Ma, P.; Li, X.; Cheng, Z.; Hou, Z.; Kang, X.; Li, C.; Lin, J. Multifunctional up-converting nanocomposits with smart polymer brushes gated mesopores

for cell imaging and thermo/pH dual-responsive drug controlled release. *Adv. Funct. Mater.* **2013**, *23*, 4067-4078.

17. Binauld, S.; Stenzel, M. H. Acid-degradable polymers for drug delivery: a decade of innovation. *Chem. Commun.* **2013**, *49*, 2082-2102.
18. Kato, Y.; Ozawa, S.; Miyamoto, C.; Maehata, Y.; Suzuki, A.; Maeda, T.; Baba, Y. Acidic extracellular microenvironment and cancer. *Cancer Cell Int.* **2013**, *13*, 89.
19. Bachelder, E. M.; Beaudette, T. T.; Broaders, K. E.; Dashe, J.; Fréchet, J. M. J. Acetal-derivatized dextran: an acid–responsive biodegradable material for therapeutic applications. *J. Am. Chem. Soc.* **2008**, *130*, 10494-10495.
20. Borteh, H. M.; Gallovic, M. D.; Sharma, S.; Peine, K. J.; Miao, S.; Brackman, D. J.; Gregg, K.; Xu, Y.; Guo, X.; Guan, J.; Bachelder, E. M.; Ainslie, K. M. Electrospun acetalated dextran scaffolds for temporal release of therapeutics. *Langmuir* **2013**, *29*, 7957-7965.
21. Schully, L. L.; Sharma, S.; Peine, K. J.; Pesce, J.; Elberson, M. A.; Fonseca, M. E.; Prouty, A. M.; Bell, M. G.; Borteh, H.; Gallovic, M.; Bachelder, E. M.; Keane-Myers, A.; Ainslie, K. M. Rapid vaccination using an acetalated dextran microparticulate subunit vaccine confers protection against triplicate challenge by *Bacillus Anthracis*. *Pharm. Res.* **2013**, *30*, 1349-1361.
22. Bachelder, E. M.; Beaudette, T. T.; Broaders, K. E.; Fréchet, J. M. J.; Albrecht, M. T.; Mateczun, A. J.; Ainslie, K. M.; Pesce, J. T.; Keane-Myers, A. M. In vitro analysis of acetalated dextran microparticles as a potent delivery platform for vaccine adjuvants. *Mol. Pharmaceutics* **2010**, *7*, 826-835.
23. Kauffman, K. K.; Do, C.; Sharma, S.; Gallovic, M. D.; Bachelder, E. M.; Ainslie, K. M. Synthesis and characterization of acetalated dextran polymer and microparticles with ethanol as a degradation product. *ACS Appl. Mater. Interfaces* **2012**, *4*, 4149-4155.
24. Zhang, H.; Yeung, K.; Robbins, J. S.; Pavlick, R. A.; Wu, M.; Liu, R.; Sen, A.; Phillips, S. T. Self-powered microscale pumps based on analyte-initiated depolymerization reactions. *Angew. Chem. Int. Ed.* **2012**, *51*, 2400-2404.
25. Zhang, H.; Duan, W.; Liu, L.; Sen, A. Depolymerization–powered autonomous motors using biocompatible fuel. *J. Am. Chem. Soc.* **2013**, *135*, 15734-15737.
26. DiLauro, A. M.; Zhang, H.; Baker, M. S.; Wong, F.; Sen, A.; Phillips, S. T. Accessibility of responsive end-caps in films composed of stimuli–responsive, depolymerizable poly(phthalaldehydes). *Macromolecules* **2013**, *46*, 7257-7265.

# Chapter 5 Biocompatible and biodegradable micropump based segmented nanobattery

## 5.1 Introduction

With the advancements in nanotechnology, the realization of micromachines for real-world applications have become ever so attainable. This is especially true for the miniaturization of biomedical devices and implants due to the development of lithography and nanoassemblies. Microfabricated devices for bio-applications have led to the development of medical devices/therapeutics, biosensors, cellular tools/devices, and molecular tools/devices.[1-4] While the design and fabrication of small devices allows for advantages (*e.g.* low cost, ease of implantation, rapid recovery), methods to power such devices have lagged behind. Due to the environment in which these devices operate in, traditional batteries and external power sources are not optimal. This is especially true for micromachines and devices intended for implantation use.[5]

In recent years, the development of biodegradable materials for *in vivo* uses have been on the rise. The same holds true for power sources for implantable medical devices as it offers biocompatibility and avoid additional procedures required for removal.[6-10] Ideal biodegradable batteries should derive electric energy from its surrounding environment and should naturally degrade over time without producing cytotoxic by-products. This is similar in mechanism to how active colloidal nano- and micromotor species operate, as they harvest energy from the ambient.[11-15] Many reported nano- and micromotor systems, however, have difficulty operating in biological conditions due to high ionic strengths and limited fuel compatibility. While there are motors and pump systems that are biocompatible, such as polymer-based and enzyme-based systems, they face other issues such as fuel concentration/compatibility and suffer from slow speeds in comparison to electrokinetically-dominated systems.[16-19] Electrokinetic locomotion, on the other

hand, is incompatible with the high ionic strength media typical of biofluids.[20-22] By utilizing newly developed biodegradable nanobattery devices, it may therefore be feasible to generate large speeds of fluid flow and particle transport while maintaining its biocompatibility. This will enable the expansion of the types of motors and pumps that are operational *in vivo*. In this chapter, a biodegradable zinc-iron micropump that is based on a nanobattery is reported. It operates in a wide range of chemicals and is not impeded by high ionic conditions (examined in up to 3M salt). This system provides an excellent new class of material for bio-applications as it combines electrokinetic mechanisms and density-driven flows to transport fluid and particles without the usual issues that plague electrokinetic systems.

## 5.2 Experimental details

### 5.2.1 Fabrication

The bimetallic pump was fabricated using two separate systems: a Semicore E-gun Thermal Evaporator and a Kurt Lesker CMS-18 Multi Target RF Sputter System. A 200 nm layer of iron was e-beam evaporated onto pre-cleaned glass slides when vacuum pressure within process chamber was below 2 x $10^{-6}$ mTorr. System was allowed to cool completely before removal of sample to minimize oxidation of iron surface. Immediately following removal, a mask containing a 7 mm diameter cutout was placed above the iron-deposited slide. A 1 μm layer of zinc was sputtered at 100°C using a Kurt Lesker CMS-18 unit without a stage bias when vacuum pressure within the process chamber reached a minimum of $10^{-7}$ mTorr to reduce sample oxidation during sputtering. Sample was allowed to cool completely before sample removal. The individual samples were placed in slide holders to prevent scraping of the pump surface and stored in vacuum dessicator.

### 5.2.2 Experimental setup

A hybridization chamber (20 mm diameter, 1 mm deep, Grace Bio Labs SKU621111) was attached to the micropump surface to provide a chamber for fluid and tracer particles in order to visualize fluid flow during pumping. Figure 5-1 shows an actual micropump setup used for the experiments. In a typical micropump experiment, the hybridization chamber was filled with a solution that contains suspended positively charged tracer particles (amidine polystyrene latex or aPSL) or negatively-charged (sulfate polystyrene latex or sPSL) particles. The fluid flow was recorded using the 5x objective on an Olympus BX60M optical microscope while inverted setups were recorded with a Zeiss Axiovert 200M microscope fitted with a Point Grey Flea3 camera. The fluid flow was characterized with the Tracker video analysis software by Cabrillo.

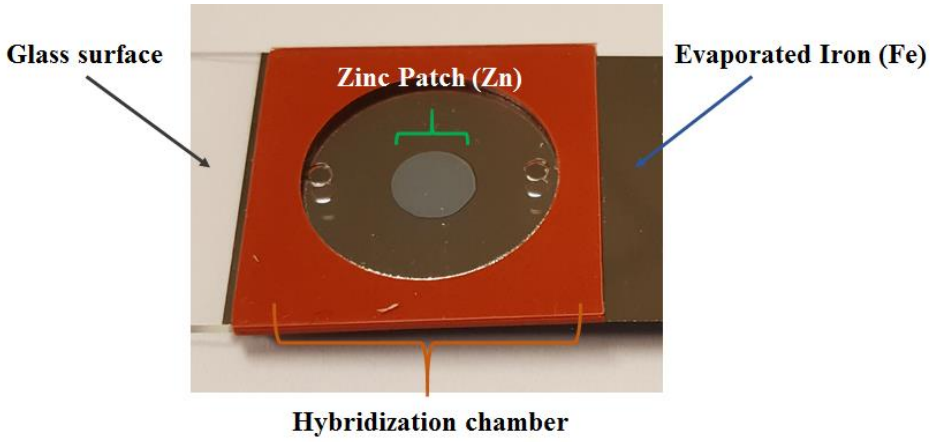


**Figure 5-1.** Zinc-iron micropump setup, with a hybridization chamber 20 mm in diameter and 1 mm in height. Iron has a metal sheen while zinc takes on a matte grey color due to mild surface oxidation.

## 5.3 Micropump characterization

### 5.3.1 Height characterization

As the amount of zinc present in the micropump will influence the pump speeds, profilometry was employed to ensure consistent patch thickness between samples. Figure 5-2 shows a measurement of the height of sputtered zinc in a typical micropump. Due to the rough surface, exact height of zinc patches were difficult to obtain. Micropumps used in experiments were therefore required to display a similar profile as the one below before experiments were conducted to ensure consistency.

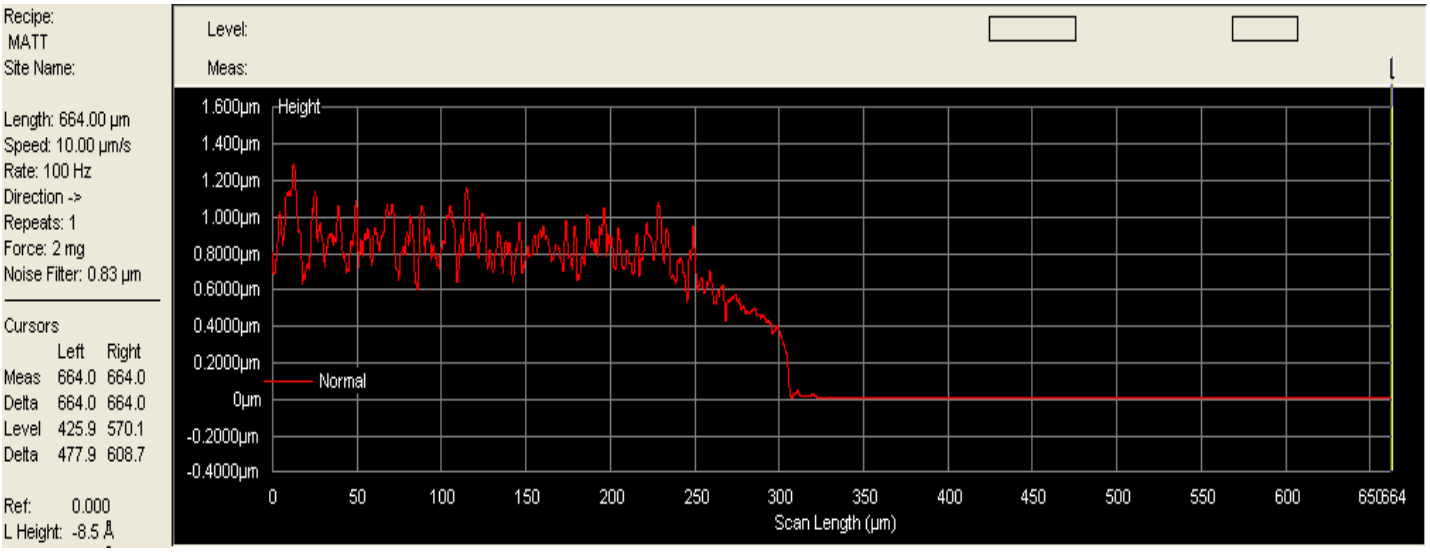


**Figure 5-2.** Stylus profilometer data on sputtered zinc under conditions described in fabrication section. The zinc was sputtered on a silicon wafer with a piece of kapton tape to mask an area. The flat measured area after 300 µm is clear silicon wafer, used as an internal standard.

### 5.3.2 Surface characterization

The metal surfaces of both zinc and iron were examined under the scanning electron microscope to ensure adhesion and is free of surface defects (*e.g.* cracks). By concentrating the electron beam on the Zn-Fe interface of a typical micropump, zinc can be seen to be sputtered onto iron as granular material (Figure 5-3). There is an excellent adhesion between the two metals, illustrated by the gentle slope present from the 1 μm layer of zinc to the flat iron layer below.

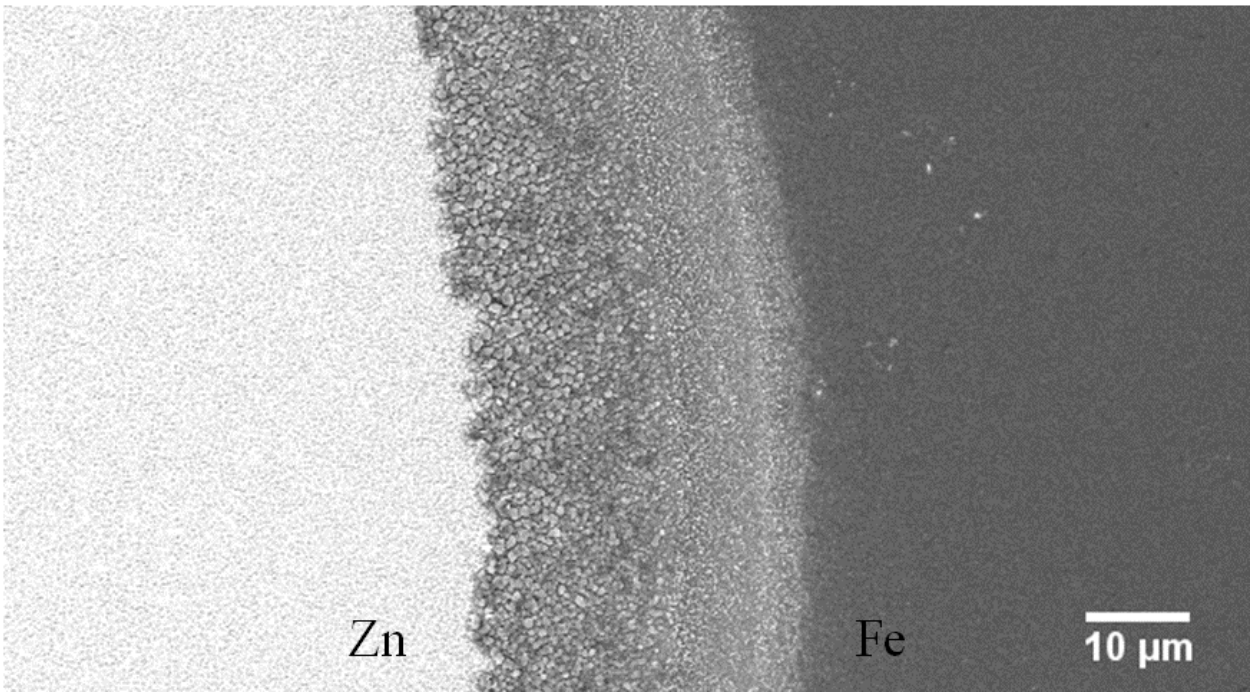


**Figure 5-3.** Magnified SEM image of Zn-Fe micropump, focusing on the interface.

Further trials shows that while surface oxidation occurs due to the reactivity of the metals, it is not overwhelming when deposited at low pressures ($10^{-7}$ mTorr) after flushing chamber with argon gas. As seen in Figure 5-1, the zinc has a matte grey appearance. When zinc is deposited at higher pressures ($10^{-6}$ mTorr), the surface of the zinc contains a black, dust-like coating as a result of forming a large amount of zinc oxide.

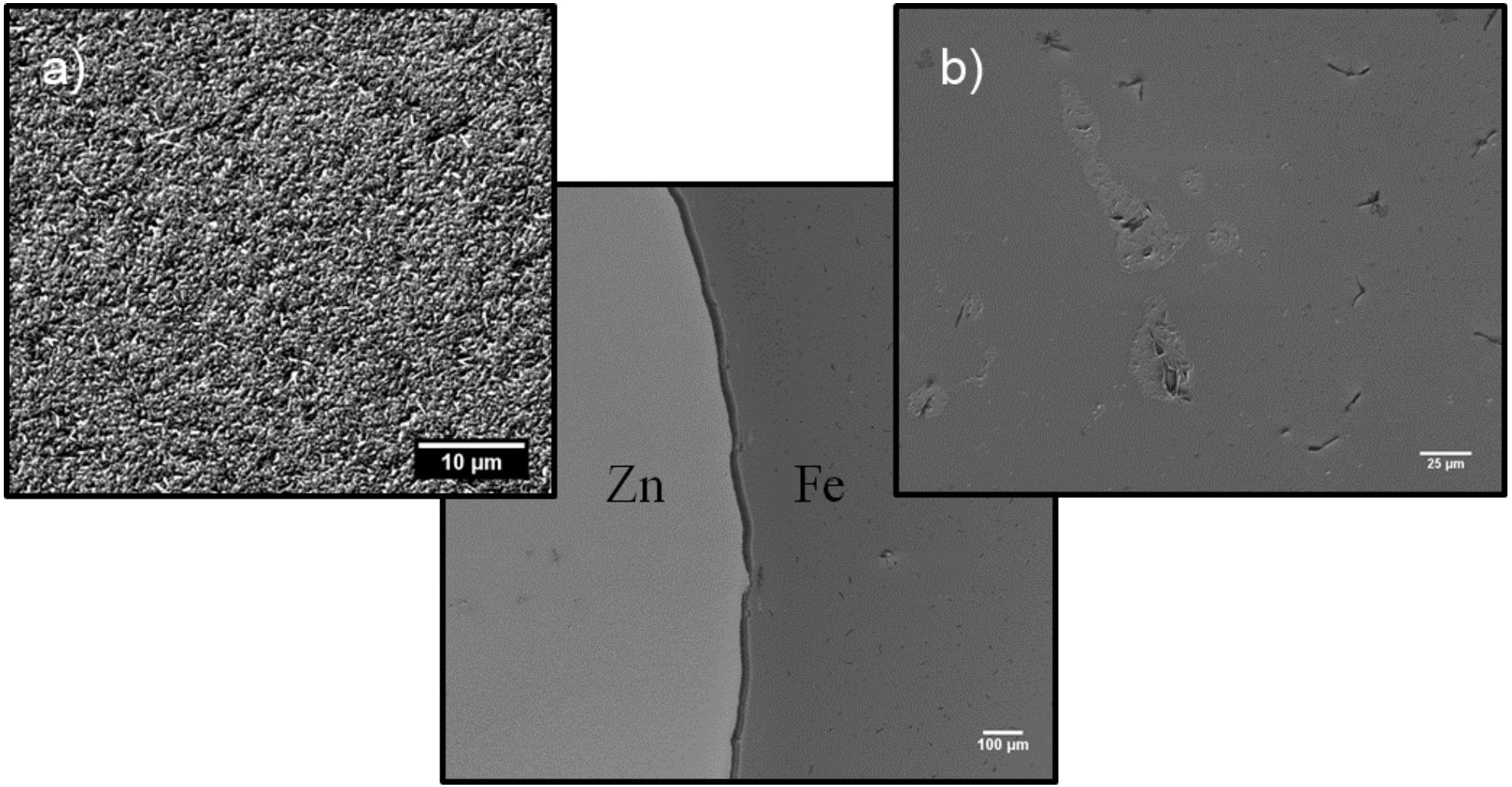


**Figure 5-4.** SEM surface image of Zn-Fe micropump, showing magnified surface detailing of zinc (a) and iron (b).

To ensure that the deposited metals are free of large surface defects, magnified SEM images detailing the surface of both zinc and iron were taken (Figure 5-4). In Figure 5-4A, it can be seen that the surface of sputtered zinc is a relatively flat with minor ridge detailing on the order of a couple microns. In Figure 5-4B, evaporated iron is shown to be an extremely smooth film with small rips about 10-25 μm in length. This is partly due to no adhesion layer being used between iron and the glass surface. The iron layer, however, does not lift off the glass surface and maintains excellent adhesion.

## 5.4 Fluid flows characterization and mechanism in acidic media

### 5.4.1 Simple Acid – Aqueous hydrochloric acid

Zinc is known to be an acid-sensitive material. It reacts and forms hydrogen gas and a zinc salt, shown by a general equation (eq. 1).

$$Zn_{(s)} + 2HB \rightarrow ZnB_2 + H_{2(g)} \qquad (1)$$

Through the generation of bubbles and possible electrokinetic contributions due to the contact between iron and zinc, it has the potential to be converted into a micropump system. Using HCl (a simple protic acid), different concentrations of HCl was introduced into a Zn-Fe micropump architecture to probe fluid flows and mechanisms.

Figure 5-5 is a speed profile of Zn-Fe micropump when exposed to different concentrations of HCl. When the individual data are fit to an exponential curve, it can be seen that pumps eventually reach a terminal velocity at around 10 μm/s. This seems to be the case for lower HCl concentrations as low as 2.5 mM HCl, showing an extremely high reactivity of zinc to acid. At low acid concentrations, bubbles were not observed in the micropump system. Therefore,

bubble formation is not a factor of disturbance in the sealed micropump. In addition, the speed profiles for lower acid concentrations (2.5 mM and 5 mM HCl) shows an exponential growth of fluid pumping speeds until it reaches the terminal velocity. This is indicative of some other mechanistic influence in addition to the expected electrokinetic mechanism.

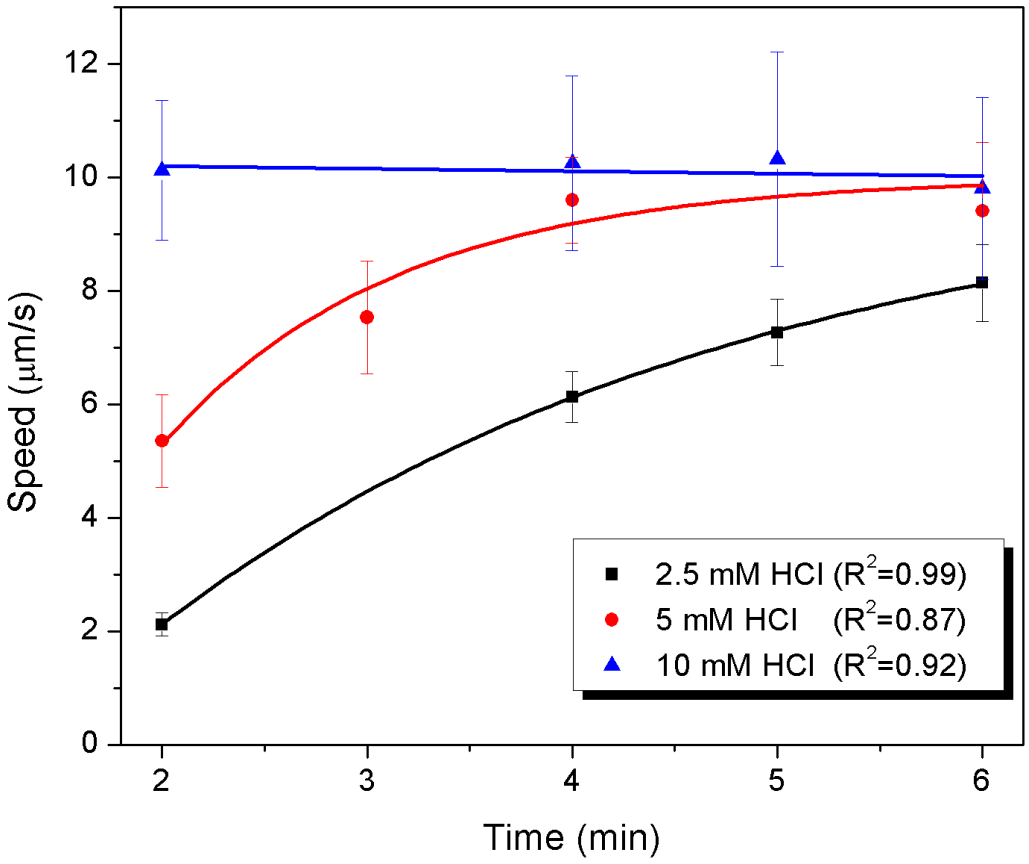


**Figure 5-5.** Fluid pumping profiles with respect to time for Zn-Fe micropumps in various concentrations of aqueous acidic media. Curves were fit with exponential growth curve fitting algorithms in OriginPro8, with good confidence. Curve fitting for 10 mM HCl was done via linear fit instead as it seems the pump reached terminal velocity and there was no real speed change over the duration of the tracking period.

### 5.4.2 Mechanism

To explore the mechanism for Zn-Fe micropump in acidic media, the micropump was probed to positively charged and negatively charged tracer particles. Both types of tracer particles are pumped outwards from the Zn-Fe interface, showing no selectivity to the charge of the tracer particle. The micropump was also examined in an inverted setting. If the micropump operates on an electrokinetic mechanism, direction of pumping will not reverse. However, if other mechanisms are present, then this will impact fluid flow and speeds.

In an inverted micropump setting, the direction of fluid flow is reversed. The tracer particles are seen moving *towards* the Zn-Fe interface, albeit at a slower speed. A density-driven flow is suspected to be present and impedes the electroosmotic flow present on the pump surface due to the higher density of products ($ZnCl_2$) in comparison to the starting material (HCl).

When Zn-Fe micropump is exposed to HCl, the following reactions occur readily:

$$Zn_{(s)} \rightarrow Zn^{2+} + 2\ e^- \qquad (2)$$

$$2\ HCl_{(aq)} \rightarrow 2\ H^+ + 2\ Cl^- \qquad (3)$$

$$2\ H^+ + 2\ e^- \rightarrow H_{2(g)} \qquad (4)$$

Using half reactions eq. 2-4, Figure 5-6 illustrates a mechanism that shows the asymmetric redox reaction occurring on opposite ends of the metals as well as the density flows generated from the formation of zinc chloride.

Further evidence that supports this mechanism is the formation of bubbles in higher acid concentrations. In 20 mM HCl, hydrogen bubbles are formed but is predominately above the iron patch as oppose to the zinc patch, illustrated in Figure 5-7. Due to the formation of bubbles, concentrations above 10 mM HCl were avoided to prevent disturbance of fluid flows by bubble interference. It is interesting, however, that at 5 mM HCl and lower concentrations, bubbles that

may have been formed are not visible to the naked eye or when magnified at 50x for extended periods of times.

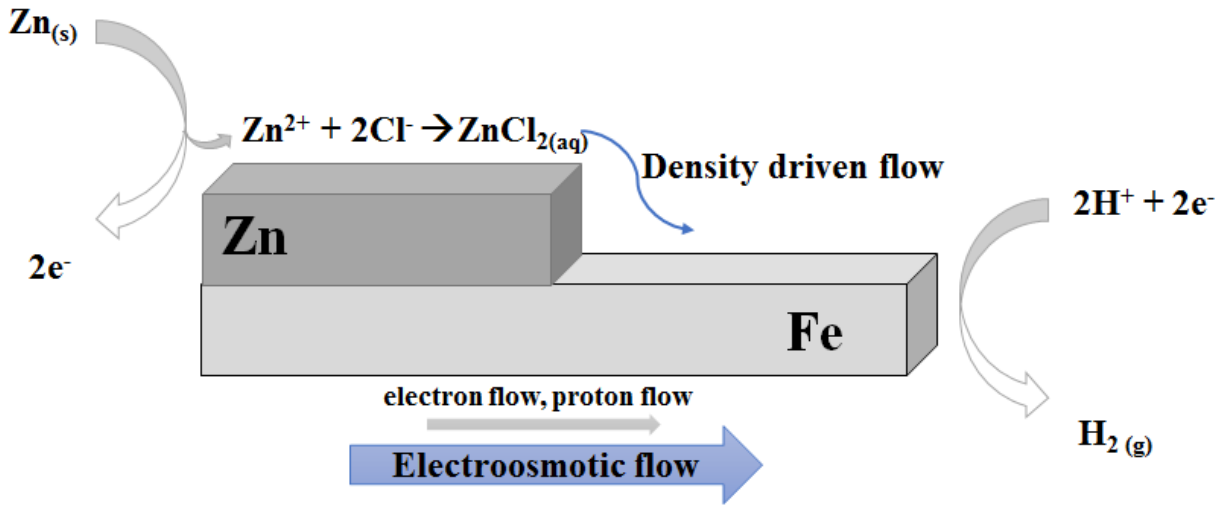


**Figure 5-6.** Zn-Fe micropump mechanism in HCl, showing both electroosmotic flow as a result of electron and proton migration from zinc to iron as well as a density-driven flow as a result of the formation of zinc chloride.

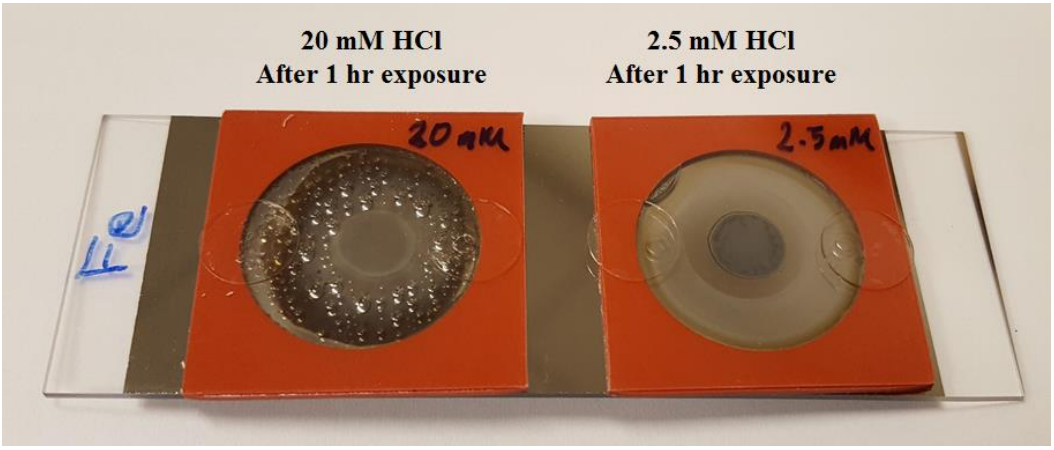


**Figure 5-7.** Bubble formation on iron in Zn-Fe micropumps after an hour exposure to high concentration of acid. In lower concentrations after prolonged exposure, an exclusion area surround the reacted zinc is observed but no macroscale bubbles is detectable by eye.

## 5.5 Fluid flows characterization and mechanism in complex media

### 5.5.1 Motivation

While Zn-Fe micropumps have been shown to operate fantastically in acidic media, it was examined in other types of media due to the highly reactive nature of zinc and the special dual-mechanism involved in the initiation and continuation of fluid and particle motion. To this end, Zn-Fe micropumps were tested in high-electrolyte media to see the effects of high concentration of ions on pumping speeds.

### 5.5.2 pH Neutral electrolyte – Sodium chloride solution

Zn-Fe micropumps were exposed to 10 mM solution of aqueous sodium chloride solution and was shown to produce fluid flows similar to that present in dilute acidic media. Figure 5-8 shows the speed profile of tracer particles in 10 mM NaCl when exposed to Zn-Fe micropumps.

Similarly to low acid concentrations reported in Figure 5-5, speeds start off low and increases to a possible terminal velocity of about 6 μm/s. The lower overall speed is likely due to the decreased reactivity of zinc to the solution, as zinc does not directly react to the salt but to the oxygen content present in the solution. The pump has been tested up to 3M NaCl conditions and fluid flows were observed. Speeds were not measure, however, due to the high ionic conditions causing the tracer particles to aggregate and make consistent tracking difficult.

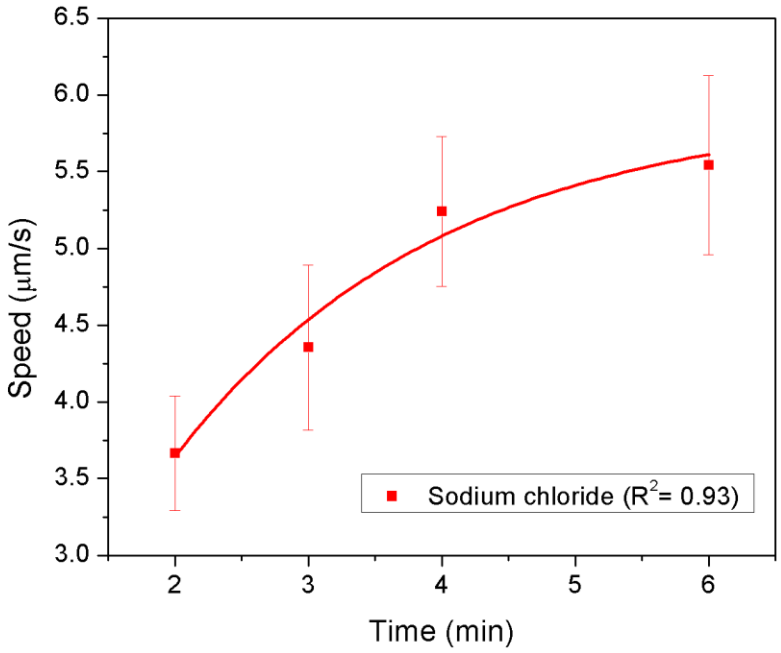


**Figure 5-8.** Fluid pumping speeds of Zn-Fe micropump when exposed to 10 mM NaCl. Curve fitted with exponential growth algorithm in OriginPro8, exhibiting excellent correlation.

The redox reactions that occur in this system is actually due to the corrosion of zinc, followed by iron in the electrolyte solution. In the salt electrolyte solution, the following half reactions take place:

$$M_{(s)} \rightarrow M^{2+} + 2e^- \quad \text{, where M = Zn, Fe} \qquad (2)$$

$$O_{2\,(g)} + 2\,H_2O + 4e^- \rightarrow 4OH^- \qquad (3)$$

$$M^{2+} + 4\,OH^- \rightarrow [M(OH)_4]^{2-}{}_{(aq)} \qquad (4)$$

In this mechanism, electroosmotic flows is impeded due to the presence of ions in the solution, so the dominating flow observed is density-driven. The specie involved in the density

flows is likely to be zinc oxide. Evidence of this is in the inverted micropump trials, where the tracer particles also have an inverted flow in comparison to upright pump systems. The most interesting phenomena observed in this pump system is that after zinc is complete consumed, iron also has traces of being consumed, albeit at lower rates. This however, does not provide fluid flows as there is no asymmetry present in the system after zinc is fully consumed.

### 5.5.3 Acidic buffered solution – Sodium citrate buffer solution

To examine the effect of ions on the micropump in an acidic media, a sodium citrate buffer solution (pH 5) was used. Figure 5-9 shows the speed profile of Zn-Fe micropumps when exposed to 10 mM sodium citrate buffer. It is very comparable to the speed profile of pure HCl micropumps. The profile also shows that it reaches the same 10 μm/s terminal velocity, but at a much faster rate in comparison to 5 mM HCl solution. This may be due to the buffering in the solution, which has an effect on the electric double layer and species diffusion. Mechanistically speaking, it likely follows the mechanism illustrated in Figure 5-6, but the species involved in creating the density-flows is zinc citrate instead of zinc chloride, as both are highly soluble species. The lower initial velocity of the acid buffered pump likely due to the system being buffered.

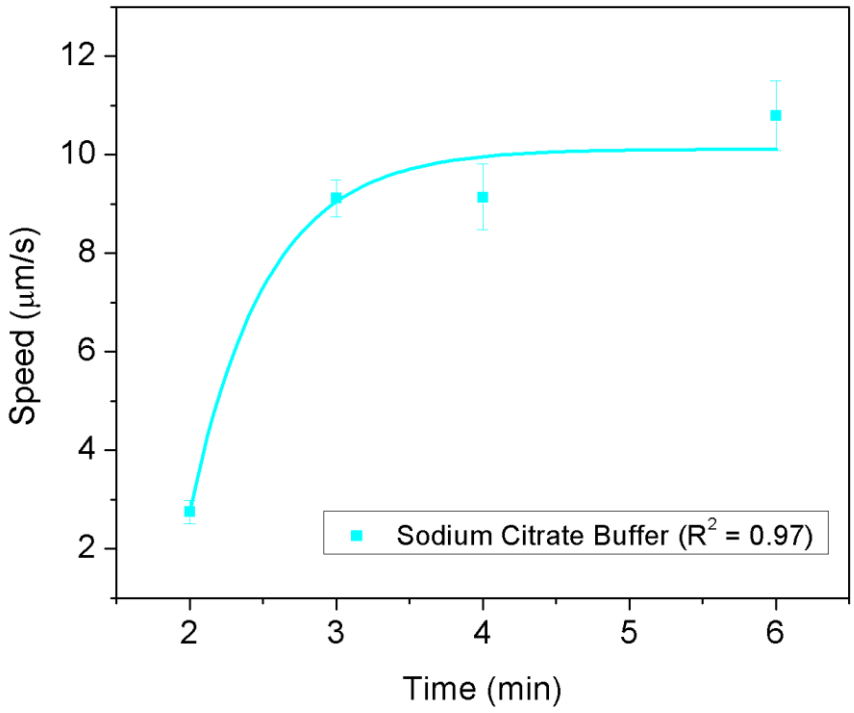


**Figure 5-9.** Pumping speed profile of Zn-Fe micropump when exposed to 10 mM Sodium citrate buffer (pH 5) solution. The data fit extremely well to an exponential growth algorithm in OriginPro8.

### 5.5.4 Basic buffered solution – Tris-HCl buffer solution

In an effort to better understand the effects of reagents on Zn-Fe micropumps, a basic Tris-HCl buffer (pH 9) solution was used to see whether the pump can operate in basic conditions. Figure 5-10 shows the speed profile of micropump speeds in Tris-HC buffer. The particles exhibit the same outwards pumping but speeds decrease drastically over time. Initial speeds when observed at 2 minutes after addition shows high speeds near the terminal velocity exhibited by the other systems. The speeds over time, however, exhibit a different profile. The speed profile of Tris-HCl solution exhibits an exponential decay with respect to time. This may be a result of the

buffer solution losing its ability to maintain HCl in the system as the ionic concentration used in the experiment was extremely low (10 mM). With less acid, reactivity of the zinc decreases, leading to slower pumping speeds over time.

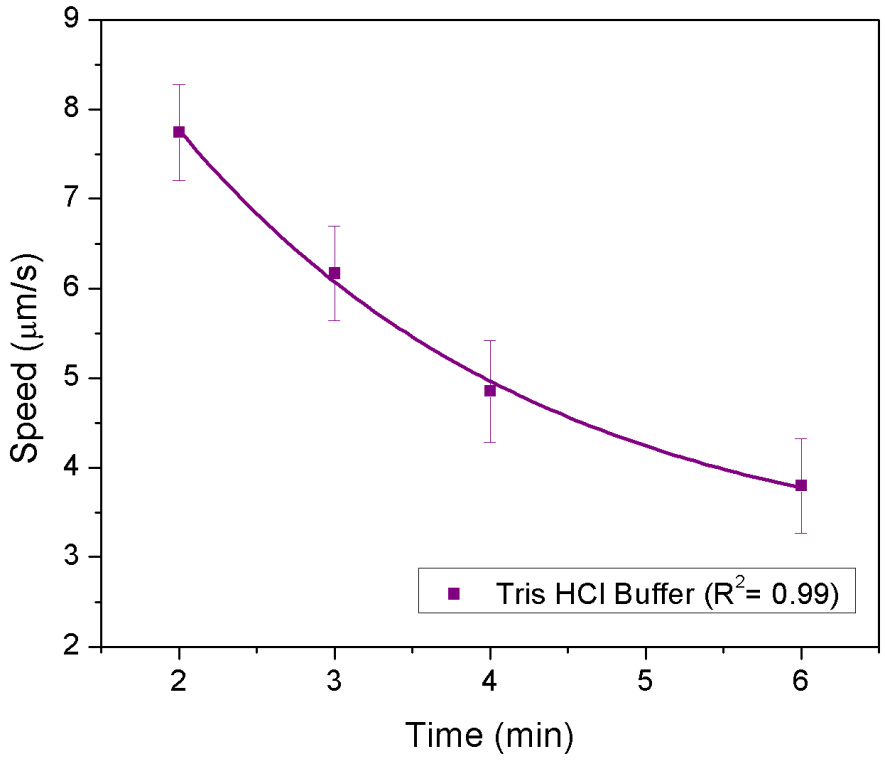


**Figure 5-10.** Pumping speed profile of Zn-Fe micropump when exposed to 10 mM Tris-HCl buffer (pH 9) solution. The data shows a different profile in comparison to acidic and neutral electrolyte species, and fit with high confidence to an exponential decay algorithm in OriginPro8.

### 5.6 Generalized reaction scheme

From the fluid flow characterization in HCl, NaCl, acidic and basic buffered solutions, it would seem that the presence of a depolarizing species (such as acid or oxygen) will lead to a reaction with zinc and trigger fluid flow. Using this, a generalized reaction scheme of the bipolar redox reaction can be made (Figure 5-11).

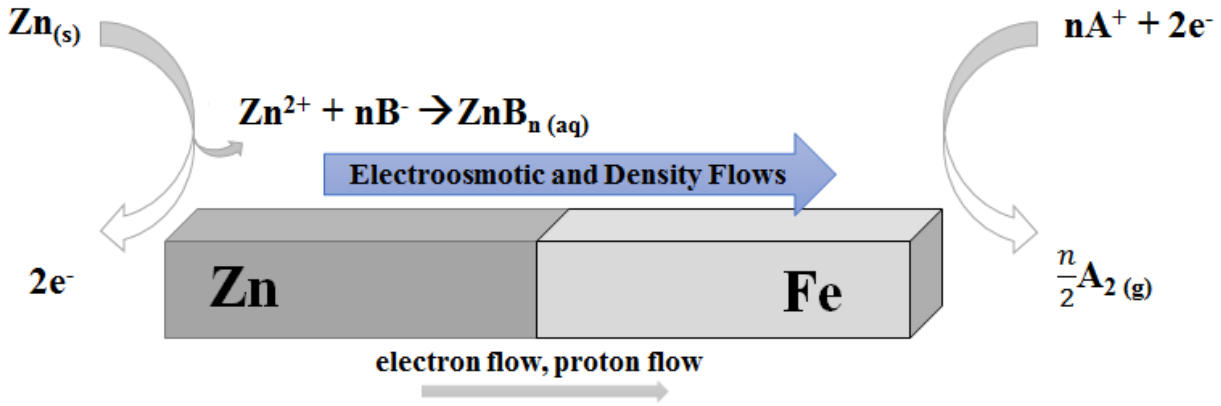


$$Zn_{(s)} + nAB \rightarrow \frac{n}{2}A_2 + ZnB_n$$

AB = depolarizer (*e.g.* protons, oxygen)

**Figure 5-11.** Generalized reaction scheme for Zn-Fe micropumps when exposed to a depolarizer/electroactive substance.

## 5.7 Conclusion

By exploiting biodegradable materials that are electroactive, biobatteries have been fabricated to power implant devices. A new application for such materials is for active colloidal transport through adaptations into a micropump system. Bimetallic zinc-iron is one such example. When exposed to electroactive species such as salt or acid, a bipolar redox reaction occurs that generates electroosmotic and density flows along the pump surface. Depending on the solubility of the depolarizing species, the density flows can be modulated. In addition, because of the dual-mode of fluid transport, the system works extremely well in high electrolyte conditions. The pump was shown to be operational in high ionic conditions as well as in acid and base buffered solutions. Zn-Fe micropump is an extremely versatile system in its range of chemical fuels and high fluid flow speeds that are comparable to other reported systems.[22-24]

While there are side reactions that can occur (*e.g.* direct formation of hydrogen from zinc) instead of a bipolar redox reaction, this is not problematic as long as we remain in low concentrations ranges. Also, as the products of the reaction aid in fluid pumping, products formed from side reactions do not decrease fuel efficiency. Zn-Fe micropumps are so reactive that even low concentrations of fuel can produce speeds of tens of microns. This work provides a new generalized system that allows for the utilization of a wide range of chemical fuel to trigger fluid motion. Due to the biocompatibility of the metals involved in the fabrication and the relatively low cytotoxity of zinc-containing side products, the Zn-Fe system can have future applications for *in vivo* stimuli-responsive devices.

## 5.8 References


1. Voldman, J.; Gray, M. L.; Schmidt, M. A. Microfabrication in biology and medicine. Annu. Rev. Biomed. Eng. 1999, 1, 401-425.
2. Eggers, M.; Ehrlich, D. A review of microfabricated devices for gene-based diagnostics. Hematol. Pathol. 1995, 9, 1-15.
3. Receveur, R. A. M.; Lindemans, F. W.; de Fooij, N. F. Microsystem technologies for implantable applications. J. Micromech. Microeng. 2007, 17, R50.
4. Lautenschläger, F.; Piel, M. Microfabricated devices for cell biology: all for one and one for all. Curr. Opin. Cell Biol. 2013, 25, 116-124.
5. Hang, D. J. T.; Hu, R.; Song, P.; Roy, I.; Yong, K-T. Approaches and challenges of engineering implantable microelectromechanical systems (MEMS) drug delivery systems for in vitro and *in vivo* applictions. *Micromachines* **2012**, *3*, 615-631.
6. Amar, A. B.; Kouki, A. B.; Cao, H. Power Approaches for Implantable Medical Devices. *Sensors* **2015**, *15*, 28889-28914.
7. Fonseca, C. P.; Neves, S. Electrochemical properties of a biodegradable polymer electrolyte applied to a rechargeable lithium battery. J. Power Sources 2006, 1, 712-716.
8. Nathan, M. Microbattery technologies for miniaturized implantable medical devices. Curr. Pharm. Biotech. 2010, 11, 404-410.
9. Yin, L.; Huang, X.; Xu, H.; Zhang, Y.; Lam, J.; Cheng, J.; Rogers, J. A. Materials, designs, and operational characteristics for fully biodegradable primary batteries. Adv. Mater. 2014, 26, 3879-3884.
10. Hwang, S-W.; Tao, H.; Kim, D-H.; Cheng, H.; Song, J-K.; Rill, E.; Brenckle, M. A.; Panilaitis, B.; Won, S. M.; Kim, Y-S.; Song, Y. M.; Yu, K. J.; Ameen, A.; Li, R.; Su, Y.; Yang, M.; Kaplan, D. L.; Zakin, M. R.; Slepian, M. J.; Huang, Y.; Omenetto, F. G.; Rogers, J. A. A physically transient form of silicon electronics. Science 2012, 337, 1640-1644.
11. Paxton, W. F.; Sundararajan, S.; Mallouk, T. E.; Sen, A. Chemical locomotion. *Angew. Chem. Int. Ed.* **2006**, *45*, 5420–29.
12. Hess, H.; Vogel, V. Molecular shuttles based on motor proteins: active transport in synthetic environments. *Rev. Mol. Biotechnol.* **2001**, *82*, 67–85.
13. Dey, K. K.; Wong, F.; Altemose, A.; Sen, A. Catalytic motors – quo vadimus? *Curr. Opin. Coll. Interface Sci.* **2016**, *21*, 4-13.
14. Yadav, V.; Duan, W.; Butler, P. J.; Sen, A. Anatomy of Nanoscale Propulsion. *Annu. Rev. Biophys.*, **2015**, *44* , 77,
15. Sánchez, S.; Soler, L.; Katuri, J. Chemically powered micro- and nanomtors. *Angew. Chem. Int. Ed.* **2014**, *54*, 1414-1444.
16. Ebbens, S. J. Active colloids: Progress and challenges towards realizing autonomous applications. *Curr. Opin. Colloid Interf. Sci.* **2016**, *21*¸14-23.
17. Duan, W.; Wang, W.; Das, S.; Yadav, V.; Mallouk, T. E.; Sen, A. Synthetic nano- and micromachines in analytical chemistry: sensing, migration, capture, delivery, and separation. *Annu. Rev. Anal. Chem.* **2016**, *8*, 311-333
18. Gao, W.; Wang, J. Synthetic micro/nanomotors in drug delivery. *Nanoscale* **2014**, *6*, 10486-10494.
19. Adelmohsen, L. K. E. A.; Peng, F.; Tu, Y,; Wilson, D. A. J. Mater. Chem. B. 2014, 2, 2395-2408.

20. Paxton, W. F.; Baker, P. T.; Kline, T. R.; Wang, Y.; Mallouk, T. E.; Sen, A. Catalytically Induced Electrokinetics for Motors and Micropumps. *J. Am. Chem. Soc.* **2006**, *128*, 14881-8.
21. Moran, J. L.; Posner, J. D. Electrokinetic locomotion due to reaction-induced charge auto-electrophoresis. *J. Fluid Mech.* **2011**, *680*, 31-66.
22. Yariv, E. Electrokinetic self-propulsion by inhomogeneous surface kinetics. *Proc. R. Soc. A* **2010**, *467*, 1645-1664.
23. Liu, R.; Sen, A. Autonomous Nanomotor Based on Copper–Platinum Segmented Nanobattery. *J. Am. Chem. Soc.*, **2011**, *133*, 20064-20067.\
24. Wang, W.; Chiang, T.; Velegol, D.; Mallouk, T.E. Understanding the Efficiency of Autonomous Nano- and Microscale Motors. *J. Am. Chem. Soc.*, **2013**, *135*, 10557-10565.

## Concluding Remarks

While research on autonomous motors and pumps have been focused on developing new systems, it is just as important to try to increase efficiency of existing systems in an effort to better understand and design nano- and micromachines. Optimization of fuels and geometries, for example, will significantly impact motor speed, fluid drag, and the efficiency of the motors. As of yet, few studies have been conducted with respect to this. The work discussed in Chapter 2 and 3 explored fuel optimization and light-enhancement effects on motor efficiency, which provides a fundamental study on how silver-based systems react in micromolar concentrations of iodine.

Another major aspect of research into active colloids is the materials the system is composed of. There is a wealth of information that can be gleaned from exploring alternative materials from the extensive literature already present in every field imaginable. By incorporating new materials or multiple components into a system, we can more easily tailor its behavior and exert finer control. There are emerging studies that have already begun to present multicomponent motors, dual modes of control, amongst others. The work discussed in Chapter 4 and 5 took materials from therapeutics (biocompatible polymer) and battery technology (biodegradable batteries) and applied it to produce a micropump system that is capable of responding to stimuli and trigger fluid flows. These studies can provide a template on how similar materials can be converted into autonomous motor and pump systems.

The field of nano- and micromachines is ever changing. In order for developed autonomous systems to find real-world applications, the environment and the task it performs must be taken into account. Therefore, the work discussed in this dissertation utilizes multi-faceted points of

control to allow for tailoring of these systems to more specific applications and to take us one step closer in making today's dreams into tomorrow's science facts.

## Appendix: Nanomotor Efficiency Calculations

### *Efficiency Calculation for Ag-Pt/$I_2$ System*

Ag-to-AgI Conversion reaction:

$I_2 + e^- \rightarrow 2I^-$ $\quad E^0 = 0.535\ V$

$Ag + I^- \rightarrow AgI + e^-$ $\quad E^0 = 0.152\ V$

$E^0_{cell} = 0.687\ V$

$E_{cell\ (measured)} = 0.66V$

$$\eta_{ambient} = \frac{P_{mech}}{P_{chem}} = 1.34 \times 10^{-5}$$

*Mechanical Power Output ($P_{mech}$):*

$$P_{mech} = F_{drag} v = f v^2$$

$$f = \frac{2\pi\mu L}{ln\left(\frac{2L}{R}\right) - 0.72}$$ where $\mu$ is the dynamic viscosity of water ($1 \times 10^{-3}$ Ns/m), $L$ is the length of cylinder ($3 \times 10^{-6}$ m), and $R$ is the radius of cylinder ($150 \times 10^{-9}$ m)

$$f = \frac{2\pi(1 \times 10^{-3}\ Ns/m^2)(3 \times 10^{-6}\ m)}{ln\left(\frac{2 \times 3 \times 10^{-6}\ m}{150 \times 10^{-9}\ m}\right) - 0.72} = 8.28 \times 10^{-9}\ Ns/m$$

Speed of motor in ambient lighting situation:

$$v^2{}_{ambient} = (20 \times 10^{-6}\ m/s)^2 = 4 \times 10^{-10}\ (m/s)^2$$

*Chemical Power Input ($P_{chem}$):*

$P_{chem} = n_{I_2}\Delta G$

$n_{I_2} = \dfrac{n_{fuel}}{m_{rods} \times t_{rxn}}$

where $n_{I_2}$ is the rate of fuel consumption (mol/s for each nanorod, ΔG is the Gibbs free energy for halide conversion per mol of $I_2$, $m_{rods}$ is the number of rods in system (calculated below) and $t_{rxn}$ is the reaction time (assuming instantaneous reaction, $t_{rxn}$ = 1 second)

$n_{fuel} = 1.13 \times 10^{-9}\ mol\ I_2$

$m_{rods} = \dfrac{10^9\ rods}{cm^2} \times 0.3167\ cm^2 \times \dfrac{1}{4}\ dilution\ factor$

$= 7.9 \times 10^7 \dfrac{rods}{sample\ vol\ 1\ mL} \times 10^{-3}\ mL\ sample\ size = 7.9 \times 10^5\ rods$

$\Delta G = -nFE^0_{cell}$

$\Delta G = -(2\ mol\ e^-)\left(94687 \dfrac{C}{mol} e^-\right)(0.687\ V) = 1.325x\ 10^5\ J = 1.325 \times 10^2\ kJ/mol\ I_2$

$P_{chem} = n_{I_2}\Delta G = 2.85 \times 10^{-17} \dfrac{mol}{s} \times 1.325x\ 10^2\ kJ/mol = 3.784\ x\ 10^{-15} \dfrac{kJ}{s}$

# VITA

## Flory K. Wong

Flory Wong is a native New Yorker and graduated magna cum laude from CUNY Macaulay Honors College with a B.S. in Chemistry. With a growing interest in nanomaterials she fostered with Professor Valeria Balogh-Nair on synthetic hybrid organic/inorganic quantum dots, she applied and was accepted into the Ph.D. program at Pennsylvania State University. In 2011, she began working under the tutelage of Professor Ayusman Sen on developing novel catalytic nanomotor and pump systems. Since then, she has developed and fully characterized many novel nanomotor and pump systems that does not rely on traditional peroxide fuels. In her free time, she likes to peruse science fiction novels and relieves her stress in a good video game or by tinkering with computer systems.